Experimental Investigations on Transverse Dispersive Mixing in Heterogeneous Porous Media

Von der Fakultät Bau- und Umweltingenieurwissenschaften der Universität Stuttgart
zur Erlangung der Würde eines Doktors der
Ingenieurwissenschaften (Dr.-Ing.) genehmigte Abhandlung

Vorgelegt von

Md. Arifur Rahman

aus Bangladesh

Hauptberichter:	Prof. Dr.-Ing. Rainer Helmig
Mitberichtern:	Prof. Dr. rer. nat. Peter Grathwohl
	PD Dr.-Ing. Olaf A. Cirpka
Tag der mündlichen Prüfung:	20. Dezember 2004

Institut für Wasserbau der Universität Stuttgart

2005

D93 Experimental Investigations on Transverse Dispersive Mixing in Heterogeneous Porous Media

Rahman, Md. Arifur:

Experimental Investigations on Transverse Dispersive Mixing in Heterogeneous Porous Media/von Md. Arifur Rahman. Institut für Wasserbau, Universität Stuttgart. – Stuttgart: Inst. für Wasserbau der Univ., 2005

(Mitteilungen / Institut für Wasserbau, Universität Stuttgart; H. 140)
Zugl.: Stuttgart, Univ., Diss., 2005
ISBN: 9-933761-43-3
NE: Institut für Wasserbau <Stuttgart>: Mitteilungen

Herausgegeben 2005 von Eigenverlag des Instituts für Wasserbau
Druck: Sprint-Druck GmbH, Stuttgart

Dedicated to my parents

Acknowledgement

This doctoral thesis is the outcome of my last three and half years research working as research assistant at the Institut für Wasserbau in the Universität Stuttgart. In this period, I worked in the project “Scaling Effects of in-situ Mixing in Heterogeneous Aquifers” (Skaleneffekte bei der in-situ-Durchmischung gelöster Stoffe in heterogenen Grundwasserleitern) funded by the Deutsche Forschungsgemeinschaft (DFG). Hence, Deutsche Forschungsgemeinschaft (DFG), which funded this research within the Emmy Noether program under the grants Ci 26/3-2 to Ci 26/3-4, is gratefully acknowledged.

I am extremely indebted to PD Dr.-Ing. Olaf A. Cirpka for giving me an opportunity to work in his research group and for his excellent supervision and inspiration throughout the thesis work. From his instruction, I learn the arts and skills of a researcher and more importantly the way of thought.

My special thanks go to Prof. Dr. Peter Grathwohl and Prof. Rainer Helmig, to be my co-supervisor and to support me with their meaningful discussions, invaluable advices and rich ideas.

For the technical support in various respects, special thanks deserve the persons from different laboratories. Without their support it would be impossible for me to complete this experimental research. In particular, I appreciate the indisputable support that I received from the mechanical workshop team led by Jürgen Laich and Henning Eickhoff. I also thank Oliver Trötschler, Thomas Haslwimmer, Johannes Schnieders and Tanja Fimpel for their immense help and support whenever it was needed. I also appreciate the support I received from the electrical lab personnel -Wolfgang Rempp, Steffen Hägele, and Gerhard Schmid.

I am thankful to my working group member Wolfgang Novak for translating my summary to German language and to my other working group members, Surabhin Jose, Waltraud Kull and Ju Qingsong for their fundamental critique, which helped me to improve my research. I also thank Arshad Hossain, Khawar Zaman, Sachin Patil, Kamal Hossain, and Jahir Mollah, all my student assistants, for providing me a very reliable assistance to the laboratory work.

I extend my thanks to my friend Muhit Razzaque in appreciation of his helping hand, provided, without ambiguity, at the hours of necessity.

Finally, I would like to express my heartfelt gratitude to my parents, and brother and sisters, for their endless encouragement and well wishes.

Table of Content

List of Figures

List of Tables

Symbols and Abbreviations

Abbreviations:

BTC	Break through curve
PVC	Polyvinylchloride
REV	Representative elementary volume

Dimensions

L	Length
M	Mass
T	Time
h	Effective Injection width/ height of the plume

Variable	Physical Meaning	Dimension
α_{ij}	Local dispersivity	[L]
α^*_{ij}	Macrodispersivity	[L]
α_a	Apparent dispersivity	[L]
α_L	Longitudinal transverse dispersivity	[L]
α_T	Transverse dispersivity	[L]
α_t^a	Apparent transverse dispersivity	[L]
λ	Correlation length of the aquifer heterogeneities	[L]
μ_o	Zeroth spatial moment	[L]
μ_i	First spatial moment	[L²]
μ_{ij}	Second non-central spatial moment	[L³]
μ_{ij}^c	Second central spatial moment	[L³]
ϕ	Total head-loss	[L]
τ_d	Characteristic dispersive time	[T]
τ_{DT}	Dispersion time scale	[T]
A	Cross-sectional area	$[L^2]$
c	Solute concentration	$[M/L^3]$
$\bar{c}$	Average concentration of solute	$[M/L^3]$
c_o	Inflow solute concentration	$[M/L^3]$
D	Hydrodynamic dispersion tensor	$[L^2/T]$

D_{mech}	Mechanical dispersion tensor	[L²/T]
D^*	Macrodispersion coefficient	[L^2/T]
D_a	Apparent dispersion coefficient	[L^2/T]
D^{ens}	Ensemble dispersion coefficient	[L^2/T]
D_a	Apparent dispersion coefficient	[L²/T]
D_e^*	Effective diffusion coefficient	[L^2/T]
D^e	Effective dispersion coefficient	[L^2/T]
D_x	Longitudinal dispersion coefficient	[L^2/T]
D_y	Lateral transverse dispersion coefficient	[L^2/T]
D_z	Vertical longitudinal dispersion coefficient	[L^2/T]
D_t^a	Apperent transverse dispersion coefficient	[L^2/T]
f^*	Dispersive flux	[M/LT^2]
K	Hydraulic conductivity	[L/T]
l	Correlation length	[L]
$\langle m_{2c} \rangle$	Cross-sectional average of second central temporal moment	[T^3]
θ_e	Effective porosity	[-]
P_e	Peclet number	[-]
q	Darcy flux or specific discharge	[L/T]
Q_{tot}	Total discharge	[L^3/T]
s	Volumetric source/sink	[L^3]
S_0	Specific storage coefficient	[-]
t	Time	[T]
V^*	Macroscopic velocity	[L/T]
ω_{mac}	Macroscopic rotational seepage velocity	[1/T]
D_{mac}^{φ}	Macroscopic rotational dispersion coefficient	[1/T]
v	Seepage velocity	[L/T]
$\bar{v}$	Mean seepage velocity	[L/T]
v_a	Apparent seepage velocity	[L/T]
X_{alk}	Mixing ratio	[-]

Abstract

Transverse mixing is identified to be a controlling factor in natural attenuation of extended biodegradable plumes originating from continuously emitting sources. While the heterogeneity of natural formations determines the spreading of solutes in groundwater, mixing between organic contaminants and oxidants of ambient groundwater flow controls the degradation of large plumes.

This thesis offers a promising approach to the characterization and quantification of transverse dispersion coefficient in heterogeneous porous media. The aim of the study is to deepen the understanding of transverse dispersion and mixing in natural heterogeneous porous media. Particularly, I develop an experimental method for the determination of transverse dispersion coefficients and apply it to verify whether there is any enhancement of transverse mixing in natural heterogeneous porous media. To this end, I conduct conservative and reactive tracer tests in a one-dimensional as well as quasi two-dimensional laboratory and technical scale sandboxes. The heterogeneous filling mimics natural sediments including a distribution of different hydro-facies and micro-structures within the sand lenses.

Heterogeneity causes plume meandering, leading to distorted concentration profiles. Without the knowledge about the velocity distribution, it is not possible to determine meaningful vertical dispersion coefficients from the conservative concentration profiles. The estimated vertical transverse dispersion coefficients are fairly small, as expected from the time-dependent effective dispersion coefficient, which is relevant to describe mixing. The values are less than an order of magnitude larger than the effective molecular diffusion coefficient. For typical groundwater flow velocities, therefore, the velocity-independent contribution to transverse dispersion cannot be ignored. No significant increase in the transverse dispersion coefficient with increasing travel distance indicates that the heterogeneity has hardly any impact on vertical transverse mixing. In general, linear stochastic theory, predicting only a small increase in transverse vertical macrodispersion coefficients in the large-time limits, are in very good agreement with the findings.

Zusammenfassung

In den letzten Jahren haben Untersuchungen ergeben, dass die Ausnutzung des natürlichen Rückhaltevermögens eine günstige Alternative gegenüber aktiven Sanierungsmaßnahmen für Altlasten darstellt, vor allem auf Grund der hohen Kosten und technischer Schwierigkeiten aktiver Maßnahmen. Der natürliche mikrobielle Abbau von Schadstoffen setzt die Durchmischung von Schadstoffen aus kontinuierlichen Quellen mit Reaktanten aus dem umgebenden Grundwasser voraus. Vor allem Oxidationsmittel wie Sauerstoff oder Nitrat werden im Bereich des Schadensherdes der Abstromfahne schnell aufgezehrt und müssen aus dem umgebenden Grundwasser durch transversalen Austausch nachgeliefert werden. Daher hängen Abbauraten in Schadstofffahnen empfindlich von transversalen Durchmischungsvorgängen am Rande der Abstromfahne ab.

Diese Dissertation bietet einen vielversprechenden Ansatz zur Charakterisierung und Quantifizierung der transversalen Dispersion in heterogenen porösen Medien. Ziel dieser Studie war es, das Verständnis der transversalen Dispersion und Durchmischung in natürlichen heterogenen porösen Medien zu vertiefen. Insbesondere verifiziere ich experimentell, ob die Heterogenität natürlicher poröser Medien transversale Durchmischungsvorgänge begünstigt.

Hierzu führte ich Experimente in drei unterschiedlichen Größenmaßstäben durch. Zuerst führte ich Experimente in einer spiralförmigen Säule durch, um Methoden zur Bestimmung der transversalen Dispersivität auf der Porenskala zu entwickeln. Zweitens habe ich auf der für Laborversuche üblichen Skala einen quasi-zweidimensionalen künstlichen Grundwasserleiter entworfen. Dieser bestand aus unterschiedlichen Gemischen von Quarzsand verschiedener Körnung, sodass einerseits homogene und andererseits kleinskalig heterogene poröse Medien vorlagen. In diesem Versuchsaufbau führte ich konservative und reaktive Tracerversuche durch, um Methoden zur Bestimmung der transversalen Dispersion zu entwickeln und um darüber hinaus den Einfluss kleinräumiger Strukturen in porösen Medien zu bewerten. Drittens entwarf ich in einer Rinne auf technischer Skala einen quasi-zweidimensionalen künstlichen Grundwasserleiter. Diese Rinne habe ich solchermaßen mit unterschiedlichen Typen von Quarzsand befüllt, dass sowohl großräumige als auch kleinräumige Sedimentstrukturen entstanden, welche natürlichen Sedimentstrukturen nachempfunden waren. In dieser Rinne habe ich sowohl konservative als auch reaktive Tracerversuche durchgeführt, um die vertikale transversale Durchmischung in heterogenen porösen Medien zu quantifizieren.

Kapitel 4 beschreibt meine experimentelle Vergehensweise für die erste Reihe von Experimenten zur Bestimmung der transversalen Dispersivität auf der Porenskala. Ich wandte

den theoretischen und numerischen Ansatz beruhend auf die Taylor-Aris Dispersion von *Cirpka und Kitanidis* [2001] anhand einer speziell entwickelten spiralförmigen Bodensäule an. Eine spiralförmige Säule habe ich deshalb verwendet, weil sie eine gescherte Strömung, so wie sie für Taylor-Aris-Dispersion notwendig ist, in porösen Medien erzwingt. In dieser experimentellen Vorgehensweise messe ich die Spreitung der Durchbruchskurve, welche umgekehrt proportional zum lokalen transversalen Dispersionskoeffizienten ist. Der Vorteil hierbei ist, dass Parameter für die transversale Dispersion im allgemeinen sehr kleine Werte haben und daher experimentell auf andere Art und Weise kaum zu bestimmen sind. In dieser Apparatur führte ich fünf Tracerversuche bei unterschiedlichem Durchfluss zwischen 1.5×10^{-7} m³/s und 5.55×10^{-9} m³/s durch. Der theoretische Ansatz, basierend auf einer analytischen Lösung für Taylor-Aris-Dispersion zu späten Zeitpunkten, ergab für die lokale transversale Dispersivität einen Wert von 7.27×10^{-4} m. Der numerische Ansatz, basierend auf der Modellierung zeitlicher Momente, ergab 6.57×10^{-4} m. Beide Werte sind relativ hoch für transversale Dispersivitäten.

Ein möglicher Grund für die hohen errechneten Werte liegt darin, dass der theoretische und der numerische Ansatz nach *Cirpka und Kitanidis* [2001] die Steigung der Spiralgänge und damit verbundene sekundäre Strömungsvorgänge vernachlässigt. *Benekos* [2004] entwickelte ein Programm zur numerischen Simulation der vollständigen Strömungsvorgänge und des Stofftransportes in spiralförmigen Säulen zur Bestimmung der transversalen Dispersivität. Er zeigte, dass eine Vernachlässigung der sekundären Strömungsvorgänge zu einer signifikanten Fehleinschätzung der transversalen Dispersivität führen kann. Ein direkter Vergleich der Ergebnisse mit dem durch geführte Untersuchungen zeigte kleinere Werte für die transversale Dispersivität, wenn die sekundäre Strömung berücksichtigt wird. Die Unterschiede sind jedoch unter den hier vorliegenden Strömungsverhältnissen und der Geometrie der hier verwendeten Säule nicht überwältigend groß.

In Kapitel 5 befasse ich mich mit den konservativen und reaktiven Tracerexperimenten in homogenen porösen Medien auf der Laborskala. Zunächst entwickelte ich ein digitales bildgebendes Verfahren mit Farbtracern, um die transversale Durchmischung zu visualisieren und um den transversalen Dispersionskoeffizienten in porösen Medien zu bestimmen. Ich injizierte den Farbstoff in den Versuchsaufbau und hielt die sichtbare Verteilung des Farbstoffes fotographisch durch mehrere Glasfenster im Versuchsaufbau fest. Dazu verwendete ich eine Digitalkamera vom Typ Casio QV-5700. Diese war, um einheitliche und reproduzierbare Verhältnisse zu schaffen, auf stählernen, im Boden verankerten Ständern im Abstand von

jeweils 1.6m von den Fenstern befestigt. Für konstante Lichtverhältnisse habe ich eine künstliche Lichtquelle bei Nacht verwendet. Um aus den digitalen Bildern die Werte der Konzentration des Farbstoffes abzuleiten, habe ich die Digitaldaten kalibriert. Die Kalibration beruht auf einer nicht linearen Interpolation zwischen zwei Referenzbildern bei völliger Abwesenheit des Farbstoffes und bei maximaler Konzentration.

Ich führte ein Experiment mit konservativen Farbtracern durch, in dem ich den Farbtracer an der linken Seite auf halber Höhe über eine Breite von 7.5 cm in den Versuchsaufbau injizierte. Die hydraulischen Randbedingungen erzwangen eine Strömung von links nach rechts. Mit Hilfe meines bildgebenden Verfahrens wertete ich die Konzentrationsverteilung im stationären Zustand aus. Durch Anpassung analytischer Lösungen an transversale Querschnitte der Konzentrationsverteilung erhielt ich Werte für die transversale Dispersivität von circa 2.40×10^{-4} m.

In reaktiven Tracerversuchen injizierte ich eine alkalische Lösung auf halber Höhe und verwendete eine saure Lösung als umgebendes Wasser. Die sich ergebende Säure-Base-Reaktion hängt ausschließlich von der transversalen Durchmischung ab. Mit Hilfe von pH-Indikatoren konnte ich den Rand der Abstromfahne alkalischen Wassers sichtbar machen. Zur Auswertung verwendete ich eine analytische Lösung für den Abstand bestimmter Verdünnungsstufen innerhalb der Abströmfahne von der Injektionsstelle. Die sich daraus ergebenden Werte für den transversalen Dispersionskoeffizienten schwankten zwischen 4.90×10^{-9} m²/s und 5.90×10^{-9} m²/s. Bei Vernachlässigung molekularer Diffusion entspricht dies unter den gegebenen hydraulischen Verhältnissen einer transversalen Dispersivität von circa 2.5×10^{-4} m und steht in guter Übereinstimmung mit den Ergebnissen der konservativen Tracerversuche.

Ich konnte zeigen, dass dies eine einfache und zuverlässige Methode zur Untersuchung dispersiver Durchmischung in porösen Medien ist. Die Ausrüstung ist beträchtlich günstiger als bei anderen nichtinvasiven bildgebenden Verfahren, wie zum Beispiel bei NMRI (Nuclear Magnetic Resonance Imaging) oder PVI (Photoluminescent Volumetric Imaging). Um mit meiner Methode präzise Ergebnisse zu erzielen, sollte durch die Verwendung stabiler Stative möglichst pixelgenaue Übereinstimmung der Bildausschnitte zwischen den Bildern während des Experimentes und den Bildern zur Kalibrierung erreicht werden.

Kapitel 6 befasst sich mit dem Einfluss von kleinräumigen Strukturen auf die transversale Dispersion in natürlichen porösen Medien. Den in Kapitel 5 verwendete Versuchsaufbau habe ich insgesamt zweimal mit unterschiedlichen Sandgemischen solchermaßen befüllt, dass kleinräumige Heterogenitäten im Bereich von wenigen Zentimetern entstanden. Für je-

den Sandtyp führte ich zwei Reihen von reaktiven Tracerexperimenten durch und schätzte die transversalen Dispersionskoeffizienten aus der Länge und Breite der Abstromfahnen ab. Abbildungen 1 und 2 zeigen zwei fahnen alkalischen Wassers, die sich bei kleinräumig heterogenen Sandbefüllungen ergeben. Die hier ermittelten transversalen Dispersionskoeffizienten liegen im Bereich von $4.6x10^{-9}$ m²/s bis $8.9x10^{-9}$ m²/s. Dies ist in der Größenordnung des effektiven Diffusionskoeffizienten. Im Vergleich zu den Versuchen mit homogenen Sandfüllungen ist kein erheblicher Anstieg der Werte zu erkennen. Dies zeigt, dass kleinräumige Heterogenität oberhalb der Porenskala kaum Einfluss auf die transversale Dispersion hat.

Kapitel 7 beschreibt Versuche mit einem künstlichen Grundwasserleiter in einer heterogen befüllten Rinne auf technischer Skala. Insbesondere untersuche ich anhand dieser Versuche, ob die transversale Durchmischung durch die Heterogenität auf größeren Skalen verstärkt wird. Um heterogene Strukturen auf größerer Skala zu erzeugen, wurde die Rinne mit unterschiedlichen Sandgemischen in einem sedimentativen Verfahren befüllt. Dabei entstanden innerhalb größerer Linsen unterschiedlicher Sandgemische kleinräumige Sedimentstrukturen, die solchen in der Natur ähneln.

In einem konservativen Experiment mit Farbtracern injizierte ich einen Farbstoff kontinuierlich in die untere Hälfte des Einlasses der Rinne. Durch hydraulische Randbedingungen erzwang ich eine Grundwasserströmung die zur Ausprägung einer Abstromfahne führte. Im stationären Endzustand nahm ich Bilder entsprechend der in Kapitel 5 beschriebenen Methode und untersuchte Querschnitte der Konzentrationsverteilung auf zwei Weisen. Zuerst interpretierte ich die Konzentrationsprofile so, als ob sie durch stationären advektiv-dispersiven Transport mit konstanten Koeffizienten entstanden wären und bestimmte die Parameter durch Anpassen einer analytischen Lösung. Die so geschätzten Werte für die apparente lokale transversale Dispersivität schwanken räumlich zwischen 3×10^{-3} m und 1×10^{-4} m.

Die so erhaltenen Parameterwerte sind jedoch durch das Mäandrieren der Abstromfahne ziemlich verzerrt. Vor allem wird das gesamte Konzentrationsprofil beim Mäandrieren in Bereichen hoher lokaler Geschwindigkeit gestaucht und in Bereichen geringer lokaler Geschwindigkeit gedehnt. Dadurch ergeben sich in Bereichen hoher Geschwindigkeit höhere Werte für die transversale Dispersivität als in Bereichen niedriger Geschwindigkeit. Aus diesem Grund habe ich in einer zweiten Auswertung den Verlauf von Stromlinien mitberücksichtigt. Unter Berücksichtigung des Strömungsfeldes liegen die geschätzten Werte der transversalen Dispersivität bei 6.9×10^{-5} m, mit einem Variationskoeffizienten von 75%. Das hierbei verwendete Stromlinienmuster stammt von *Nowak* [2004], der mit Hilfe von geostatistischer

inverser Modellierung ein Experiment von *Jose* [2004] in der selben Rinne auswertete. Daraus erhielt er unter anderem eine Schätzung der räumlichen Verteilung der Durchlässigkeit. Abbildung 3 zeigt das geschätzte Durchlässigkeitsfeld, das damit modellierte Potentialnetz mit Strom- und Potentiallinien, und ein digitales Bild des konservativen Farbtracers in der Rinne. In diesem Bild ist das Mäandrieren der Fahne sehr deutlich zu sehen.

Abbildungen 4 und 5 zeigen die sich ergebenden Werte der transversalen Dispersivität und die vertikale Position der Randlinie der Fahne, einmal unter Vernachlässigung und einmal unter Berücksichtigung des geschätzten Stromlinienmusters. Die Auswertung unter Berücksichtigung des Stromlinienmusters ergibt wesentlich konsistentere Ergebnisse, obwohl das geschätzte Stromlinienmuster das mäandrierende Verhalten der Fahne nicht vollständig beschreibt. Dies wird darin offensichtlich, dass unter Berücksichtigung des Stromlinienmusters die Randlinie der Fahne nur teilweise gerader verläuft.

Ich führte einen weiteren reaktiven Tracerversuch (Abbildung 6) durch, wiederum unter Verwendung der Methoden aus den Kapiteln 5. Aus der Breite und Länge der Abstromfahne schätzte ich einen transversalen Dispersionskoeffizienten von 3.4×10^{-9} m²/s.

Die in der großen Rinne angetroffenen transversalen Dispersionskoeffizienten sind nicht größer als diejenigen, die ich in den homogenen und in den kleinräumig heterogenen Systemen vorgefunden habe. Daraus schloss ich, dass die Heterogenität poröser Medien lediglich einen kleinen Einfluss auf die vertikale Durchmischung hat. Dieses Ergebnis stimmt gut mit den Ergebnissen der stochastischen Theorie von *Gelhar and Axness* [1983] überein, die lediglich eine sehr geringe Skalenabhängigkeit transversaler vertikaler Dispersionskoeffizienten vorhersagen.

Allerdings verursacht Heterogenität erheblich mäandrierende Stofffahnen. Meine Experimente zeigen, dass Konzentrationsprofile für sich allein betrachtet nicht ausreichen, um transversale Durchmischung in heterogenen porösen Medien zu quantifizieren. Ohne das Strömungsfeld im fraglichen Gebiet zu kennen, kann man keine aussagekräftigen transversalen Dispersionskoeffizienten bestimmen. Unter Feldbedingungen ist die Unsicherheit des Strömungsfeldes viel höher als in wohlkontrollierten Laborexperimenten. Insgesamt ist es wesentlich zuverlässiger, Koeffizienten für die vertikale Durchmischung aus der Länge von Abstromfahnen aus reaktiven Versuchen abzuschätzen, als sie aus vertikalen Konzentrationsprofilen zu bestimmen.

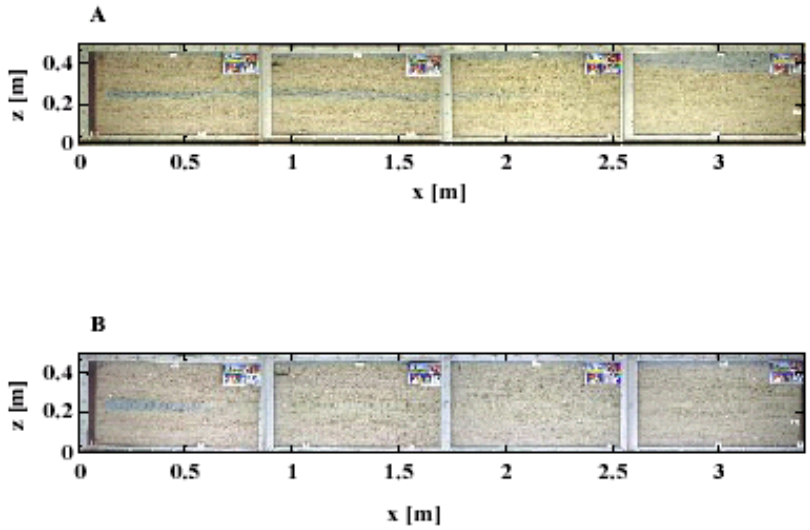

Abbildung 1: Alkalische Stofffahne im künstlichen feinstrukturierten Grundwasserleiter aus Sand mit Korngröße 0-3mm. A: Fließgeschwindigkeit $2{,}76\times10^{-5}$ m/s; B: Fließgeschwindigkeit of $1{,}65\times10^{-5}$m/s.

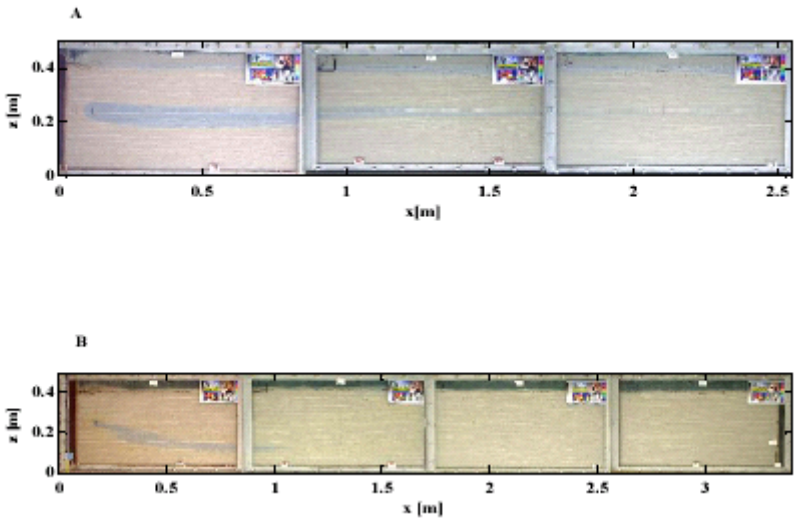

Abbildung 2: Alkalische Stofffahne im künstlichen feinstrukturierten Grundwasserleiter aus Sand mit Korngröße 0-3mm. A: Fließgeschwindigkeit $1{,}65\times10^{-5}$ m/s; B: Fließgeschwindigkeit of $1{,}1\times10^{-5}$ m/s.

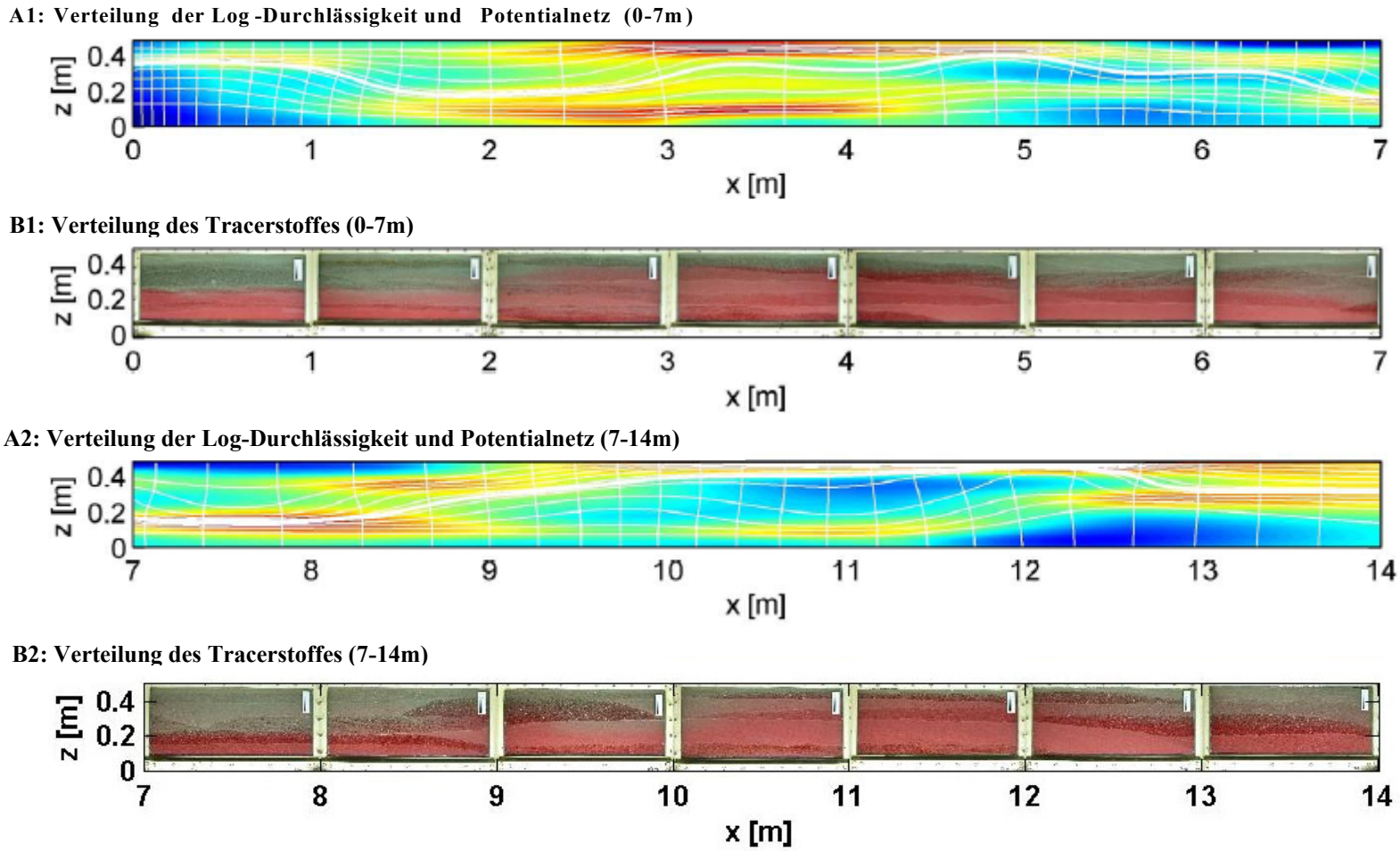

Abbildung 3: Verteilung der Log-Durchlässigkeit, berechnetes Strömungsnetz und gemessene Verteilung des konservativen Tracerstoffes im künstlichen Grundwasserleiter. Dicke Stromlinie: Mittellinie der transformierten Koordinaten.

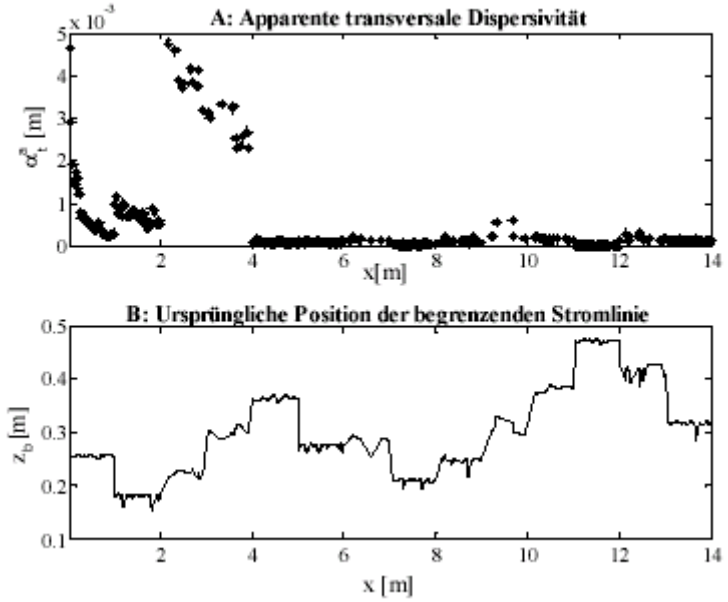

Abbildung 4: Apparente transversale Dispersivität α_t^a und vertikale Position z_b der begrenzenden Stromlinie in den ursprünglichen Koordinaten.

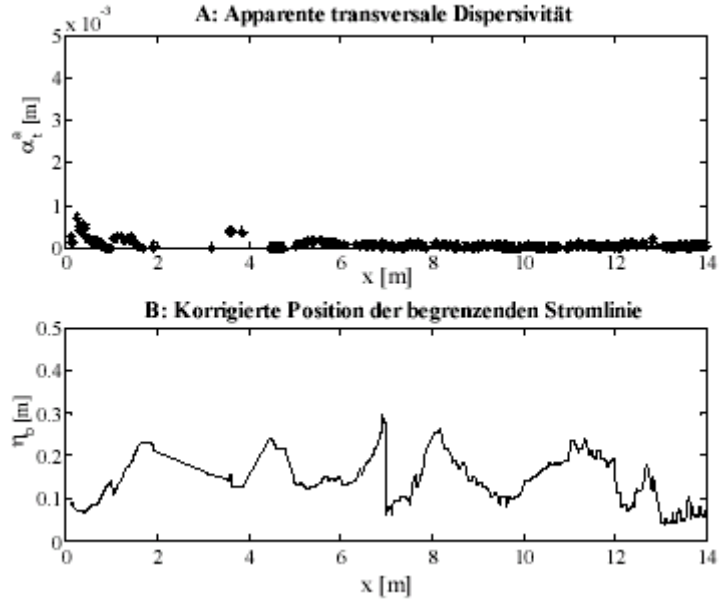

Abbildung 5: Apparente transversale Dispersivität α_t^a vertikale Position η_b der begrenzenden Stromlinie in den transformierten Koordination.

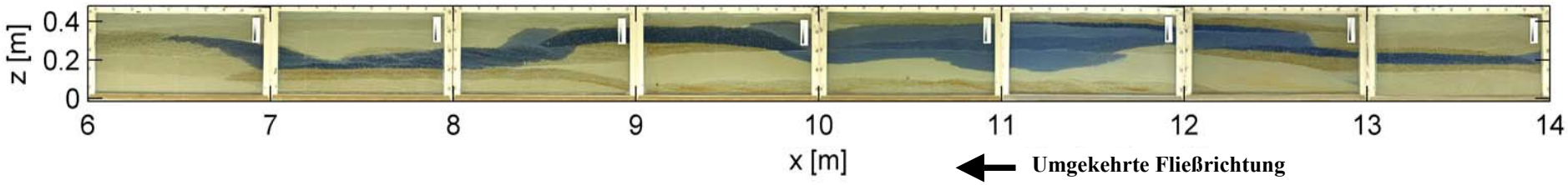

Abbildung 6: Fahne des reaktiven Tracerstoffes im künstlichen Grundwasserleiter, Quellbreite 0,05m, gemessene Länge der Fahne 7,65m.

1. Introduction

1.1. Rationale

Ground water is the main source of drinking water for two third of the world's population [*Freeze and Cherry, 1979*]. Various chemical compounds such as chlorinated and aromatic hydrocarbons, heavy metals etc. have been identified as contaminants in groundwater. Industrial sites, former gas plants, landfills and tanks, among others, have been recognized as the potential pollutant sources for the contamination of soil and groundwater.

Common active in-situ remediation strategies, like pump and treat, air sparging and soil vapor extraction, often reveal a high ineffectiveness (due to persistence contaminants and heterogeneity of the subsurface), as they cause very high costs due to long operation times while failing to achieve the remediation target. Over the last few years, the high costs of conventional remediation have encouraged the development of more effective methods for groundwater management. In this climate, interest in natural attenuation is increasing. The United States Environmental Protection Agency (US EPA) defines natural attenuation as "biodegradation, dispersion, dilution, sorption, volatilization, and /or chemical or biochemical stabilization of contaminants to effectively reduce contaminants toxicity, mobility, or volume to levels that are protective of human health and the ecosystem" [*US EPA, 1999*]. Among these processes, biodegradation is the major process for reducing contaminant mass.

A key process in bioremediation is the mixing between two substrates, namely the electron donor and acceptor. In many cases, the electron donor load of the plume is substantial, while the availability of electron acceptors is limited. Electron acceptors are replenished by transverse mixing [*Grathwohl et al., 2000; Cirpka et al., 1999*], and contaminants are reduced by dilution processes arising from transverse dispersion. Therefore, the rate of biodegradation in a steady-state plume depends significantly on the mixing processes at the fringe of the plume, that is, to a large extent on the transverse mixing of electron acceptors and organic compounds caused by transverse dispersion (Figure 1. **1**).

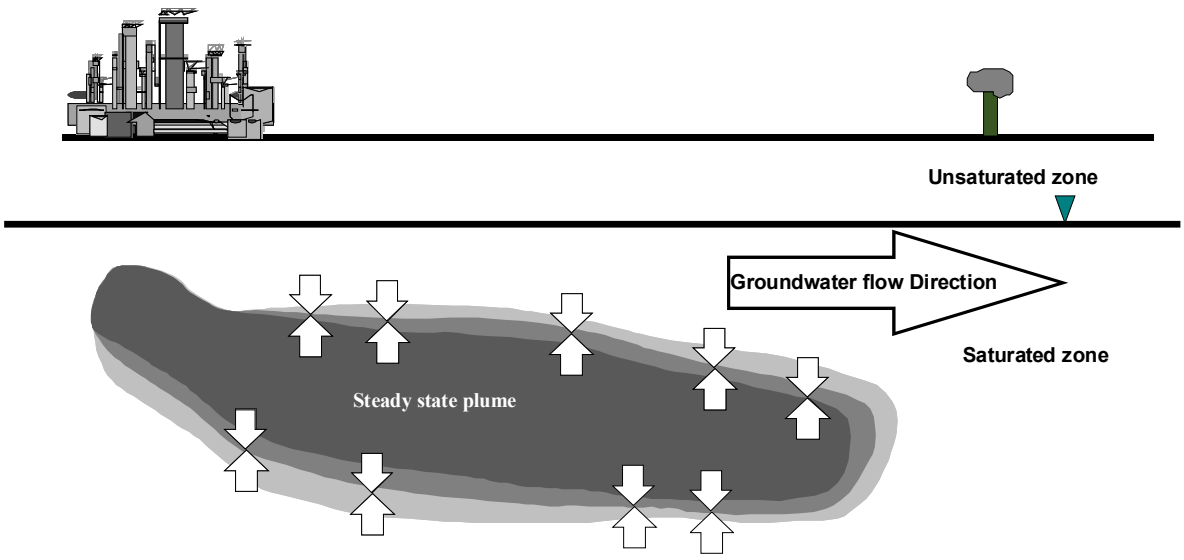

Figure 1. 1 Rate of biodegradation in a steady-state plume depends significantly on the mixing processes at the fringe of the plume as the electron donor load of the plume is substantial, while the availability of electron acceptors is limited and electron acceptors are replenished by transverse mixing.

Understanding the role of transverse dispersion in reactive mixing requires a detailed knowledge about the governing processes of flow and transport in the spatially variable natural porous medium. The fundamental and complex roles played by heterogeneity in transport of solutes in porous media have been studied in last two decades. Much of the research in recent years are directed towards the development of a more physically based mathematical description [e.g. *Gelhar and Axness, 1983*; *Dagan, 1984, 1988*; *Dagan et al., 1992*; *Kitanidis, 1994*; *Dagan and Fiori, 1997*; *Fiori and Dagan, 1999*; *Cirpka et al., 1999*; *Attinger et al., 1999*; *Cirpka and Kitanidis, 2000a, 2000b*; *Dentz et al., 2000a, 2000b & 2002*;] and targeted experimental studies [*Grane and Gardner, 1961*; *Kobus and Spitz, 1985*; *Robbins, 1989*; *Grathwohl et al., 2000*; *Klenk and Grathwohl, 2002*; *Huang et al., 2002 & 2003*] of the physical transport processes in heterogeneous aquifers.

The heterogeneity of natural formations determines the spreading of solutes in groundwater. A plume injected into an aquifer undergoes enhanced spreading because of the variation in groundwater velocity caused by permeability changes. Particularly, the plume is sheared and distorted, with fast fingers moving through zones of high conductivity and slowly displaced ones in zones of low conductivity (Figure 1.2). These heterogeneities are present at scales ranging from microscopic scale (pore-scale) to macroscopic scale (field scale). Macrodispersion describes how fast the second central spatial moments of a very large plume increases. This includes both mixing on the local scale and spreading on a larger scale. The irregularity of the interface referred to as spreading, however, is not a measure of mixing [*Cir-*

pka and Kitanidis, 2000a]. Therefore, applying Fickian macrodispersion concept to reactive transport leads to an overestimation of mixing rate [*Ginn et al., 1995, Kapoor et al., 1997*].

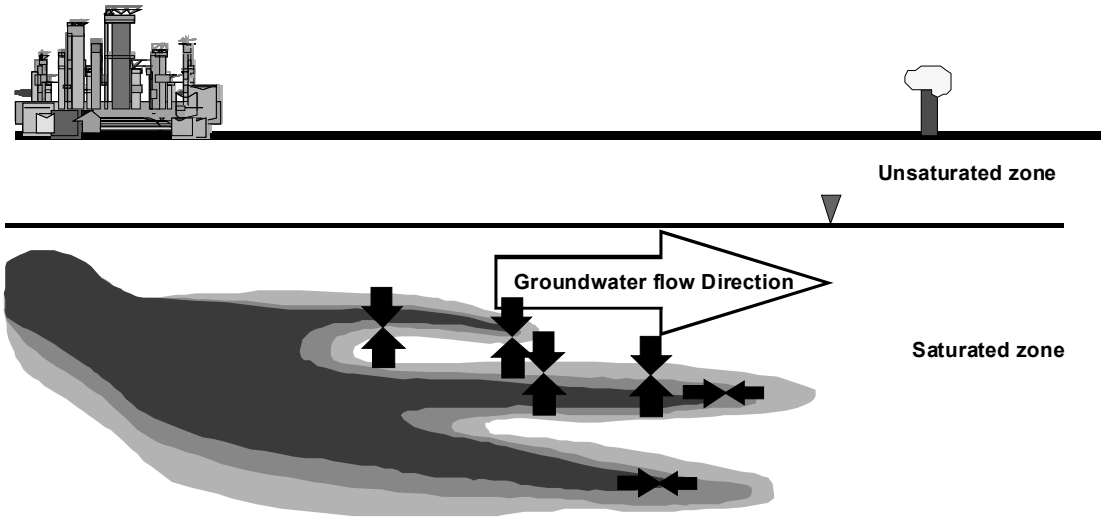

Figure 1.2 Plume injected into an aquifer undergoes enhanced spreading because of the variation in groundwater velocity caused by permeability changes. Particularly, the plume is sheared and distorted, with fast fingers moving through zones of high conductivity and slowly displaced ones in zones of low conductivity

In mixing, the important question is whether the reacting compounds occur at the same point at the same time so that they may react with each other. As biodegradation occurs due to mixing of substrates on the scale of reactions, local scale (pore-scale) dispersion may become the limiting factor for the biodegradation process [*Cirpka et al., 1999*].

The value of pore scale transverse dispersivity is much smaller than that of the related longitudinal dispersivity [*Bear, 1972*]. However, the variability of the flow fields leads to an extensive stretching of the plume interfaces [*Weeks and Sposito, 1998*], therefore transverse pore-scale dispersion acts over a much larger area than longitudinal dispersion [*Cirpka, 2002*]. Hence, it is transverse dispersion that transfers longitudinal spreading into longitudinal mixing [*Cirpka and Kitanidis, 2000a*]. For plumes originating from continuous sources, transverse mixing is more important than longitudinal mixing. The effectiveness of transverse mixing determines the length of steady-state plumes reacting with surrounding water.

Transverse dispersion is also an essential factor to predict the temporal behavior of the contaminant plume. The ratio of longitudinal to transverse dispersivity in an aquifer is an important factor to determine the shape of the contaminant plume. The lower the ratio is, the

broader the shape of the resulting plume will be. A well estimated transverse dispersion coefficient helps to predict the plume development accurately.

The work presented in this dissertation is a part of the joint research efforts in the project "Scaling Effects of in-situ Mixing in Heterogeneous Aquifers" (Skaleneffekte bei der in-situ Durchmischung gelöster Stoffe in heterogenen Grundwasserleitern) funded by the Deutsche Forschungsgemeinschaft within the Emmy-Noether-program.

Therefore, the present dissertation is motivated by the requirement for an improved understanding of the role of transverse dispersion on reactive mixing in natural heterogeneous porous medium.

1.2. Objectives

The aim of the research was to improve the understanding of the transverse dispersion phenomena in the context of reactive mixing in natural heterogeneous porous medium. This was approached using laboratory scale and technical scale experiments in homogeneous and heterogeneous model aquifer systems. The main objectives were to:

1. Develop a suitable conceptual model of dispersive transverse mixing between contaminant plumes and aqueous compounds in a groundwater system.
2. Develop methods for the determination of pore-scale transverse dispersivity.
3. Analyze the role of natural heterogeneity on transverse dispersive mixing.

1.3. Existing Measurement Methods to Determine Transverse Dispersion Coefficients

In most existing methods for the determination of transverse dispersion, the measured quantity is proportional to the dispersion coefficient; therefore, it induces significant errors in its experimental determination. *Kitagawa* [1934] was perhaps the first to perform experiments on dispersion phenomena. Transverse dispersion coefficients are typically evaluated by the interpretation of steady-state transverse concentration profiles of conservative solutes in parallel flow. Usually two miscible fluids are injected into a porous medium and the effluent concentration profiles are determined consequently. The most common system is brine and fresh water in which the concentration is determined by using conductivity resistivity meters [*Blackwell, 1962*; *Bruch, 1970*; *Kobus and Spitz, 1985*; *Robbins, 1989*; *Sudicky et. al, 1985*].

Typically two experimental methods are used to determine the transverse dispersion parameters. Two miscible fluids are simultaneously injected, side by side [Figure 1.3], [*Grane and Gardner, 1961*; *Simpson, 1962*; *Perkins and Johnston, 1963*; *Harleman and Rumer,*

1963; *Lawson and Elrick, 1972*] or into the core and annulus regions of a cylindrical porous medium [Figure 1.4] [*Blackwell, 1962*; *Bruch, 1970*; *Hassinger and Rosenberg, 1968*; *Mohanty and Salter, 1983*]. Then, the concentration profile perpendicular to the direction of flow is measured further downstream. *Robbins* [1989] used point sources, and *Nishigaki et al*. [1996] used line sources of a tracer solution. Transverse dispersion coefficients have also been inferred from transient transport in columns [*Robbins, 1989*], in parallel flow [*Zou and Parr, 1993, 1994*; *Pisani and Tosi, 1994*] and in inter-well tracer tests [*Chen et al., 1999*]. *Wang et al*., [1987] proposed a linear graphical method for estimating the dispersivity parameters based on the use of an analytical expression and comparing it to the derivatives of the experimental breakthrough curves. This method was very sensitive to erratic and noisy data obtained in the experiments. *Jiao* [1993] improved the linear graphical method and proposed the dispersive-plume-area method.

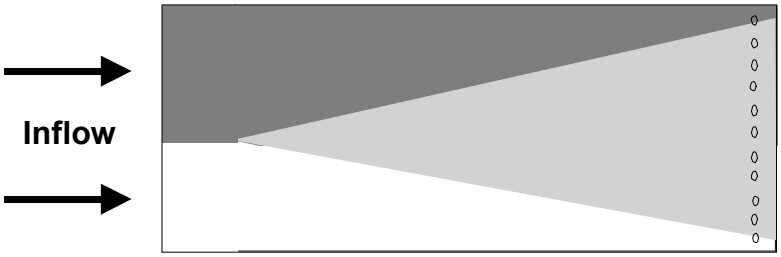

Figure 1.3 Injection of two miscible fluid simultaneously, side by side

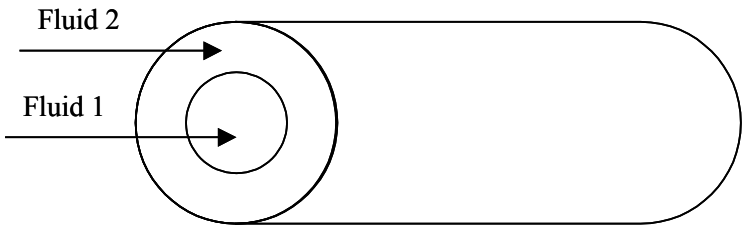

Figure 1.4 Injection of two miscible fluids into the core and the annulus region

Grane and Gardner [1961] conducted dispersion experiments with three types of glass beads at groundwater velocities between 0.14m/day and 345.6m/day. They conducted experiments in a ¾ inch Lucite box (30"×1"×2"). The first third of the box was divided into two compartments and the box was packed with glass spheres. Two miscible fluids were passed through the box at a constant rate. The distribution of fluids in the media was meas-

ured by means of a narrow x-ray beam. The transverse dispersion coefficient was calculated using the measured concentration gradient. They concluded that at sufficiently high flow rates the measured transverse dispersion coefficient was 1/50 of the longitudinal one.

Blackwell [1962] performed experiments in an unconsolidated sand packed column to measure the longitudinal and transverse dispersion coefficient. He also used a Lucite column, but he injected one fluid into the core and the other into the annulus of equal cross-sectional area. Frequent resistivity measurements of the effluent were conducted. The steady-state values for resistivity were used to calculate the fractional concentration of the salt tracer in the two streams. His results indicated that the transverse dispersion coefficient was 1/25 of the longitudinal dispersion coefficient.

Harleman and Rumer [1963] measured the dispersion of sodium chloride for laminar water flow in beds of plastic spheres with a mean diameter of 0.96mm at water velocities ranging from 10m/day to 245m/day. Two fluids, fresh water and water containing sodium chloride were co-injected into the box. They correlated the ratio of the longitudinal and transverse dispersion coefficient with the Reynolds number; the ratio was found to be proportional to the square root of the Reynolds number.

Bruch [1970] conducted two-dimensional dispersion experiments in unconsolidated porous media. A Plexiglas box was filled with sand and saturated by a source solution. A NaCl solution was used as the dispersing fluid. Conductivity probes were used to measure the tracer concentrations. Experiments were also conducted in a layered system where the Plexiglas box was filled with two sand layers of different diameters. It was concluded that one must consider the combined effect of longitudinal and lateral dispersion in the analysis of the propagation of a miscible fluid in groundwater.

Kobus and Spitz [1985] conducted an experimental investigation of the transverse vertical mixing across an initially sharp density interface in an effort to further understand the impact of contaminants in the vicinity of sources of pollution. Two parallel streams of fresh and salt water were injected into a media filled with sand grains. Vertical concentration measurements were taken downstream of the inlet by extracting probes of 1ml and measuring the probe conductivity. The transverse dispersion coefficient was then calculated from the measured concentration profiles. They concluded that density differences reduce the mixing zone length at the interface and that the contribution of density is more pronounced in the region of lower flow velocities.

Robbins [1989] followed the methodology developed by Bruch [1970] and presented methods for determining dispersion coefficients from laboratory experiments involving col-

umns packed with spherical glass beads. A continuous point source and an instantaneous finite source were used for tracer injection, concentrations were detected by a miniaturized electrical probe. The initial and steady state solute concentrations were used to calculate the transverse dispersion coefficient. He indicated that the continuous point source test appeared to be more reliable than the finite source method since it resulted in higher tracer concentrations and was less affected by measurement errors. He also showed that transverse dispersion coefficients evaluated from transient data were less accurate than those determined under steady-state conditions.

Field tracer tests were performed by *Moltyaner and Killey* [1988] with iodide in fluvial sands at groundwater velocity of 1.2m /day. *Sudicky et al*. [1983] performed tracer experiments at the Borden site and concluded that the transverse vertical dispersivity value of the site was in the order of the aqueous diffusivity. *Rajaram and Gelhar* [1991] simulated transport at the Borden site and estimated a transverse macrodispersivity value of 2.2mm. Transport simulation accounting for the heterogeneity also indicate much lower values of 0.5mm [*Hantush and Marino,1998*] and 0.44mm [*Fiori and Dagan, 1999*] for the pore scale dispersivity.

Grathwohl et al. [2000] conducted experiments to quantify the effect of transverse mixing on NAPL pool dissolution and vapor phase transport across the capillary fringe. They observed a very small vertical dispersivity. It was concluded that the mass transfer rates across the capillary fringe and the dissolution of a pool strongly depend on dispersion.

Eberhardt and Grathwohl [2000] performed large scale laboratory experiments on the long-term dissolution behavior of BTEX and PAHs from Creosote in residual phase. The experiments were carried out in an 8 m long flume filled with medium grained sand. Two different NAPL source zones (zone containing creosote at residual saturation of 5% and zone containing a 2.5 m long creosote pool at the base of the aquifer) were examined. They calculated vertical transverse dispersivity values of 0.2mm. *Klenk and Grathwohl* [2002] performed a controlled tank experiment on the transport of TCE across the capillary fringe at velocities ranging from 1.53m/day to 11.33m/day and the resultant transverse vertical dispersivity value was 0.63mm.

Huang et al. [2002] presented an imaging technique to calculate transverse dispersion coefficient. They performed laboratory experiments in a two dimensional physical model with nominal thickness. The model was packed with glass beads to form a transparent quasi two- dimensional porous matrix. Sodium Fluorescein tracer was injected through the saturated

medium with a velocity of 0.49 m/day and the images were recorded by the CCD camera. The transverse dispersivity value of 0.07mm was calculated from the observed image intensity.

1.3.1. Tasks

It has been widely accepted that pore-scale transverse dispersion plays a decisive role in the decay of concentration fluctuations, dilution of conservative solutes, and mixing of reacting compounds [*Kitanidis, 1994*; *Cirpka and Kitanidis*, *2000a*; *Attinger et al., 1999*]. But there is little direct evidence to demonstrate this process.

Many researchers have developed various physical methods to determine transverse dispersive mixing in the subsurface. In all these methods, the measured quantity is proportional to the dispersion coefficient therefore inducing significant errors in its experimental determination. No simple, efficient and satisfactory method is available until now. Hence, new methods for the determination of pore-scale transverse dispersion coefficient are developed in the laboratory scale. A technical-scale heterogeneous model aquifer system was designed to investigate transverse dispersive mixing. MATLAB written codes were used to simulate experimental results.

The steps followed in this research are summarized as:

1. Developing a novel method to determine pore-scale transverse dispersivity by Taylor-Aris dispersion in a helical soil column,
2. Designing quasi two dimensional laboratory-scale and technical scale heterogeneous model aquifer systems,
3. Developing a non-invasive imaging technique to determine transverse dispersivity from tracer experiments,
4. Conducting reactive experiments to quantify the effect of micro-heterogeneity on transverse reactive mixing.
5. Conducting conservative and reactive experiments to quantify the impact of macro heterogeneity on transverse dispersive mixing.

1.4. Scope and Structure of Dissertation

This dissertation is divided into two main parts. The first part includes the theoretical background of transverse dispersive mixing, the materials and methods used in the study (chapter 2 and chapter 3), whereas the second part comprises the results of the different experiments, modeling approaches and their discussions (chapter 4 to chapter 7).

Chapter 1 describes the rationale and objectives of the research and gives a brief review of the existing measurement methods.

Before addressing the details of the materials and measurement techniques used in the study, chapter 2 provides a brief description of the reactive dispersive mixing phenomena on the microscopic and macroscopic scale. Groundwater flow and solute transport equations are also presented. The chapter includes a brief review of stochastic theory in subsurface hydrology and of different existing approaches on dispersion phenomena.

Chapter 3 describes in detail the filling materials, tracers, the design of the experimental domain, and different measurement techniques used in the study. As a requirement to measure local concentration [*Cirpka and Kitanidis, 2000a*], point measurement techniques developed by *Jose* [2004] were used and a new non-invasive imaging technique was developed for determining transverse dispersive mixing in porous medium. The experimental setup for both one-dimensional column experiment and quasi two-dimensional laboratory scale and technical-scale experiments are presented here.

Chapter 4 describes a novel method developed for the determination of pore scale dispersivity by Taylor-Aris dispersion in a specially designed helical soil column. It includes the flow and transport behavior and the assumptions applied to the helical soil column. Results of both experimental and numerical modeling are discussed.

Chapter 5 presents a method to determine the transverse dispersion coefficient in a homogeneous porous medium by measuring the length of a reactive plume. Here, a non-invasive imaging technique is developed.

Chapter 6 describes the impact of microheterogeneity on transverse dispersive mixing. Here, I discuses the experimental results of reactive tracer tests performed in the laboratory scale model aquifer filled by different sand mixtures that exhibits microscopic sedimentary structures.

Chapter 7 demonstrates the influence of macroscopic heterogeneity on transverse mixing. Here, I present the experimental results of both the conservative and reactive tracer tests performed in the technical-scale model aquifer which exhibits macroscopic heterogeneity.

Summary and Conclusions of the dissertation are presented in Chapter 8.

2. Theoretical Background

This chapter provides the theoretical description of reactive dispersive mixing phenomena on both the local and macroscopic scale. The equations of groundwater flow and solute transport in the subsurface are given. Also, I briefly review stochastic theory in subsurface transport. The chapter also summarizes the different existing approaches on dispersion phenomena.

2.1. Reactive Mixing Process

Two dissolved compounds, that initially occupy separate volumes in an aquifer, must mix in order to react with each other. Only when the reacting compounds are present at the same point at the same time, a reaction may occur. A lack of mixing limits therefore the transformation of contaminants [*Kitanidis, 1994*; *Miralles- Wilhelm et al., 1997*; *Kapoor et al., 1997*; *Oya & Valocchi, 1998*; *McCarty et al., 1998*; *Dybas et al., 1998*; *Cirpka et al., 1999a*; *Miralles Wilhelm & Gelhar, 2000*]. Three mixing processes on the scale of the smallest possible representative elementary volume [*Bear, 1972*] were identified by *Cirpka et al.* [1999] - chromatographic mixing, kinetic mass transfer and dispersion. In contrast to the other two mixing processes, dispersion is the active mixing process even if no mass transfer occurs, and it acts into the principal direction of flow as well as transverse to it.

2.2. Dispersion

Dispersion consists of molecular diffusion and pore-scale dispersion. The complicated system of interconnected passages comprising the microstructure of the medium causes a continuous subdivision of the compound's mass into finer offshoots. Variations in local velocity, both in magnitude and direction, along the tortuous flow paths and between adjacent flow paths within each pore, cause any initial compound mass to spread and occupy an ever-increasing volume of the porous medium.

The mixing/spreading that occurs along the direction of the flow path is called **longitudinal dispersion** (Figure 2.1) and the spreading in directions normal to the flow is called **transverse dispersion (**Figure 2.2**).** In both longitudinal and transverse direction, the dispersion results from an interplay between advection and diffusion.

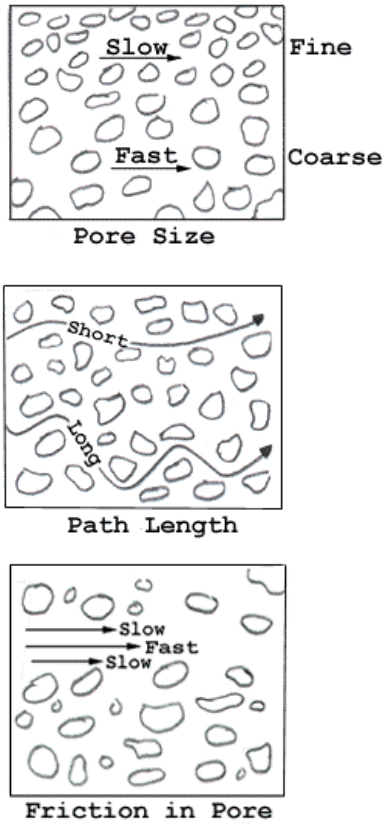

Figure 2.1 Factors causing longitudinal dispersion at the scale of individual pores (Fetter, C. W. 1994)

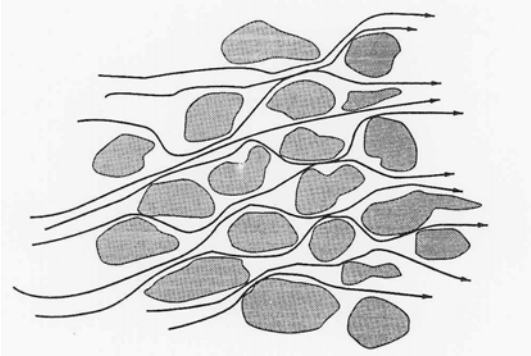

Figure 2.2 Flow path in porous media causes transverse dispersion

Classically, transverse dispersion includes two components: transverse mechanical dispersion and diffusion. It is commonly parameterized by [*Fetter, 1993*]:

$$D_T = \alpha_T v + D_e^* \qquad (2.1)$$

where, D_T is the transverse dispersion coefficient, D_e^* is the effective diffusion coefficient, α_T is the transverse dispersivity and v is the seepage velocity. In general, three factors (various pore sizes, tortuosity and a velocity distribution in a single pore) are responsible for pore-

scale mechanical dispersion [*Bear, 1972*; *Weidemeier et al., 1999*], and the dispersivity is a characteristic quantity of porous media. Molecular diffusion is driven by intrinsic molecular thermal movement and may be described by Fick's law. Molecular diffusion in porous media depends on the temperature, solute properties and pore size. *Grathwohl* [1998] presented an empirical equation for the estimation of the diffusion coefficient:

$$D_e^* = D_{aq}\theta_e^{\omega-1} \qquad (2.2)$$

where D_{aq} is the diffusion coefficient in the aqueous phase, θ_e is the porosity and ω is an empirical exponent ranging between 1.8 and 2.4.

Taylor [1953], in his analysis of longitudinal dispersion in capillary tubes, obtained D proportional to $\bar{v}^{-2}$. *Bear and Todd* [1960], in their one-dimensional analysis of porous media, suggest $D = a_1\bar{v}$, i.e., D is proportional to $\bar{v}$, with a_1 being some characteristic medium length.

Scheidegger [1957] summarized his analysis on the two possible relationships between D and $\bar{v}$ according to the role played by molecular diffusion: (a) $D \approx a'\bar{v}^{-2}$, where a' is a constant of the porous medium alone (dynamic dispersivity), which is derived by a dynamic procedure applicable where there is enough time in each flow channel for appreciable mixing to take place by molecular transverse diffusion; (b) $D \approx a''\bar{v}$, where a'' is another constant of the porous medium (geometric dispersivity), which is derived by a geometric procedure applicable where there is no applicable molecular transverse diffusion from one streamline to another.

Thus in all models in which the combined effect of velocity distribution across a channel and transverse molecular diffusion is considered [e.g., *Taylor 1953*], the coefficient of dispersion is proportional to $\overline{v^2}$. Where only the mean motion in a channel is considered, while mixing occurs at junctions connecting different channels, disregarding molecular diffusion one obtains $D \approx \bar{v}$. Of course, intermediate cases, where D is proportional to some power of the velocity between 1 and 2, lie between these two extremes. *Klenk and Grathwohl* [2002] suggest that vertical α_T apparently declines with increasing flow velocities. According to them, the incomplete diffusive mixing in the pore throats leads to an exponent smaller than one, i.e., $D \approx \alpha_T v^n, n < 1$.

2.3. Mechanism of Pore-Scale Transverse Dispersion

The individual streamlines follow a tortuous path through the porous medium although the average direction of each streamline must be in the direction of mean flow. The paths followed by various streamlines vary widely in direction for distances in the order of the diameter of the sand grain. The lateral motion of a particle along these streamlines, combined with the diffusive exchange of particles between streamlines both within the individual flow channels and at junctures, give rise to transverse mixing. Two factors can cause a fluid particle to transfer from one streamline to another: (1) molecular diffusion or (2) turbulent eddies which disrupt the streamlines. For very low Reynolds numbers, however, mixing between streamlines is caused predominantly by molecular diffusion since the formation of turbulent eddies is negligible [*Blackwell, 1962*].

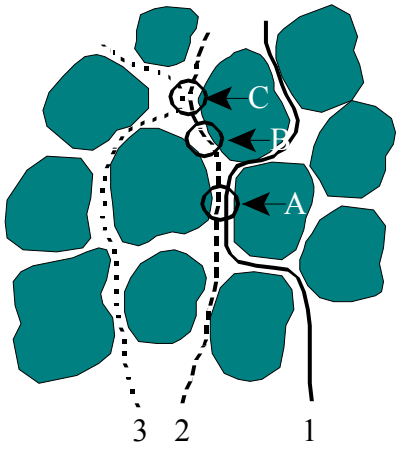

Figure 2.3 Mechanism of Transverse Dispersion **(***after Blackwell, 1962***)**

The microscopic mixing processes can be described conveniently by discussing the transport of tracer molecules through the porous medium. The mechanism of transverse dispersion is illustrated in (Figure 2.3) as illustrated by *Blackwell* [1962]. Tracer molecules are initially injected into streamline 1. As they flow along this streamline, molecular diffusion tends to distribute the particles uniformly across the flow channel analogous to that described by Taylor for a single capillary. Near region A some of the particles transfer from streamline 1 to streamline 2. Subsequently, the particles are transported laterally along streamline 2 through region B and approach streamline 3 near region C. At very low flow rates, transport of tracer particles through region B is predominantly carried out by molecular diffusion. As the mean flow rate increases, however, advective transport through region B becomes more important and eventually determines the minimum time required for the particles to reach

region C. In the vicinity of region C some of the particles transfer to streamline 3 to continue the transverse dispersion process.

At very low rates, transverse mixing is dominated by molecular diffusion. Although the velocity variation perpendicular to the mean flow are smaller than those parallel to it, the transverse mixing area will tend to be much greater than the area of longitudinal mixing, at the large-time limit. Both transverse and longitudinal mixing are independent of the viscosity because effects of inertia or eddy mixing are negligible at low Reynolds numbers [*Blackwell*, 1962].

2.4. Importance of Macroscopic and Pore-scale Transverse Dispersion

Dispersivities are seen to increase with scale of observation [*Gelhar et al., 1992*]. Therefore, as a plume grows and develops, its rate of spreading both longitudinally and transversely appears to increase. While pore-scale transverse dispersion is caused by variations of pore sizes, tortuosity, and variable friction within an individual pore [*Bear 1972*, *Weidemeier et al.*, 1999], macrodispersion is attributed to by macroscopic heterogeneity (e.g. stratigraphy, grain size distribution and permeability variations) rather than pore-scale heterogeneity [*Zheng and Bennett, 1995*].

On the field scale, macroscopic dispersion controls the spreading of the non-reactive plume components. *Gelhar and Axness* [1983] and *Dagan* [1988] showed that solute dispersion is a anisotropic process in natural heterogeneous media even under steady-state flow conditions. Therefore as a plume grows and develops, its rate of spreading both longitudinally and transversely (as an observational phenomenon) would appear to increase. When modeled as a continuum process, this requires that the dispersivity is not a constant but varies with distance traveled and implied that dispersion is a cumulatively increasing process.

In contrast to longitudinal macrodispersivity, transverse macrodispersivity approaches an asymptotic value only slightly larger than the pore-scale coefficient. Authors like *Attinger et al*., [1999] and *Dentz et al*., [2000] claimed that effective transverse dispersion, the parameter of actual mixing also show the similar behavior. Therefore, slow transverse dispersive mixing will determine the large time quasi steady-state behavior of the plume.

It is well accepted that natural heterogeneity governs the spreading of solutes in groundwater. The effect of natural heterogeneity in hydraulic conductivity on transport of conservative solutes has been studied intensively, namely by stochastic methods [*Gelhar & Axness, 1983*; *Dagan, 1984*; *Neuman et al., 1987*]. The previous studies were focused to understand the relationship between the geostatistical parameters describing the hydraulic-

conductivity distribution, and macrodispersion. Technically, macrodispersion coefficients measure how the expected second central spatial moments of a conservative tracer increase at field scales. They quantify the combined effect of two inter-related processes: spreading and dilution.

Spreading is associated with the increasing irregularity of the plume shape due to the spatially variable advection caused by variable hydraulic conductivity (Figure 2.4*a*). However, if advection was the only transport process, the volume of the plume would not change and local concentrations were binary, equaling the original plume concentration within the plume and zero outside of it.

By contrast, dilution describes the decrease of the actual concentration peak of a conservative solute as the mass is distributed over a larger volume. *Kitanidis* [1994] defined measures of plume dilution and *Kapoor & Kitanidis* [1996; 1998] showed the relation between dilution and the decay of concentration fluctuations. The driving force of dilution is diffusion that smoothes concentration differences. Figure 2.4*b* illustrates the effect of diffusion on a rectangular solute plume in a homogeneous flow field. The sharp concentration contrast disappears, the concentration in the original water body decreases, and the solutes occupy a large body.

In case of groundwater flow, both varying advection and diffusive processes are present which leads to extensive stretching of the plume interfaces. This leads to an extended surface area of the plume exhibiting high concentration gradients. As a consequence, diffusion can be more effective, and dilution is stronger in a spatially varying velocity field than in a uniform one. As spreading creates more interfaces, dilution increases and eventually catches up with spreading. The speed at which dilution approaches equilibrium with spreading depends on the heterogeneity of the flow field and on local dispersion whereas spreading alone is hardly influenced by the latter. Figure 2.4*c* illustrates the combined effects of spreading and diffusion.

Many researchers showed that the spreading of the large solute plumes i.e. macrodispersion in conservative studies could accurately be predicted by linear stochastic theory [*Gelhar and Axness, 1983*; *Neuman et al., 1987*; *Dagan, 1988*]. *Cirpka and Kitanidis*, [2000a], however, demonstrated that macrodispersion includes both mixing on the local scale and spreading on a large scale. Hence, applying the Fickian macrodispersion concept to reactive transport means that we merge mixing and spreading, thus we arriving at too large effective reaction rates [*Molz and Widdowson, 1988*; *Ginn et al., 1995*; *Kapoor et al., 1997*].

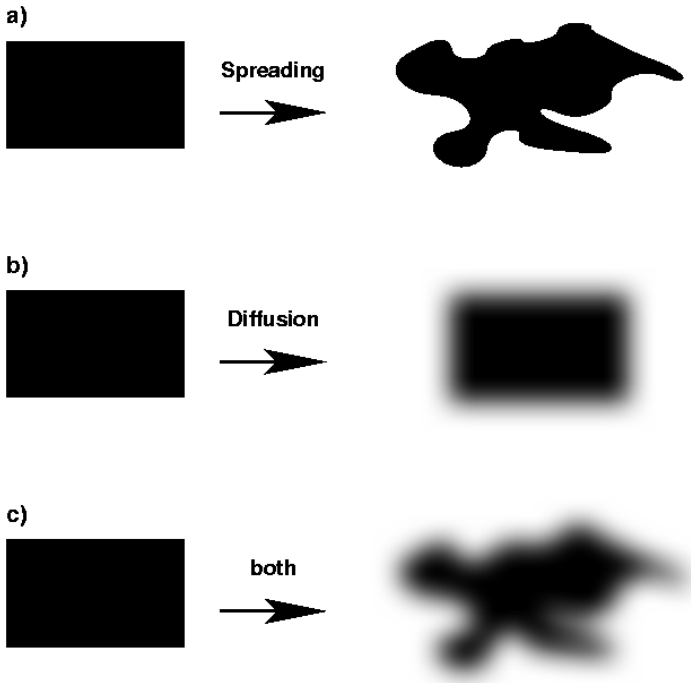

Figure 2.4 Effects of spreading and diffusion on the transport of a rectangular solute cloud.

The stochastic-convective model [*Simmons et al., 1995*] was applied to bio-reactive model problems [*Ginn et al., 1995*; *Xin and Zhang, 1998*; *Cirpka and Kitanidis, 2001a*] where mixing was determined by differences in sorption behavior of the reacting compounds [*Oya and Valocchi, 1998*] and local scale dispersion was neglected. But local dispersion is the only mixing process between the compounds when they do not sorb or undergo any interphase mass transfer. Hence, in cases without sorption the stochastic-convective approach is no more applicable to reactive transport.

The stochastic-convective approach was extended by *Ginn* [*2001*] to include longitudinal pore-scale dispersion. However, *Kitanidis* [1994] showed that spatially variable flow fields lead to extended plume interfaces, so that transverse pore-scale dispersion acts over a much more area than longitudinal pore-scale dispersion. The effect of transverse pore-scale dispersion on longitudinal pore-scale dispersion was quantified by the second central moment of conservative breakthrough curves obtained from point measurement [*Cirpka and Kitanidis, 2000b*].

Cirpka [2002] claimed that the effective dispersion coefficient for a point-like injection is an adequate measure of actual dispersive mixing, even for wide plumes. As mixing occurs on the scale of single pores, it is irrelevant how the second central moments of a wide

plume increase, since these moments primarily describe the irregularity of the plume shape. By contrast, the point related effective dispersion coefficients describe the expected area influencing the concentration at a point. Hence, for mixing-controlled reactive transport, the effective dispersion coefficient for a point-like injection quantifies dispersive mixing, whereas additional spreading of a large plume is quantified by the corresponding covariance matrix of first moments [*Cirpka and Kitanidis, 2000b*; *Cirpka, 2002*].

Therefore, the accurate choice of dispersion coefficient is of greater practical significance in predicting rates of natural attenuation or biodegradation. Further investigation into the observed magnitudes of macroscopic and pore-scale dispersion is therefore required as a precursor to evaluating the significance of the actual magnitude of dispersion relevant to reactive fringe mixing in a heterogeneous porous media.

2.5. Governing Equations of Flow and Transport in the Subsurface

2.5.1. Darcy's Law

In 1856, Henry Darcy presented the basic law describing flow in a porous medium. The law states that the flow of water through a column filled with sand is proportional to the cross-sectional area and the head loss along the column and inversely proportional to the column length. In multi-dimensional systems, Darcy's law can be expressed in vector form:

$$\mathbf{q} = -\mathbf{K}\nabla \mathrm{h} \tag{2. 3}$$

in which $\mathbf{q}$ is the specific discharge, $\mathbf{K}$ is the hydraulic conductivity tensor, and h is the hydraulic head.

The hydraulic conductivity, $\mathbf{K}$, is defined as the measure of capacity of a porous media to transmit water [*Fetter, 1993*]. It can have different values depending upon the actual direction of water flow through the porous media. If the hydraulic conductivity is identical in all directions, i.e. $K_x = K_y = K_z = K$, the medium is isotropic. Otherwise it is anisotropic, and $\mathbf{K}$ is a full tensor.

Since the actual flow takes place only in the pores, the average flow velocity, or seepage velocity, $\mathbf{v}$, is greater than the specific discharge, $\mathbf{q}$. The two quantities are related to each other by

$$\mathbf{v} = \frac{\mathbf{q}}{\theta_e} \tag{2. 4}$$

where θ_e is the effective porosity of the porous medium.

Darcy's law is valid only when the pore sizes are much smaller than the characteristic dimensions governing the flow field and also the flow has to be laminar.

2.5.2. Groundwater Flow Equation

The law of mass conservation states that the rate of change of fluid mass is given by the divergence of mass fluxes and internal sources or sinks of fluid mass.

$$\frac{\partial(\rho_w \theta_e)}{\partial t} + \nabla \cdot (\rho_w \mathbf{q}) = q_{in} - q_{out} \tag{2. 5}$$

where ρ_w = water mass density of water (M/L^3)

Since the spatial gradient of the fluid density ρ_w is negligible, we can write,

$$\frac{1}{\rho_w}\frac{\partial(\rho_w \theta_e)}{\partial t} + \nabla \cdot \mathbf{q} = q_{in} - q_{out} \tag{2. 6}$$

We may substitute Darcy's law, eqn (2.3) in the above equation, leading to

$$S_s \frac{\partial h}{\partial t} \nabla \cdot (\mathbf{K} \nabla h) = q_{in} - q_{out} \tag{2. 7}$$

with the specific storage coefficient, $S_s = \frac{\theta_e}{\rho_w}\frac{\partial \rho_w}{\partial h} + \frac{\partial \theta_e}{\partial h}$

For an incompressible fluid and a medium with constant porosity, the above equation reduces to

$$\nabla \cdot (\mathbf{K} \nabla h) = q_{in} - q_{out} \tag{2. 8}$$

2.5.3. Solute Transport Equation

In solute transport, we consider the conservation of the solute mass within the pore space. Then, the corresponding density of the conserved extensive quantity is the mass of the solute per unit bulk volume:

$$\rho^* = c\theta_e \tag{2. 9}$$

in which *c* is the concentration, i.e. the solute mass per unit volume of water. The flux density consists of two components, the advective contribution, which is caused by the movement of water carrying the dissolved compound with it, and the dispersive flux smoothing concentration differences:

$$\mathbf{f}^* = c\mathbf{q} - \theta_e \mathbf{D} \nabla \mathbf{c} \tag{2. 10}$$

in which **D** is the dispersion tensor. In stagnant water, **D** reduces to the effective diffusion coefficient D_e^*, for which the mass-flux density is described by Fick's first law. In porous media, the effective diffusion coefficient $\mathbf{D}_e^*$, is smaller than the molecular diffusion coefficient, because diffusing particles have to go around the grains (tortuosity) [*Carman, 1937*]. At a significant strength of flow, the molecular contribution to dispersion becomes negligible. Instead, velocity fluctuations at the pore scale, that have disappeared by assuming a specific discharge vector averaged over many pores, cause a mean flux that is formally equivalent to anisotropic diffusion.

Velocity fluctuations on much larger scales than the pore scale lead to similar effects in macroscopic transport. Here, we consider only the fluctuations on scales smaller than the Darcy scale.

We define our source and sink terms:

$$s^* = \theta_e r + c_{in} q_{in} - c q_{out} \tag{2. 11}$$

in which r is a reaction term, q_{in} describes the source of solute mass due to compounds dissolved in water entering the control volume as internal volumetric source, whereas the water flux q_{out} leaving the control volume carries the solute with concentration c with it. Substituting Eqs. (2.9 – 2.11) into the differential form of general conservation equation, yields the transport equation:

$$\frac{\partial(c\theta_e)}{\partial t} + \nabla \cdot (c\mathbf{q} - \theta_e \mathbf{D} \nabla c) = \theta_e r + c_{in} q_{in} - c q_{out} \tag{2. 12}$$

We may analyze Eq. (2.12) by applying the chain rule of differentiation to the divergence of the advective flux:

$$\theta_e \frac{\partial c}{\partial t} + c \frac{\partial \theta_e}{\partial t} + \mathbf{q} \cdot \nabla c + c \nabla \cdot \mathbf{q} - \nabla \cdot (\theta_e \mathbf{D} \nabla c) = \theta_e r + c_{in} q_{in} - c q_{out} \tag{2. 13}$$

which is equivalent to:

$$\frac{\partial c}{\partial t} + \frac{q_{in}}{\rho_w} \frac{\partial \rho_w}{\partial t} c + \frac{\mathbf{q}}{\theta_e} \cdot \nabla c - \frac{1}{\theta_e} \nabla \cdot (\theta_e \mathbf{D}) = r + \frac{c_{in} q_{in}}{\theta_e} \tag{2. 14}$$

In which we made use of the simplified continuity equation. Using the seepage velocity, eq. (2.3) becomes:

$$\frac{\partial c}{\partial t} + c \frac{1}{\rho_\omega} \frac{\partial \rho_\omega}{\partial t} + \mathbf{v} \cdot \nabla c - \frac{1}{\theta_e} \nabla \cdot (\theta_e \mathbf{D} \nabla c) = r + (c_{in} - c) \frac{q_{in}}{\theta_e} \tag{2. 15}$$

Under steady-state flow conditions without internal volumetric sources or sinks, the specific discharge field is free of divergence. If we assume additionally that the volumetric

water content θ_ω is uniform, the transport equation of conservative solutes simplifies further to:

$$\frac{\partial c}{\partial t} + \mathbf{v} \cdot \nabla c - \nabla \cdot \left(\mathbf{D} \nabla c \right) = 0 \qquad (2.\ 16)$$

This version of the transport equation is valid for both porous media and other types of flow systems but it requires the following assumptions:

- steady state flow, or at least a negligible compressibility of the fluid,
- a uniform volumetric water content,
- and the absence of internal volumetric sources.

2.6. Subsurface Transport on the Macroscopic Scale

2.6.1. Stochastic Approach

Natural processes are subject to a considerable variability, resulting in both spatial heterogeneity of naturally formed materials (e.g. sedimentary structures) and temporal variability of ongoing processes. As a consequence, describing processes occurring in nature, like flow and transport in the subsurface, requires knowledge of the spatial and temporal distribution of the parameters involved. Classical engineering approaches describe only the largest and most distinct hydrogeological structures by the definition of zones and layers in (numerical) models [*McDonald & Harbaugh, 1988*]. Within a certain structure, the hydraulic parameters are assumed uniform. One of the arguments supporting such models is the consideration that natural formations are generated by processes that create distributions of geological homogeneous units (facies), and heterogeneities result from the intertwined arrangement of facies that are characterized by a hierarchy of scales. While these models have been shown valuable in groundwater-flow studies, their predictive capabilities in solute transport are limited. Traditionally, the impact of heterogeneities that are smaller than the defined zones is accounted for by constant macrodispersion parameters [*Freeze & Cherry, 1979*].

Two major approaches have evolved in order to describe with the heterogeneity of subsurface parameters: genetic and strictly geostatistical models [*Koltermann & Gorelick, 1996*]. Genetic models try to simulate the sedimentation or other geological processes creating the subsurface structures, whereas geostatistical models view the distribution of the quantities of interest as the results of a random spatial process, independent of sedimentological or other geological insights on the genesis of the formation. The simulated distribution of hydraulic

properties may be more realistic when using the genetic models, but the geostatistical methods have the following advantages:

- Measured data can be included easily in the simulation of fields (conditioning), the uncertainty associated with each distribution of properties can be quantified,
- geostatistical parameters of flow and transport can be inferred from those of the hydraulic conductivity by analytical methods,
- the distribution of hydraulic conductivity can be estimated from flow and transport data (inverse modeling), including measures on the estimation uncertainty.

In all practical applications, we are not able to define the exact distribution of the hydraulic conductivity field. Therefore, it is impossible to predict flow and transport in all details. Even if we knew the exact conductivity distribution, the practical use of detailed flow and transport information would be doubtful. Therefore, the objective of stochastic hydrology is to describe the mean flow and transport behavior, whereas details such as the definite concentration at a single point and time are not considered and cannot be predicted.

Intuitively, one would define the mean as a spatial average [*Kitanidis, 1992*; *Wang & Kitanidis, 1999*]. The more common approach in stochastic hydrology, however, is to apply ensemble-averaging based on the following principles:

- The hydraulic log-conductivity field is a random spatial function.
- An infinite number of fields, referred to as realizations, share the geostatistical parameters of the true distribution which remains unknown.
- Flow and transport "calculations" are performed for each possible realization under identical boundary and initial conditions.
- The mean hydraulic head and concentration is obtained by averaging at identical location and time over all possible realizations. That is, the mean is the expected value.

Spatially varying parameters of naturally occurring materials often exhibit two important characteristics [*Journel and Huijbergts, 1978*]: they show a high degree of variability but nevertheless reveal a certain spatial structure. *Matheron* [1971] termed them regionalized variables. They can be described by means of random variables that account for the spatial structure i.e. a regionalized variable is the realization of a random function. According to the stochastic notation [*Journel and Huijbergts, 1978*; *de Marsily, 1986*; *Gelhar 1993*; ; *Dagan and Neuman 1997*] the spatial distribution of a parameter observed in the domain U is the result of a random process, that can be described by a random function. The observed distribution represents therefore one possible realization of the random function. A random

bution represents therefore one possible realization of the random function. A random function is a set of random variables corresponding to the points of the domain U under study.

A random variable is often characterized by its first two moments, the expected value $E[Z(\mathrm{x})]$ *and the* var*iance* $\sigma^2_{z(x)}$.

$$\mu_z(\mathbf{x}) = E[\,Z(\mathbf{x})] \tag{2. 17}$$

$$\sigma^2_{z(x)} = E\left[\left(z(\mathrm{x}) - \mu(\mathrm{x})\right)^2\right] \tag{2. 18}$$

The second important characteristic of a regionalized variable is its spatial structure [*Journel and Huijbergts, 1978*]. We may treat spatially distributed variables like sets of multiple variables with a single value for each location x. Then the autocovariance $\mathbf{R}_{zz}$ is defined by:

$$\mathbf{R}_{zz}(\mathbf{x},\mathbf{x}') = \mathrm{E}\left[\left(Z(\mathbf{x}) - \mathrm{E}[Z(\mathbf{x})]\right)\left(Z(\mathbf{x}') - \mathrm{E}[Z(\mathbf{x}')]\right)\right] \tag{2. 19}$$

Evaluation of the autocovariance function requires that the mean is known. An alternative measure is the (semi) variogram defined by:

$$\gamma(\mathbf{x},\mathbf{x}') = \frac{1}{2}\mathrm{E}\left[\left(Z(\mathbf{x}) - Z(\mathbf{x}')\right)^2\right] \tag{2. 20}$$

Spatially varying parameters appearing in the flow and transport equations can be described with the concept of random functions, thus leading to a stochastic description of the dependent variables, e.g. head and concentration. However, two important assumptions on the used random functions are made. One is the stationarity of the random function which means that its statistical properties are independent of **x**. As a consequence, the statistical characteristics like the first two moments of a random variable can be obtained from pooling together observations taken at different locations in space. The second important assumption is that of ergodicity defined as follows [*Marsily, 1986*]:

"Ergodicity implies that the unique realization available behaves in space with the same probability density function (pdf) as the ensemble of possible realizations. In other words, by observing the variation in space of the property, it is possible to determine the pdf of the random function for all realizations."

As ergodicity is a characteristic of the random function and not of a single realization observed in the field, it is difficult to prove ergodicity in a given domain. Nevertheless, for most applications both stationary and ergodicity are assumed. Different approaches exist to solve stochastic differential equations, which are described in detail e.g. by *Marsily* [1986] and *Gelhar* [1993].

In non-stationary media, $\overline{Z}$ or $R(\mathbf{x},\mathbf{x}')$ vary in space. The use of a spatially variable mean can easily be incorporated into interpolation, conditional simulations and inverse modeling [*Kitanidis, 1995*; *McLaughlin & Townley,* 1996; *Kitanidis, 1997*], whereas it complicates the stochastic analysis of flow and solute transport [*Li & McLaughlin, 1991*; *Neuman, 1993*; *Rubin & Seong, 1994*; *Li & McLaughlin, 1995*; *Indelman & Rubin, 1995*; *Indelman & Rubin, 1996*; *Zhang et al., 2000*].

By using the covariance or the variogram, we rely on two-point statistics that are limited in describing the typical shape of geological features. In petroleum engineering, e.g., multi-phase flow model results are extremely sensitive to connected high-permeability zones that might not be covered by two-point variograms. Extensions of the geostatistical analysis may therefore include connectivity measures or the joint correlation between multiple points [*Isaaks & Srivastava, 1988*; *Deutsch & Journel, 1992*;*Wang, 1996*]. The resulting permeability fields created by conditional simulations are more realistic, however, the reliable determination of multiple-point statistical parameters require a large number of measurements that are not available in most groundwater applications.

2.6.2. Statistical Moments

Imagine for a moment we were able to measure the exact concentration distribution of a plume in a heterogeneous aquifer. Heterogeneities make the plume extremely irregular in shape. Rather than studying the exact distribution, we may analyze the plume by its spatial moments. The breakthrough curves obtained both at points within the domain and the average at the outflow boundary can also be characterized by temporal moments. The definitions of spatial and temporal moments are presented in Table 2. 1

Table 2. 1 Identities of Spatial and Temporal Moments

Identities	Moments
$\mu_0(t) = \int_{V_\infty} c(\mathbf{x},t)dV$	zeroth spatial moment of the concentration distribution
$\mu_i(t) = \int_{V_\infty} x_i\, c(\mathbf{x},t)dV$	first spatial moment in direction x_i
$\mu_{ij}(t) = \int_{V_\infty} x_i\, x_j\, c(\mathbf{x},t)dV$	second non-central moment in the directions x_i and x_j
$\mu_{ij}^c(t) = \int_{V_\infty} \left(x_i - \overline{x_i}\right)\left(x_j - \overline{x_j}\right) c(\mathbf{x},t)\, dV = \mu_{ij}(t) - \frac{\mu_i(t)\,\mu_j(t)}{\mu_0(t)}$	second central spatial moment
$m_0(\mathbf{x}) = \int_{t=0}^{\infty} c(\mathbf{x},t)\, dt$	zeroth temporal moment
$m_1(\mathbf{x}) = \int_{t=0}^{\infty} t^1\, c(\mathbf{x},t)\, dt$	first temporal moments
$m_2^c(\mathbf{x}) = \int_{t=0}^{\infty} \left(t - \bar{t}(\mathbf{x})\right)^2\, c(\mathbf{x},t)\, dt$	Second central temporal moment
$\bar{t}(\mathbf{x}) = \frac{m_1(\mathbf{x})}{m_0(\mathbf{x})}$	Breakthrough time

Stochastic theory aims to predict the spatial or temporal moments of a solute plume in a heterogeneous aquifer from the statistical moments of the underlying log-conductivity field. Since only statistical information on the conductivity field is used, obviously, we can derive only statistical information about the moments of the ensemble-averaged concentration, the ensemble average of the concentration moments in single realizations, and the related uncertainty.

We can use the spatial and temporal moments derived by stochastic theory for solute transport in heterogeneous domains to define macroscopic, or upscaled parameters. The macrodispersion tensor, e.g., is the dispersion tensor needed in calculations with uniform coefficients to meet the same second-central moments as the ensemble-averaged concentration in a heterogeneous domain.

2.7. Dispersion Theories

2.7.1. Taylor-Aris Dispersion

Taylor [1953,1954] was the first to analyze the relationship between the longitudinal dispersion coefficient for transport of a solute averaged over a cross section of a capillary tube and the molecular diffusion coefficient. In any type of shear flow, where the magnitude of the velocity varies normal to its orientation, the asymptotic longitudinal macrodispersion coefficient is proportional to the mean velocity squared and inversely proportional to the transverse diffusion coefficient [*Taylor 1953, 1954*]. Assume that at t =0, a tracer is introduced at x = 0 by a pulse. The transport of the solute takes place by advection with the velocity ν and by molecular diffusion, such that C(x,y,z,t) satisfies the following equation:

$$\frac{\partial C}{\partial t} + \nu(r)\frac{\partial C}{\partial r} = D_m \nabla^2 C \qquad (2.\ 21)$$

Taylor has shown that for a sufficiently long travel distance L or travel time t, the concentration C(x, t) averaged over the cross-section satisfies the advective-dispersion equation with uniform coefficients

$$\frac{\partial C}{\partial t} + \bar{\nu}\frac{\partial C}{\partial x} = (D_m + D_{TR})\frac{\partial^2 C}{\partial x^2} \qquad (2.\ 22)$$

$$\text{with } D_{TR} = \frac{a^2 \overline{\nu^2}}{48 D_m} \qquad \text{i.e. } D_{TR}/D_m = \frac{1}{48}Pe^2$$

where a is the radius of the tube, D_{TR} is the Taylor dispersion coefficient. Equation (2.22) is only valid if the travel time $t = L/\nu$ is much larger than the transverse diffusion time scale, i.e. it satisfies the inequality $tD_m/a^2 >> 1$. For large Peclet numbers, as encountered in most applications, it is seen that $D_{TR} >> D_m$.

The Taylor dispersion approach was rigorously extended by *Aris* [1956]. He analyzed the capillary dispersion problem by the evolution of axial moments of the concentration distribution, distinguishing between what *Brenner* [1980b] later called global and local moments. Global moments are obtained through integration of the concentration over the entire volume of the tube, whereas local moments are obtained through integration exclusively over the axial direction. It turns out that the temporal change of the *k* th global moment is the integral of an algebraic expression containing the (*k* -1)th local moment, which is governed by a partial differential equation (pde) depending on the (*k* -1)th global moment. The macrotransport parameters are then given by

$$v^* = \frac{1}{\mu}\frac{\partial \mu_1}{\partial t} \tag{2. 23}$$

$$D^* = \frac{1}{2\mu_0}\frac{\partial \mu_2^c}{\partial t} \tag{2. 24}$$

in which v^* and D^* are the macroscopic velocity and dispersion coefficient, m_2^c is the second central moment. Equation (2.24) has been used to infer the molecular diffusion coefficient from the axial dispersion in a capillary [*Bello et al., 1994*, *Belongia and Baygents, 1997*]. The theory has also been applied to the diffusion of particles in Couette flow [*Nadim, 1988*], and macrodispersion in stratified aquifers [*Gelhar et al., 1979*], among others. *Cirpka and Kitanidis* [2001b] analyzed the same type of macrodispersion for a helical device by the method of spatial moments.

2.7.2. Classical Macrodispersion

The most common macroscopic transport equation is formally identical to the local-scale advection-dispersion equation:

$$\frac{\partial \mathrm{c}}{\partial \mathrm{t}} + \mathrm{v}^* \cdot \nabla \bar{\mathrm{c}} - \nabla \cdot \left(\mathbf{D}^* \nabla \mathrm{c} \right) = 0 \tag{2. 25}$$

in which $\bar{c}$ is an averaged concentration, v^* is the macroscopic velocity vector and $\mathbf{D}^*$ the macrodispersion tensor. Both macroscopic parameters may change in time. The typical criteria to determine the macroscopic parameters are the spatial moments of the averaged concentration, which has already been discussed in the previous section.

Kitanidis [1992] used volume averages based on a periodic representation of the velocity field. The approach was generalized to stationary random media by *Wang and Kitanidis* [1999]. In the following, however, the most common methods of stochastic hydrology using ensemble-averages are briefly presented.

2.7.2.1 Eulerian Analysis

The stochastic theory developed by *Gelhar and Axness* [1983] provides a specific predictive model of large-scale dispersion indicating that a classical Fickian relationship is valid. In stationary log-conductivity fields, the longitudinal macrodispersivity is convectively controlled, but the transverse macrodispersivity is proportional to the local dispersivity and is several orders of magnitude smaller than the longitudinal term.

Gelhar & Axness [1983] analyzed macrodispersion in three-dimensional stationary velocity fields applying the same spectral methods as used for flow. Both the seepage velocity and the concentration are expressed by a deterministic trend and a random fluctuation:

$$\boldsymbol{v} = \bar{\boldsymbol{v}} + \boldsymbol{v}' = \frac{1}{\theta_e}\left(\bar{\boldsymbol{q}} + \boldsymbol{q}'\right) \tag{2. 26}$$

$$c = \bar{c} + c' \tag{2. 27}$$

Although in reality the local dispersion tensor **D** varies in space, it is assumed uniform in the following analysis. By introducing the perturbations into the transport equation, Eq. (2.16), and taking expected values we arrive at the transport equation of the mean concentration $\bar{c}$:

$$\frac{\partial \bar{c}}{\partial t} + \bar{v} \cdot \nabla \bar{c} + \nabla \cdot \left(\overline{v'c'}\right) - \nabla \cdot \left(\mathbf{D} \nabla c'\right) = 0 \tag{2. 28}$$

The comparison with Eq. (2.26) shows that the macroscopic velocity vector v^* is identical to the mean velocity $\bar{\boldsymbol{v}}$, whereas the macrodispersive flux consists of the local-dispersion contribution and the covariance of velocity and concentration fluctuations at zero separation:

$$\mathbf{D}^* \nabla c = \mathbf{D} \nabla \bar{c} - \overline{v'c'} \tag{2. 29}$$

Obviously, the macrodispersive parameterization is valid only when $\overline{v'c'}$ is proportional to $-\nabla \bar{c}$.

Subtracting the mean transport equation, Eq. (2.28), from the exact equation, Eq. (2.16), and neglecting second-order terms, yields the transport equation of the concentration fluctuations:

$$\frac{\partial c'}{\partial t} + v' \cdot \nabla \bar{c} + \bar{v} \cdot \nabla c' - \nabla \cdot \left(\mathbf{D} \nabla c'\right) = 0 \tag{2. 30}$$

Assuming a uniform mean concentration gradient $\nabla \bar{c}$ and a stationary velocity field, the concentration fluctuations are also stationary, and we can transfer Eq. (2.30) into the spectral domain [*Gelhar & Axness, 1983*]:

$$\frac{\partial \tilde{c}}{\partial t} + \tilde{v} \cdot \nabla \bar{c} + s \cdot \bar{v} \tilde{c} + s^T \mathbf{D} s \tilde{c} = 0 \tag{2. 31}$$

which holds for each wave number **s.** Eq. (2.31) is an ordinary differential equation of the Fourier transform of the concentration fluctuations. Applying zero fluctuations as initial condition, the solution of Eq. (2.31) is:

$$\tilde{c}(s,t) = \frac{1-\exp\left(-t\left(\mathrm{is}\cdot\bar{\mathbf{v}} + s^{\mathrm{T}}\mathbf{D}s\right)\right)}{\mathrm{is}\cdot\bar{\mathbf{v}} + s^{\mathrm{T}}\mathbf{D}s}\bar{\mathbf{v}}(s)\cdot\left(-\nabla\bar{c}\right) \tag{2. 32}$$

The cross-spectrum $S_{cv}(t,s)$ of concentration and velocity fluctuations is given by:

$$S_{cv}(t,s) = \tilde{c}(t,s)\tilde{\mathbf{v}}^{*}(s) = \frac{1-\exp\left(-t(\mathrm{is}\cdot\bar{\mathbf{v}} + s^{\mathrm{T}}\mathbf{D}s)\right)}{\mathrm{is}\cdot\bar{\mathbf{v}} + s^{\mathrm{T}}\mathrm{D}s}S_{vv}(s)(-\nabla\bar{c}) \tag{2. 33}$$

leading to the covariance of velocity and concentration fluctuations at zero separation $\overline{\mathbf{v}'c'}$:

$$\overline{\mathbf{v}'c'} = \frac{1}{(2\pi)^{d/2}}\int_{V_\infty} S_{cv}(t,s)ds = \frac{1}{(2\pi)^{d/2}}\int_{V_\infty}\frac{1-\exp(-t(is\cdot\bar{\mathbf{v}} + s^{T}\mathbf{D}s))}{is\cdot\bar{\mathbf{v}} + s^{T}\mathbf{D}s}S_{vv}(s)(-\nabla\bar{c}) \tag{2. 34}$$

That is, $\overline{\mathbf{v}'c'}$ is indeed proportional to $(-\nabla\bar{c})$ and the time-dependent macrodispersion tensor $\mathbf{D}^{*}(t)$ is:

$$\mathbf{D}^{*}(t) = \mathbf{D} + \frac{1}{(2\pi)^{d/2}}\int_{V_\infty}\frac{1-\exp(-t(\mathrm{is}\cdot\bar{\mathbf{v}} + s^{\mathrm{T}}\mathbf{D}s))}{\mathrm{is}\cdot\bar{\mathbf{v}} + s^{\mathrm{T}}\mathbf{D}s}S_{vv}(s)ds \tag{2. 35}$$

Gelhar & Axness [1983] analyzed $\mathbf{D}^{*}(t)$ at the large-time limit $t\to\infty$ where $\mathbf{D}^{*}$ approaches an asymptotic value. Eq. (2.35) has been derived by Neuman et al. [1987] using an Eulerian-Lagrangian method and by *Dagan* [1988] using a Lagrangian method. Closed-form expressions of $\mathbf{D}^{*}(t)$ as those derived by *Gelhar & Axness* [1983] and *Dagan* [1984; 1988] are obtained by choosing a covariance model of the log-conductivity, deriving the velocity spectrum and substituting it into Eq. (2.35).

2.7.2.2 Lagrangian Analysis

The temporal behavior of transport coefficients in a medium with spatial fluctuations in the conductivities was investigated by *Dagan* [1984, 1988, 1991] using a Lagrangian approach. This analysis neglects the influence of pore-scale dispersion on the transport of the solute, that is, the dispersion occurring at scales smaller than those characterizing the spatial distribution of hydraulic conductivity is neglected. The inherent assumption is that dispersion caused by velocity differences between different flow paths is much more important for the total field-scale dispersion than small scale velocity variability and molecular diffusion within the fluid phase.

Let $\mathbf{u}(\tau)$ be the velocity the particle experiences at time t along its trajectory (*Lagrangian* velocity). Then its displacement is:

$$\mathbf{X}(t) = \int_0^t \mathbf{u}(\tau)d\tau \tag{2. 36}$$

In advective transport, the Lagrangian velocity $\mathbf{u}(\tau)$ and the Eulerian $\mathbf{v(x)}$ are related by

$$\frac{\mathrm{d}\mathbf{X}(t)}{\mathrm{d}t} = \mathbf{v}\left(\mathbf{X}(t)\right) \tag{2. 37}$$

Accounting for local dispersion, the Lagrangian velocity $\mathbf{u}(\tau)$ differs from the Eulerian $\mathbf{v}\left(\mathbf{X}(\tau)\right)$ by random fluctuations leading to local-dispersive contributions to the covariance of particle displacements of:

$$\frac{\overline{\mathrm{d}\mathbf{X}'_{\mathrm{d}}\mathbf{X}'^{\mathrm{T}}_{\mathrm{d}}}}{\mathrm{d}t} = 2\mathbf{D} \tag{2. 38}$$

The Lagrangian analysis of advective-dispersive transport is performed best in the spectral domain, leading to expressions that are identical to those of the Eulerian analysis [*Dagan, 1988*; *Fiori, 1996*; *Dagan & Fiori, 1997*; *Fiori & Dagan, 2000*].

For the strictly advective case, the macrodispersion tensor $\mathbf{D}^*$ can now be evaluated as [*Dagan, 1984*]:

$$\mathbf{D}^*(t) = \frac{1}{2}\frac{\mathrm{d}\overline{\mathbf{X}'\mathbf{X}'^{\mathrm{T}}}(t)}{\mathrm{d}t} = \frac{1}{2}\left(\int_0^t \mathbf{R}_{\mathbf{vv}}((t-\tau)\overline{\mathbf{v}})\mathrm{d}\tau + \int_0^t \mathbf{R}_{\mathbf{vv}}((\tau-t)\overline{\mathbf{v}})\mathrm{d}\tau\right) = \int_0^t \mathbf{R}_{\mathbf{vv}}(\overline{\mathbf{v}}\tau)\mathrm{d}\tau \tag{2. 39}$$

Eq. (2.39) shows that, in stationary velocity fields, $\mathbf{D}^*(\mathrm{t})$ approaches an asymptotic value at the large-time limit. For non-reactive transport, *Fiori* [1996] extended the framework of *Dagan* [1989] to include pore-scale dispersion. He concluded that pore-scale dispersion influences macrodispersion primarily through its transverse component. Hence, neglecting pore-scale dispersion effects on macrodispersion implies neglecting the transverse mixing between different paths. *Dagan and Fiori* [1997] showed the effect of transverse pore-scale dispersion in heterogeneous porous media. Transverse pore-scale dispersion retards the quickly advancing fingers of solute and accelerates the slow ones. Indeed, advancing pore-scale dispersion transfers solute across the interface into zones of lower conductivity and vice versa.

2.7.3. Effective Dispersion

The behavior of the plume evolving from a point-like instantaneous injection is characterized by the velocity of its center of mass and by its dispersion as a function of time. *Dentz et al*. [2000*a*, 2000*b*] derived moment equations for a conservative solute in a heterogeneous flow field. They also made a clear distinction between the ensemble and the effective dispersion tensors. In both cases, they consider an average of half the rate of change of the second central moments. In case of ensemble dispersion, the classical macrodispersion, the

ensemble-averaging of the concentration is performed prior to taking the spatial moments. In effective dispersion, by contrast, the spatial moments are taken prior to ensemble averaging.

$$D_{ij}^{e} = \frac{1}{2}\frac{1}{\mu_0}\frac{\partial E\left[\mu_{ij}(c)\right]}{\partial t} \tag{2. 40}$$

The effective dispersion tensor describes therefore more accurately how small plumes spread, whereas the ensemble dispersion tensor includes information about the uncertainty. At the limit of a point-like injection, the dispersion theories based on strictly advective transport predict zero effective dispersion [*Dagan, 1990*]. Accounting for local dispersion, the effective dispersion tensor is initially identical to the local dispersion tensor, grows over time since local transverse dispersion makes the plume sampling increasingly more streamlines, and finally reaches the asymptotic macrodispersion tensor, although at very large times [*Attinger et al., 1999; Dentz et al., 2000a*].

In the Lagrangian framework, the effective dispersion coefficients are evaluated by the two particle moments of displacement: Conceptually, two particles are jointly introduced into each realization of the random field at locations ($\mathrm{X}(\mathrm{t}_0) = \mathrm{a}$ and $\mathrm{X}(\mathrm{t}_0) = \mathrm{b}$). For a point-like introduction, the initial separation **a** - **b** is zero. The displacement of the first particle is denoted by $\mathbf{X}(\mathrm{t})$, and that of the second by $\mathbf{Y}(\mathrm{t})$. Then, the covariance matrix of two-particle displacements $\overline{\mathbf{X}'\mathbf{Y}'}(t)$ is:

$$\overline{\mathbf{X}'\mathbf{Y}'}(t) = \mathrm{E}[(\mathbf{X}(t) + \mathrm{a} - \mathrm{E}[(\mathbf{X}(t)])(\mathbf{Y}(t) + \mathbf{b} - \mathrm{E}[(\mathbf{Y}(t)])^{\mathrm{T}}\,] \tag{2. 41}$$

in which $\mathrm{E}[(\mathbf{X}(\mathrm{t})] = \mathrm{E}[(\mathbf{Y}(\mathrm{t})]$ is the expected one-particle displacement.

At early times, the two-particle covariance of displacement with zero initial separation $\overline{\mathbf{X}'\mathbf{Y}'}(t; 0)$ is identical to the one-particle covariance of displacements $\overline{\mathbf{X}'\mathbf{X}'}(t)$. At later times, however, $\overline{\mathbf{X}'\mathbf{Y}'}$ increases much slower than $\overline{\mathbf{X}'\mathbf{X}'}$. Fiori & Dagan [2000] found, for three dimensional domains, that $\overline{\mathbf{X}'\mathbf{Y}'}$ becomes proportional to $\mathbf{ln}(\mathrm{t})$ at large times, while $\overline{\mathrm{X}'\mathbf{X}'}$ increases linearly. For a point-like injection, the effective dispersion tensor $\mathbf{D}^{\mathrm{e}}(\mathrm{t})$ is related to $\overline{\mathbf{X}'\mathbf{Y}'}(t; 0)$ by:

$$\mathbf{D}_{\mathrm{ij}}^{\mathrm{e}} = \mathbf{D}^{*} - \frac{1}{2}\frac{\overline{\partial \mathbf{X}'\mathbf{Y}'}(t;0)}{\partial t} \tag{2. 42}$$

The effective dispersion coefficients of an extended plume contain information on both the spreading and dilution of the plume. By contrast, the effective dispersion coefficients of a point-like injection may be used to describe solute dilution and dispersive mixing alone,

although $\mathbf{D}^e$ is not a direct measure of dilution. Figure 2.5 shows a plot of dispersion coefficients for conservative solute transport in periodic porous media under steady-state flow conditions. Time dependent longitudinal macrodispersion grows much faster and approaches the asymptotic value in the large-time limit whereas transverse macrodispersion increases, reaches its maximum value, decreases and reaches an asymptotic value that is slightly higher than the effective one in the large-time limit.

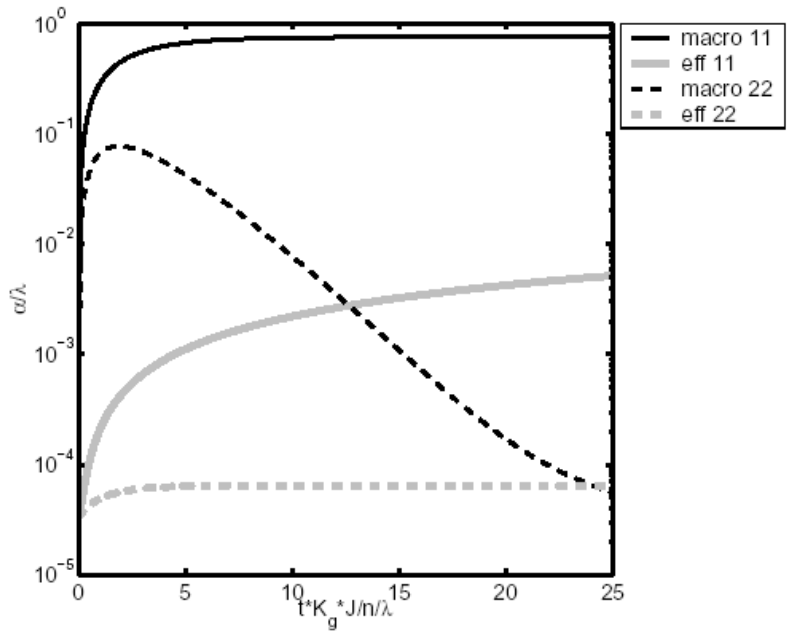

Figure 2.5 Longitudinal, transverse Macrodispersion and effective dispersion tensors for conservative solute transport in periodic porous media under steady-state flow conditions.

3. Materials and Methods

3.1. Introduction

I conduct experiments in three different dimensions (helical column, quasi two-dimensional laboratory scale and technical-scale model aquifers) to achieve the goal of the study. Here, I provide a detailed description of the materials, the design of the model aquifers, the filling procedures as well as the measurement techniques used in the study. Also, I describe the sedimentary structures formed in the heterogeneous model aquifers.

3.2. Materials

3.2.1. Tracers

The tracers used to conduct experiments can be classified as follows:

Conservative Tracer: I use Fluorescein and Cochineal Red 80 E 124 as conservative tracers. Fluorescein is selected as it is reported as a good conservative fluorescent tracer in silica sand (*Smart and Laidlaw*, 1977; *Kasnavia et al.,* 1999). The main advantage of fluorescein is its low detection limit of about 40$\mu g/l$. Fluorescein is dissolved in degassed-deionized water at a concentration of 500$\mu g/l$.

Cochineal Red 80 E 124 is selected as it is a red color food dye and thus is harmless to humans and the environment. It is also conservative, that is, it does not undergo degradation or absorption to the sand surface. 0.3 g/l concentration of the tracer is used for the tracer test.

Reactive Tracer: Some chemical compounds change color at different pH values, thus they can be used to indicate or approximately quantify pH values. The Table 3.1 lists common pH indicators.

Table 3.1 Common pH indicators

pH indicator	pH range	Color change	Concentration of solution
Thymol blue	1.2–2.8	red – yellow	0.1% in 20% Alcohol
Dimethyl yellow	2.9–4.0	red – yellow	0.1% in 90% Alcohol
Bromophenol Blue	3.0–4.6	yellow – blue	0.1% in 20% Alcohol
Congo red	3.0–5.0	blue – red	1% in water
Methyl orange	3.2–4.4	red –yellow	0.1% in water
Bromocresol green	3.8–5.4	yellow – blue	0.1% in 50% Alcohol
Methyl red	4.8–6.0	red – yellow	0.2% in 90% Alcohol
Litmus	5.0–8.0	red – blue	0.3% in 90% Alcohol
Bromocresol purple	5.2–6.8	yellow – purple red	0.04% in 90% Alcohol
Bromothymol blue	6.0–7.6	yellow – blue	0.1% in 20% Alcohol
Neutral red l	6.8–8.0	red – yellowish orange	0.1% in 70% Alcohol
Phenol red	6.6–8.0	yellow – red	0.02% in 90% Alcohol
o-Cresol red	7.0–8.8	yellow – purple red	0.1% in 20% alcohol
Tropaeoline 000	7.6–8.9	yellowish green – pink	1% in water
Phenolphthalein	8.2–10.0	colourless – pink	1.0% in 50% Alcohol
Thymol blue	8.0–9.6	yellow – blue	0.1% in 20% Alcohol
Thymolphthalein	9.4–10.6	colourless – blue	0.1% in 90% Alcohol
Alizarin Yellow R	10.1–12.0	yellow – red	0.1% in 50% Alcohol
Tropaeoline O	11.3–13.0	yellow – orange red	0.1% in water

In the experiments, two kinds of indicators are chosen: a mixture of Methyl red and Thymol blue and only Thymolblue. The chemical structures of both pH indicators are given in Figure 3.1. They both show a change from red to yellow color when changing from acidic to alkaline conditions. Thymol blue changes further to blue at high pH values. The physical and chemical data are listed in Table 3. 2.

Table 3. 2 Physical and chemical data for Methyl red and Thymolblue

	Methyl red	Thymol blue
Formula	$C_{15}H_{15}N_3O_2$	$C_{27}H_{30}O_5S$
Molar mass	269.31 g/mol	466.60 g/mol
Melting point	178°C-182°C	
Bulk density	300-500 kg/m^3	350 kg/m^3
Solubility in water (20°C)	Slightly soluble	Almost insoluble
Use as pH indicator	0.1 g in 100 ml ethanol (96%)	0.04g in 100 ml ethanol (20%)
pKa	4.5	8.8

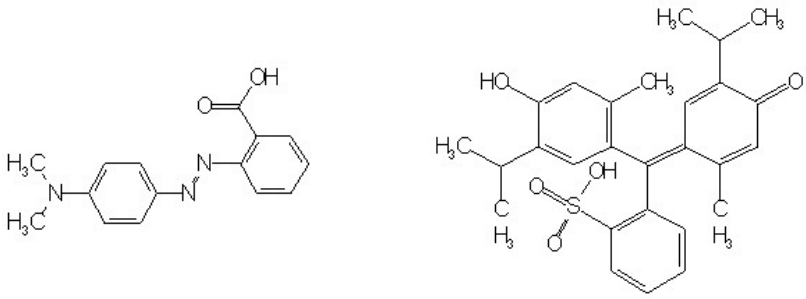

Figure 3.1 The structure formulas of Methyl red (left) and Thymol blue (right) (*Source: Merck chemical databases*)

3.2.2. Glass Beads and Sand Types

To fill the helical column, I use spherical, non-transparent glass beads with a grain size of 0.75 mm to 1 mm as filling materials. The glass beads were supplied by *SIGMUND LINDER*, Germany.

The two-dimensional model aquifers are filled homogeneously and heterogeneously with different silica sand mixtures. The basic criteria for the selection of sand types are-

- to ensure macroscopic scale heterogeneity (significant difference between the sand types) and small scale heterogeneity (sufficient variability within each sand type), and
- to prevent exhibiting a pH buffering capacity over the pH range applied in the experiments as the reactive tracer test is based on pH changes.

I use three sand types (grain size 1.0 - 2.5 mm, 0.0 – 3.0 mm, 0.1 – 0.8 mm) together with the mixture of two sand sizes (0.3 –0.6 mm and 0.6 – 1.2 mm). The grain size distribution graphs of each sand type are given in Figure 3. **2** to Figure 3.6. The mixture of two sands

is prepared by an electric mixer with a weight ratio of 1:1. Sands were provided by Dorfner GmbH (supplied by Paul Link GmbH, Korntal-Münchingen). Sand with grain size 1.0 mm to 2.5 mm is referred to as coarse sand (1.67×10^{-2} m/s), the sand with grain size 0.3 mm to 1.2 mm (mixture of two sand types) is referred to as mixed sand. The sand with a flat grain size distribution 0.0 mm to 3.0 mm is referred to as medium sand and the sand with grain size 0.1 mm to 0.8 mm is referred to as fine sand. The grain sizes and the hydraulic conductivity values of the sand types are shown in Table 3. 3.

Table 3. 3 Grain sizes and hydraulic conductivity of the chosen sand types

Name	Type	Grain size (mm)	Conductivity (m/s)
Coarse sand	Dorsilit Nr. 5	1.00-2.5	1.67×10^{-2}
Mixed sand	Dorsilit Nr. 7 and 8	0.3-0.6 and 0.6- 1.2	4.32×10^{-3}
Medium sand	Dorsilit Nr. 0-3	0.0 – 3.0	9.09×10^{-4}
Fine sand	Dorsilit Nr. 8/9	0.1-0.8	5.61×10^{-4}

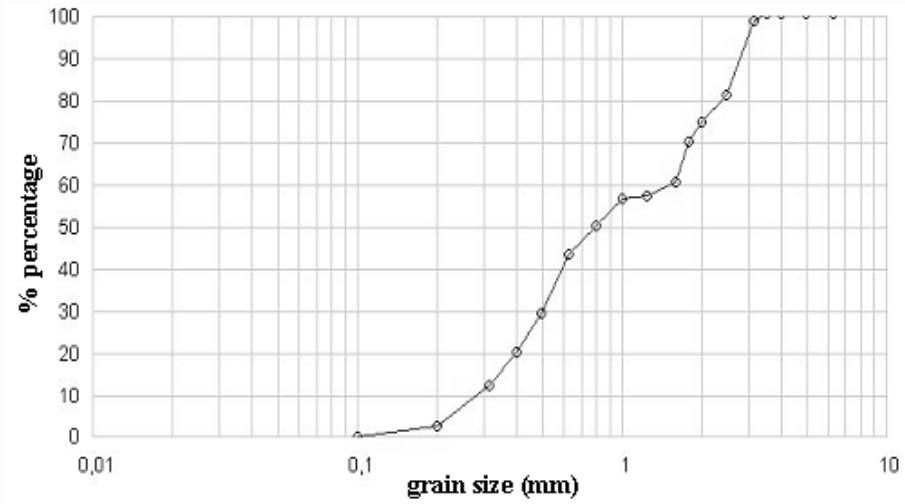

Figure 3. 2 Grain-size distribution of the quartz sand (Dorsilit Nr. 0-3)

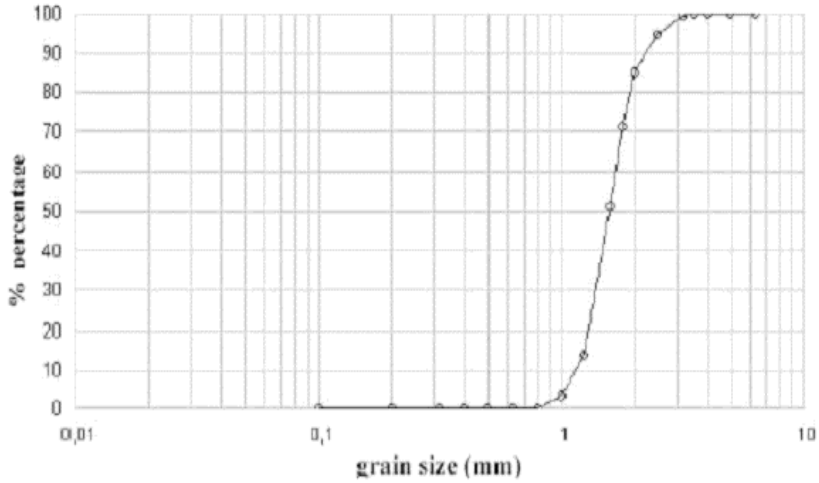

Figure 3. 3 Grain-size distribution of the quartz sand (Dorsilit Nr. 5)

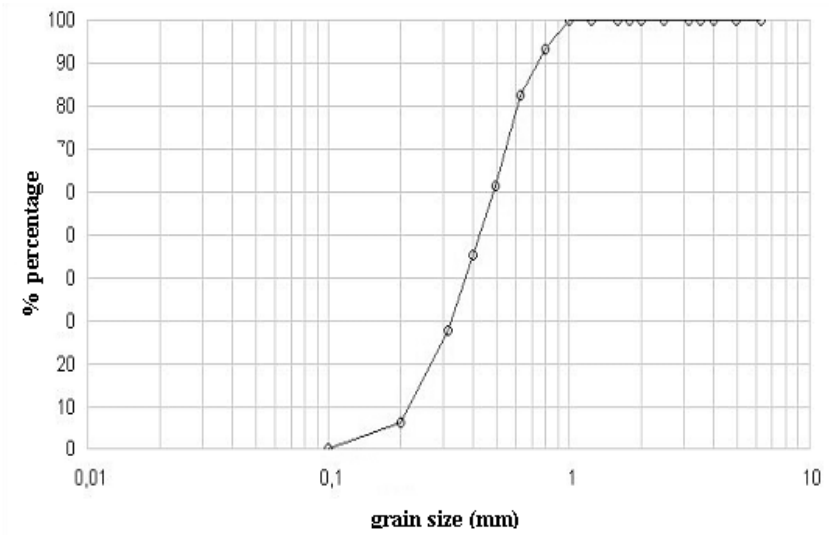

Figure 3.4 Grain-size distribution of the quartz sand (Dorsilit Nr. 8/9)

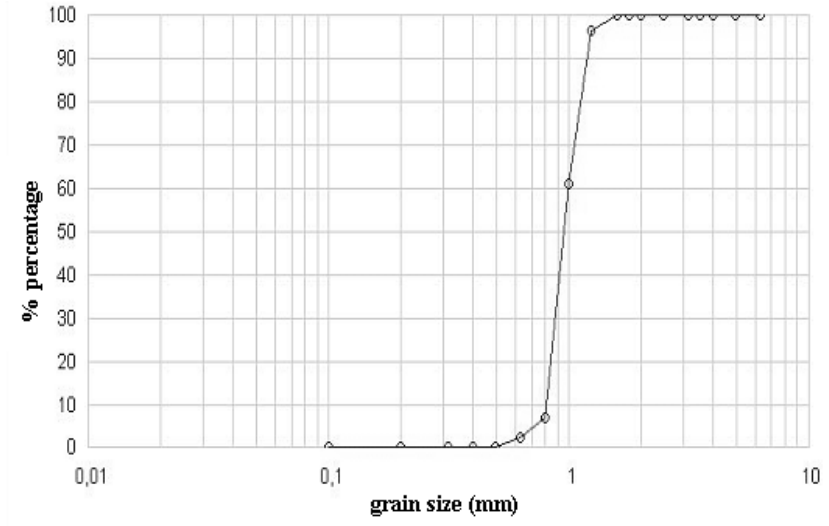

Figure 3.5 Grain-size distribution of the quartz sand (Dorsilit Nr. 7)

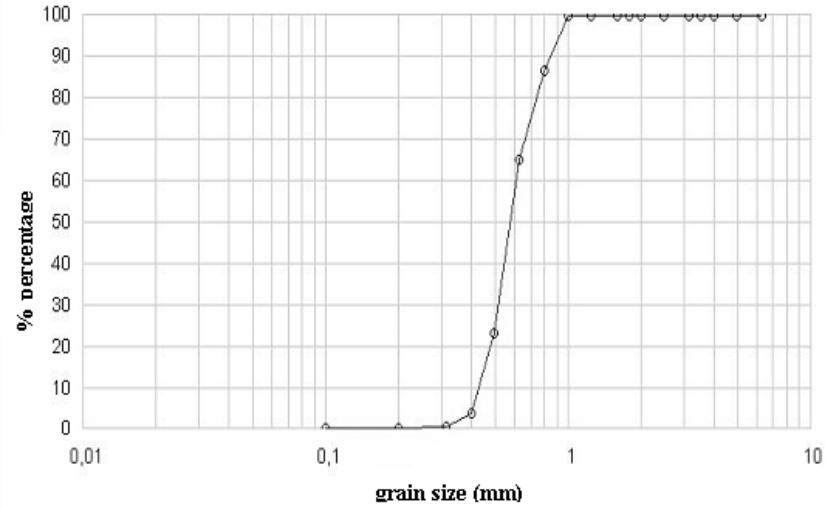

Figure 3.6 Grain-size distribution of the quartz sand (Dorsilit Nr. 8)

3.2.3. Camera

I use a digital camera Casio QV-5700 to take images during the course of the experiment. It is positioned on fixed stands, made of steel, placed in a distance of 1.6m from the windows of the sandbox.

3.2.4. Light Source:

I use neon-light tubes (LUMILUX L58W/860 PLUS, 58W/6000K, 1.5 m long and Ø26 mm), which have a very high color temperature, 6000K, similar to daylight. The tubes are placed in two rows over a total length of the sandbox (14.5 meters), illuminating the sandbox uniformly.

3.3. Design of the Column and Model Aquifers

I use one column and two sandboxes to perform experiments. Here, the one-dimensional column is refer to helical column and the 3m model one is referred to as laboratory-scale model aquifer and the 14m one is referred to as technical scale model aquifer. In the following subsections, I describe the design of the helical column and the model aquifers.

3.3.1. Helical Column

The helix is a stainless steel, 1.7 m long column, which looks like a normal straight column from the exterior (Figure 3.7), but in the interior it is a helix (Figure 3. 8). It has 60 rotations. The outer diameter of the helix is 10 cm with a core diameter of 3 cm, and a pitch of 27 mm. The thickness of the flights is 2 mm, so that the effective thickness of the packing is 25 mm.

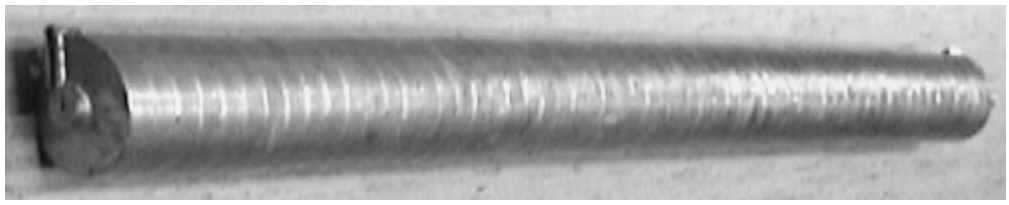

Figure 3.7 Exterior view of the helical column

The inlet of the helix has the dimension of 2cm x 2.5 cm x 3.5cm. Stainless-steel wire fabric (mesh size <0.7 mm) are placed to keep the porous material out of the inlet chamber. The inlet has four connections: one to inject water, one for the tracer solution, one to drain the chamber and the fourth one for the piezometer. This allows me to flush the chamber with the tracer solution in order to achieve a uniform concentration in the inlet. A fiber optic probe is directly connected to the inlet chamber.

Like the inlet, the outlet of the helix has the dimension of 2cm x 2.5 cm x 3.5cm. Wire fabrics are used in the same manner as in the inlet to keep the porous material out of the outlet. A fiber optic probe is connected to the outlet tube by a flow-through cell. Details drawing of the inlet and outlet of the column are given in the appendix B.

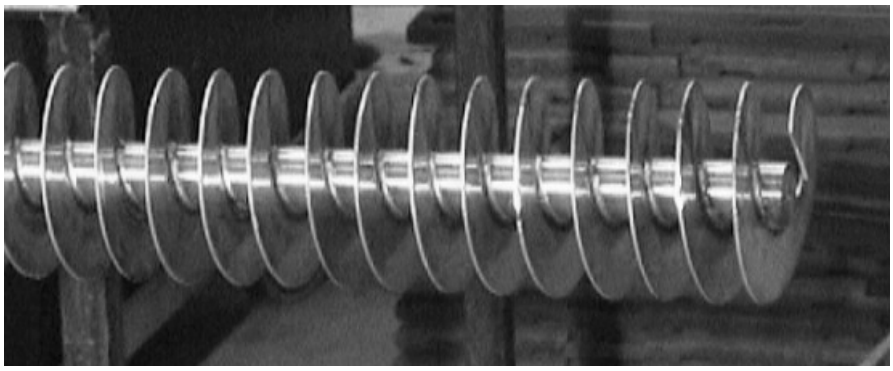

Figure 3. 8 Interior of the helical column

3.3.2. Laboratory Scale Model Aquifer

It is made of standard steel and has the dimension of 3.4m x 0.50m x .15m (Figure 3.9). The front side has a 15mm thick glass pane facilitating visual observation of the tracer movement through the heterogeneous medium during the course of the experiments. The top of the box is covered by a steel frame.

Figure 3.9 A general view of the laboratory scale model aquifer

The inlet of the small sandbox is provided with a 5 cm long inlet chamber. A stainless-steel wire fabric (mesh size < 0.1mm) is used at the side facing the packed sandbox to keep the sand out of the inlet chamber. The wire fabric is fixed to a perforated stainless-steel plate. A horizontal injection well (a perforated pipe covered with fine mesh) with a diameter of 2cm is inserted through the rear of the box penetrating through the full 0.15m thickness of the box. Twenty-two piezometric tubes are connected to the box to obtain the pressure head. Four piezometers each are connected at every 75 cm length of the sandbox. The distance between the piezometers at each cross-section is 5 cm. Like the inlet, the outlet of the box is also provided with a 5 cm long outlet chamber. Perforated steel sheets and wire fabrics are used in the same fashion as in the inlet to keep the sand out of the outlet chambers.

3.3.3. Technical Scale Model Aquifer

It is made of standard steel and has dimensions of 14m x 0.5m x 0.13m (Figure 3. 10). At the front side, windows with 15mm thick glass panes provide the opportunity of visual observations. The top of the box is covered by a PVC sheet. Detailed drawings are given in the appendix A.

Figure 3. 10 A general view of the technical scale model aquifer

5cm long chambers are added at both the inlet and the outlet. Vertically, the inlet is divided into two sub-chambers with an equal height of 25cm by a stainless steel plate reaching into the sand filling as a flow separator. This provided the possibility to inject tracer solutions separately into the upper or lower half of the domain.

The domain is 14 m long, and 126 fiber optic probes together with 100 piezometric tubes are connected to it. The probes are connected in two sets alternatively at equal distance, one with ten probes and the other with nineteen probes. The series repeat themselves at a distance of 2.8 m. The connectors for the fiber optic probes are standard cable inlets with PG thread (inner diameter 9 mm). The measurement tip of the fiber optic probes is inserted 4 cm into the packed sandbox. This feature is for experiments on longitudinal dispersion that are not discussed here. Hundred piezometers are connected to the domain to measure the pressure head over the domain. Ten piezometers each are connected at every 140 cm length of the sandbox. The distance between the piezometers at each cross-section is 4.8 cm. The locations of probes and piezometers are shown in Figure 3. 11, as cross and circles, respectively.

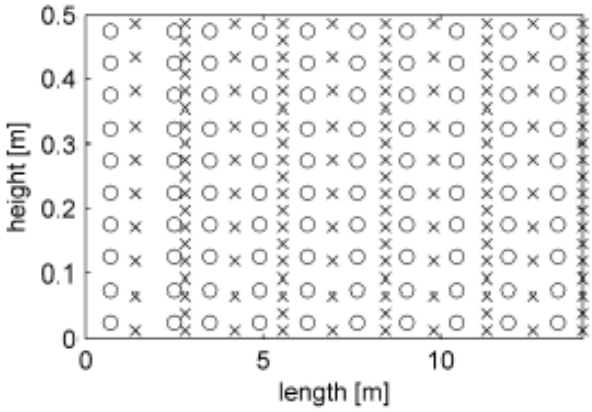

Figure 3. 11 Position of the piezometers and the probes in the domain of the sandbox

The outlet chamber is divided into nineteen sub-chambers of equal height. Perforated steel sheets and wire fabrics are placed in the same fashion as in the inlet to prevent sand falling into the chambers. Fiber optic probes are connected to the outlet tubes by flow through cells, whereas piezometers are directly connected to the outlet flow chambers.

The outflow tubes are connected to a hydraulic switchboard. The purpose of the board is to measure the discharge of the nineteen flow chambers separately. The switchboard consists of two vertical flow chambers, each connected to a constant-head tank, and nineteen horizontal tubes. Each of the nineteen horizontal flow tubes is connected to the two vertical flow chambers and one outflow chamber of the sandbox via a three-way-valve. By connecting a single outflow chamber to one constant-head tank while connecting all other outflow chambers to the other constant-head tank, the discharge of this single chamber can be measured.

3.4. Filling Procedures

I fill the small sandbox in two ways, first, with homogeneous silica sand and second with two distinct sand mixtures that create microscopic heterogeneity and the large sandbox with four sand mixtures to produce macroscopic heterogeneity.

3.4.1. Homogeneous Filling of the Helical Column

There are several methods for homogeneous filling and packing in standard sandboxes and columns [see, e.g., *Ripple et al., 1973*, 1974; and *Oliviera et al., 1996*]. Because of the helical geometry, only dry packing could be applied. In order to achieve uniform packing, the column is filled from top to bottom by a funnel with a tube. The column was attached vertically (inlet at the topside) on the top of a rotating plate. Then it was inclined axially at 35° from the vertical plane. A funnel with a tube was added to the inlet of the column (Figure

3.12). The glass beads were poured into the column for a minute. A hydraulic vibrator was attached to the plate of the rotator to support homogeneous compaction of the filling. After each session of pouring glass beads, the column was rotated for 4 minutes. Finally, the column was laid down horizontally and the inlet chamber of the column was filled and closed. The resulting column porosity was 40%.

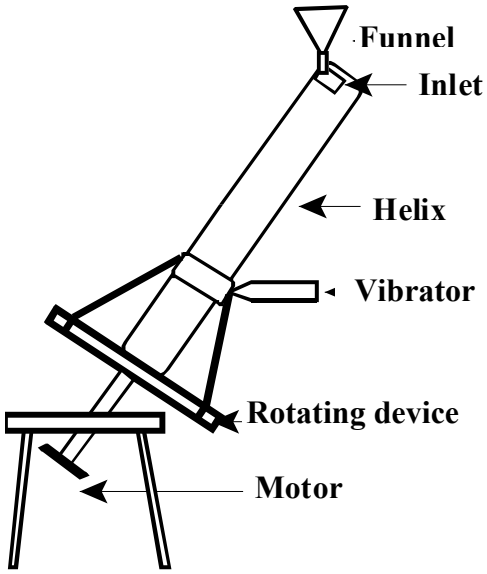

Figure 3.12 Filling setup of the helical column

3.4.2. Homogeneous Filling of the Model Aquifer

For the filling of the model aquifer, first the sand was moistured in a black plastic container to make it slightly cohesive, preventing the fine particles in the sand to be separated during the filling procedure and form an undesired layer of fines into the domain. The sand was transferred by buckets and homogeneously filled into the sandbox. After reaching about 9 cm thickness, the sand layer was packed by a wood block, and the first layer of sampling needles was set up. Sand was carefully added until it submerged the needles. This procedure was repeated for every layer of sampling needles. When the sandbox was full, the steel plate was placed on the top of the sandbox and fixed. In order to simplify the packing procedure, it was decided to do the experiment in an unconfined aquifer, which means the inlet water level is about 2 cm lower than the top of the sandbox.

3.4.3. Filling Exhibiting Micro-Scale Heterogeneity

I use two sand types - fine sand (0.1 mm to 0.8 mm) and Medium sand (0.0 mm to 3.0 mm) for two different fillings with microscopic heterogeneity. Sand was poured into a stagnant water body at relatively higher rates producing naturally looking sedimentary structures. The turbulent flow conditions during the filling produce the micro-scale structures. In

order to achieve the desired structure, canisters were filled with the desired sand type and hung from the crane (Figure 3. 13). After filling the box with sand, the water was drained. To prevent preferential flow at the top of the domain, which could occur due to compaction of the sand filling, I added a 5 cm thick layer of toptogel. Swelling of the toptogel ensured the compaction of the sand while sealing efficiently the top of the domain.

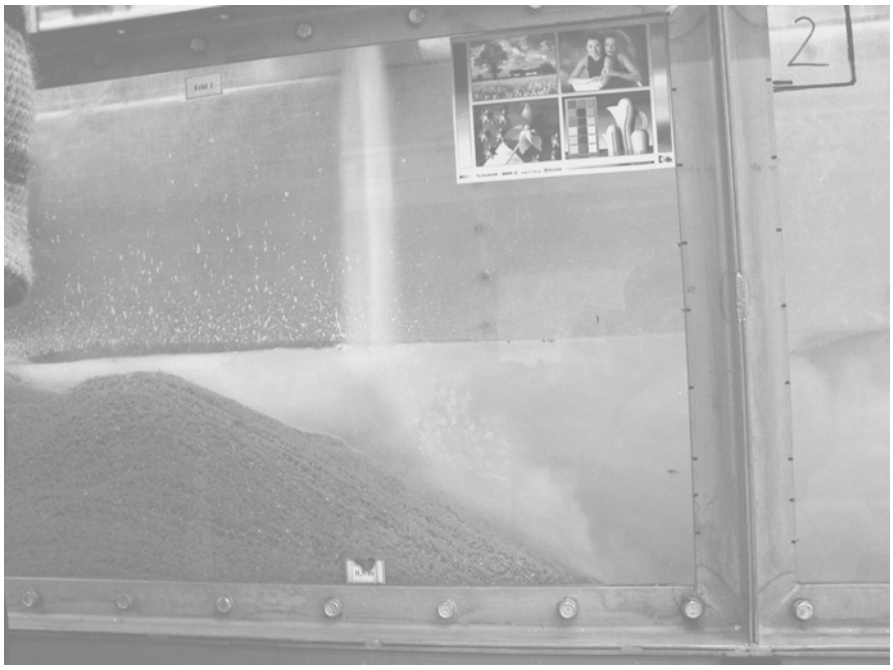

Figure 3. 13 Filling procedure used in the sandbox

3.4.4. Filling Exhibiting Macroscopic Heterogeneity

Definite rectangular heterogeneities of uniform sand structures are advantageous for modeling purposes, but they do not reflect the type of heterogeneity observed in sedimentary deposits such as lamination, graded bedding (coarsening or fining upwards) or cross bedding. Thus, sacrificing the definiteness of the structure, I tried to mimic at least partially the sedimentary process itself, creating more realistic structures. Additional constraints were:

- to prevent a continuous layer of high permeability dominating the entire flow field,
- to create structures that can be determined on the planned grid of measurement points,
- to include a sufficiently high number of layers to guarantee representative flow behavior.

The heterogeneous artificial aquifer is filled by using the similar filling procedure as in the laboratory scale model aquifer, i.e., by releasing different types of sand mixtures at relatively high rates into a stagnant water body within the model domain. Prior to the filling, a qualitative sketch was drawn onto the glass wall of the domain, indicating the distribution of

sand types. The typical length of each lenses is 2m and its typical height is 0.10m. After filling the box with sand, the water was drained from it.

Crushed, dried clay was distributed uniformly on the top of the sand layers to prevent preferential flow at the top of the domain that could occur due to compaction of the sand filling. After the completion of the filling procedures, the qualitative sketch was erased from the glass wall.

Figure 3. 14 shows the distribution of the four sand types, mimicking a facies distribution.

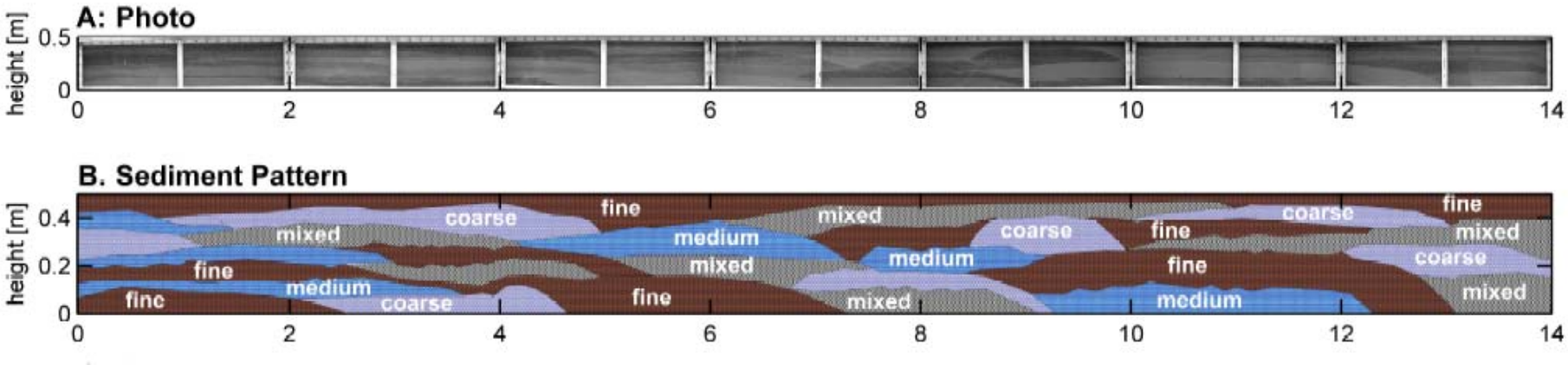

Figure 3. 14 Distribution of sand types in the sandbox.

3.5. Sedimentary Structures Observed in the Model Aquifers

Sedimentary structures like different types of lamination and ripples were produced in the model aquifer. These are very typical sedimentary structures in nature.

a. *Parallel Lamination:*

Parallel lamination was formed in fine sand layers, mostly at the lower layers of the technical scale model aquifer and throughout the laboratory scale model aquifer (Figure 3. 15) and (Figure 3. 16). The lamina has a typical thickness of 2-3 mm.

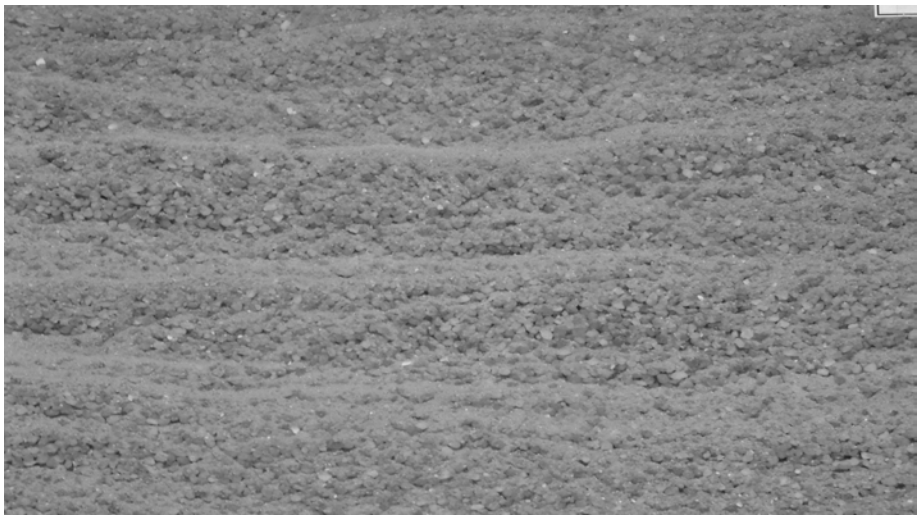

Figure 3. 15 Sedimentary structure (lamination) formed in the laboratory- scale model aquifer

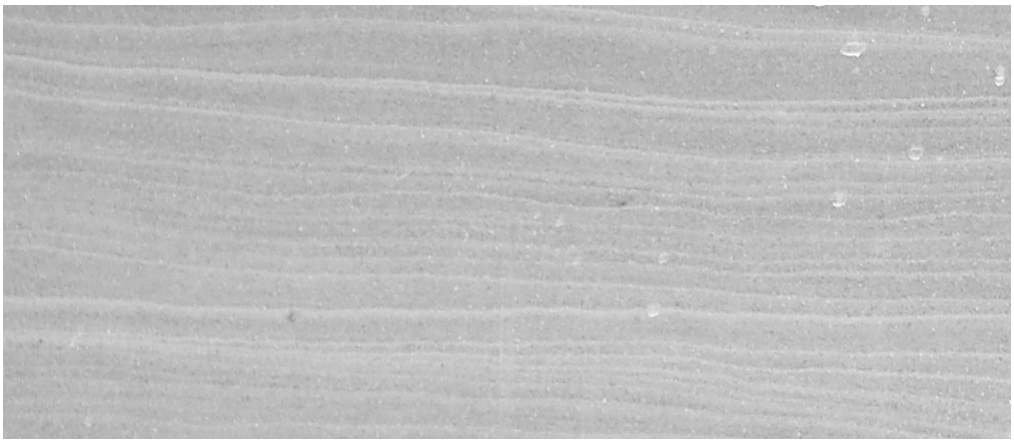

Figure 3. 16 Sedimentary structure (lamination) formed in the laboratory-scale model aquifer

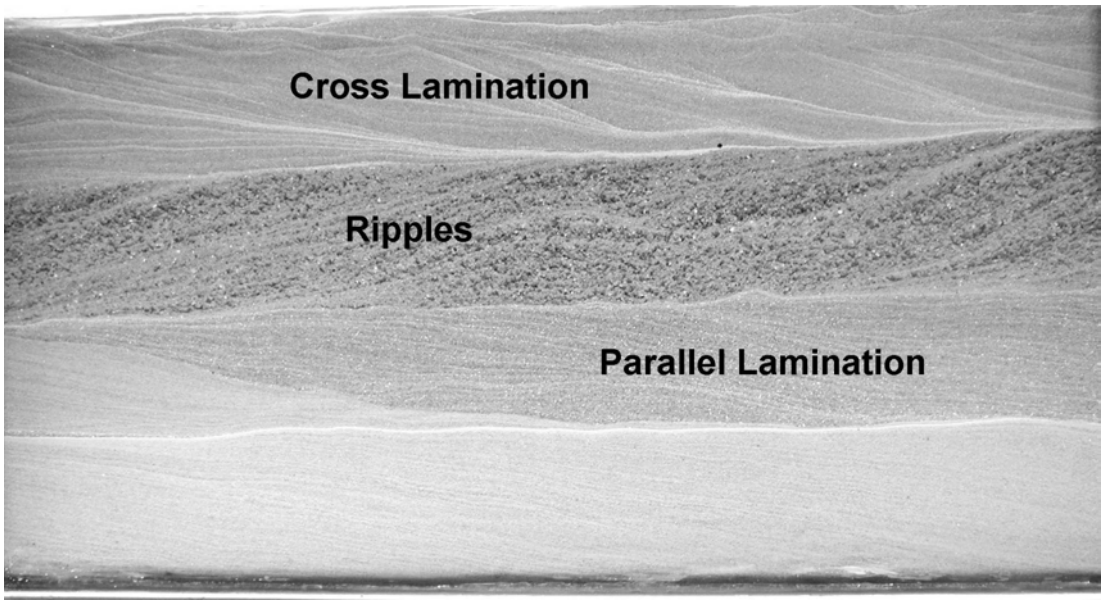

Figure 3. 17 Sedimentary Structures observed in the technical-scale model aquifer

b. *Cross Lamination:*

Cross laminations was formed at the upper fine, mixed and medium sand lenses (Figure 3. 17). Here, the individual layers are inclined and have a thickness of less than 1 cm.

c. *Ripples:*

Ripple marks or structures of similar shape, were produced in the medium sand lenses (Figure 3. 17).

3.6. Concentration Measurement

I use a point measurement technique modified by *Jose* [2004] and I develop an innovative noninvasive imaging technique for quantifying transverse dispersive mixing in porous media.

3.6.1. Point Measurement Techniques

I use fiber-optic fluorimetry for the in-situ measurements of fluorescent tracer concentration at the inlet and outlet of the helix. The major elements in fiber- optic fluorimetry are the fluorometers, optic fiber probes and the data acquisition system. The data is acquired and stored in a PC using a software provided by the manufacturer of the fluorometers. The final diameter of the modified measurement tip is 2.5 mm (Figure 3. 18). Details of the point measurement system used in the experiments are presented by *Jos*e, [2004].

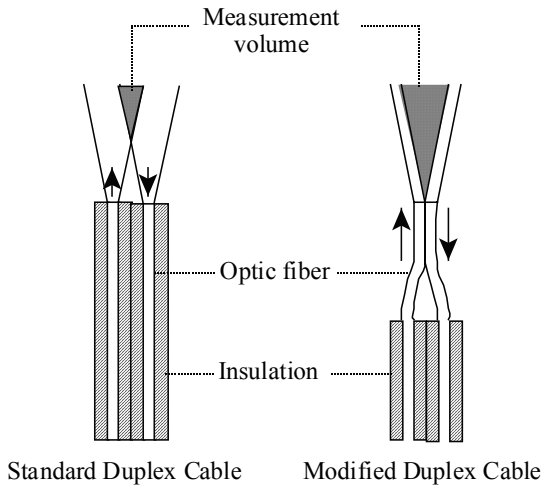

Figure 3. 18 Point Measurement Techniques by Fiber Optic Fluorometry

3.6.2. Imaging Techniques

An imaging technique is developed for the visualization of transverse mixing in a quasi two-dimensional domain and to quantify the effect of macroscopic and microscopic heterogeneity on transverse dispersive mixing. I use a tracer dye in the experiments. Thus I can determine the concentration distribution by taking and processing digital images of the glass front during the course of the experiment. In order to quantify the tracer concentration, I need two additional images of the sandbox, one for the case that the entire box is filled uniformly with the tracer solution, and another for uniform, tracer-free conditions. The images are recorded by a Casio digital camera, and stored on a computer. The images are analyzed by a script written in MATLAB.

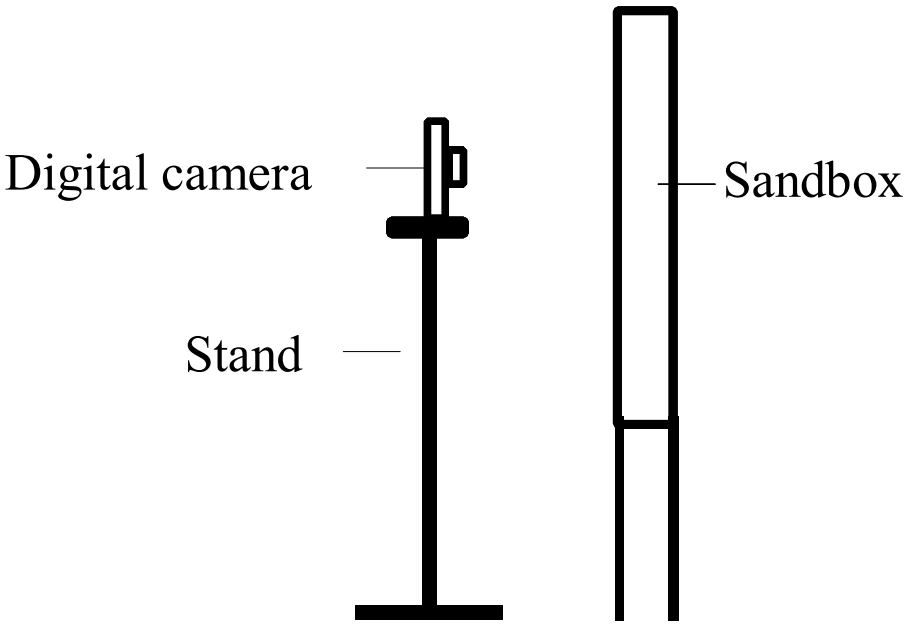

Figure 3. 19 An Imaging Technique used in the experiments

The digital camera is positioned in a distance of 1.6m from the sandbox windows. For all the windows, the camera was set up in exactly the same position and same height (Figure 3. 19). To ensure reproducibility, fixed stands made by steel on the ground (with a tolerance of less than 1 mm) were used, and photos were taken for all windows under identical conditions: (1) For each window, the distance and position of the camera were the same. (2) Only the neon light was used as an illumination source, which required that all the photos were taken at night. (3) The camera parameters (shutter speed 1/30 s, aperture F2.0, focus to the middle point of the objective, WRE i.e. white remediation for indoor situation,) were set manually to identical values. Table 3. 4 summarizes the parameter used for photography.

Table 3. 4 Parameter set in Digital Camera

Parameters	**Settings**
Sutter Speed	1/30
Aperture	F2.0
Focus	Mid point of the object
White balance	WRE i.e. white remediation for indoor situation

In order to avoid the vibration of the camera, which would cause shifting or rotation of the pictures, a remotely control computer program is used. Color cards are stuck on each window to give an ideal color as reference. A big rectangular frame holding a dark color curtain is placed behind the camera to prevent any reflection of other objects.

4. Determination of Pore scale Transverse Dispersivity in a Helical Soil Column

4.1. Introduction

In this chapter, I develop an experimental method for the determination of pore-scale transverse dispersivity by Taylor-Aris dispersion theory as suggested by *Cirpka and Kitanidis* [2001b]. While their study was theoretical, I present experimental results.

In Taylor-Aris dispersion, the longitudinal macrodispersion coefficient is inversely proportional to the pore-scale transverse dispersion coefficient. *Cirpka and Kitanidis* [2001b], proposed to induce shear flow, needed for Taylor-Aris dispersion, by using a helical geometry of the flow domain. Since the circumference of the helix is larger at the outside than that of the inside, the angular flow velocities are higher at the inside of the helix than at the outside. They presented analytical expressions for angular macrodispersion in a helical domain provided that the pitch of the helix is negligible.

4.2. Systems of Helical Coordinates

Consider a helical domain as shown in (Figure 4.1). The domain is characterized by the inner and outer radius r_1 and r_2, the pitch Δz and the number of convolutions n. For the purposes of our analysis, we may use cylindrical coordinates. However, in the helix, a second coordinate system can be defined. In this helical coordinate system the z and *r* directions are the same as in the cylindrical one. The difference between the two systems of coordinates is in the angular coordinate. In the helical coordinate system the angular coordinate follows the convolution of the helix and therefore is not perpendicular to the *z-r* plane.

A side effect of the system of helical coordinates, is that z ranges only from 0 to Δz. The mapping from helical to Cartesian coordinates is:

$$\begin{aligned} x_1 &= r\cos(\varphi) \\ x_2 &= r\sin(\varphi) \\ x_3 &= \frac{\Delta z \varphi}{2\pi} + z \end{aligned} \qquad (4.1)$$

in which x_1 and x_2 are horizontal and x_3 vertical Cartesian coordinates, *r* and *z* are the radial and vertical coordinates within the cross-section between two flights, and φ is the angular coordinate parallel to the flight.

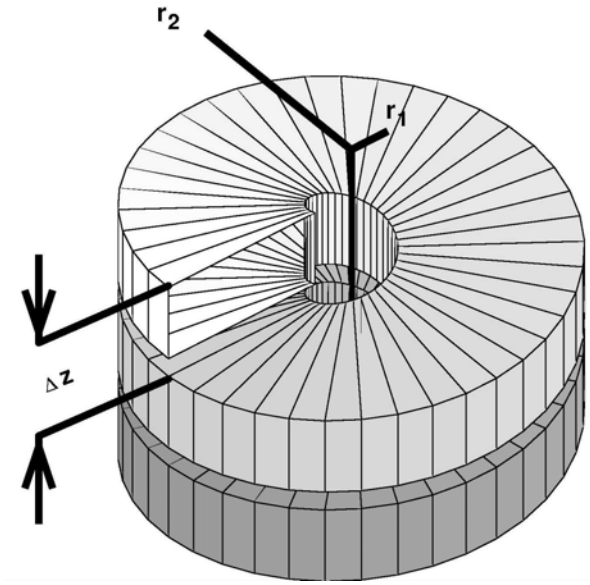

Figure 4.1 Visualization of the Helical Column

4.3. Limiting Case of Negligible Pitch

4.3.1. Governing Equation

Cirpka and Kitanidis [2001b] analyzed flow and transport in helical porous media for the limiting case of $\Delta z \to 0$. Under these conditions, there is no variation in the vertical direction, and the flow and transport equations can be formulated in two dimensions. The flow equation is:

$$\frac{K}{r^2}\frac{\partial^2 h}{\partial \varphi^2} + K\frac{\partial^2 h}{\partial r^2} + \frac{K}{r}\frac{\partial h}{\partial r} = 0 \tag{4. 2}$$

where h is the hydraulic head, K is the hydraulic conductivity, r is the radial, and φ the angular coordinate.

The specific discharge is always oriented into the angular direction:

$$q_\varphi = \frac{KJ}{r} \tag{4. 3}$$

where J is the negative angular head gradient.

The corresponding transport equation for a negligible pitch $\Delta z \to 0$ is:

$$\frac{\partial c}{\partial t} + \frac{q_\varphi}{r\theta}\frac{\partial c}{\partial \varphi} - \frac{D_l}{r^2}\frac{\partial^2 c}{\partial \varphi^2} - \frac{\partial}{\partial r}\left(D_t\frac{\partial c}{\partial r}\right) - \frac{D_t}{r}\frac{\partial c}{\partial r} = 0 \tag{4. 4}$$

subject to the boundary conditions:

$$\left.\frac{\partial c}{\partial r}\right|_{r=r_1,r_2} = 0 \tag{4. 5}$$

$$c(\varphi=0) = \delta(t) \tag{4. 6}$$

where c is the concentration in the aqueous phase, θ is the effective porosity, t is time and D_l and D_t are the longitudinal (tangential) and transverse (radial) dispersion coefficients, respectively [*Scheidegger, 1961*]:

$$D_l = \alpha_l \frac{|\mathbf{q}|}{\theta} + D \tag{4. 7}$$

$$D_t = \alpha_t \frac{|\mathbf{q}|}{\theta} + D \tag{4. 8}$$

in which α_l and α_t are the longitudinal and transverse dispersivities, which are properties of the porous medium, and D is the effective diffusion coefficient, which may differ from the molecular one by a factor referred to as tortuosity. At the large-distance limit we impose the auxiliary condition:

$$\lim_{\varphi\to+\infty} \frac{\partial^n c(\varphi,r,t)}{\partial\varphi^n} = 0 \quad \forall n \geq 0 \tag{4. 9}$$

4.3.2. Temporal Moments for the Case with Negligible Pitch

The k-th temporal moment of the flux-weighted concentration is defined as:

$$M_k(\varphi) = \frac{1}{Q_{tot}} \int_{r_1}^{r_2} q_\varphi(r) \int_0^\infty t^k c(t,r,\varphi) dt dr \tag{4. 10}$$

with:

$$Q_{tot} = \int_{r_1}^{r_2} q_\varphi(r) dr (\Delta z - z_f) = KJ \ln\left(\frac{r_2}{r_1}\right)(\Delta z - z_f) \tag{4. 11}$$

which is the total discharge and $(\Delta z\text{-}z_f)$ is the height of the cross-section. For the second and higher moments we also define central moments $M_{kc}(\varphi)$:

$$M_{kc}(\varphi) = \frac{1}{Q_{tot}} \int_{r_1}^{r_2} q\varphi(r) \int_0^\infty \left(t - \frac{M_1}{M_2}\right)^k c(t,r,\varphi) dt dr \tag{4. 12}$$

In analogy to transport in parallel flow, we expect that the flux-weighted cross-sectional average of the concentration satisfy, after a relaxation time, a macroscopic advection-dispersion equation:

$$\frac{\partial \breve{c}}{\partial t} + \omega_{mac} \frac{\partial \breve{c}}{\partial \varphi} - D^{\varphi}_{mac} \frac{\partial^2 \breve{c}}{\partial \varphi^2} = 0 \tag{4. 13}$$

with the flux-weighted concentration $\breve{c}$:

$$\breve{c}(\varphi, t) = \frac{1}{\ln\left(\frac{r_2}{r_1}\right)} \int_{r_1}^{r_2} \frac{c(r, \varphi, t)}{r} dr \tag{4. 14}$$

ω_{mac} and D^{φ}_{mac} are the macroscopic rotational seepage velocity and dispersion coefficient, respectively. These macroscopic parameters can be expressed in terms of the dimensions r_1 and r_2 of the helix, the total specific discharge Q_{tot}, the porosity θ, and the parameters determining pore-scale dispersion α_l, α_t, and D. We relate the angular derivatives of the global moments to the macroscopic parameters ω_{mac} and D^{φ}_{mac} by:

$$\frac{\partial M_0}{\partial \varphi} = 0 \tag{4. 15}$$

$$\frac{\partial M_1}{\partial \varphi} = \frac{M_0}{\omega} \tag{4. 16}$$

$$\frac{\partial M_{2c}}{\partial \varphi} = \frac{2 D^{\varphi}_{mac}}{\omega^3} M_0 \tag{4. 17}$$

By applying the method of temporal moments, it can be shown that the macroscopic angular velocity ω_{mac} equals the mean rotational seepage velocity $\bar{\omega}$:

$$\bar{\omega} = \frac{2 Q_{tot}}{\theta\left(r_2^2 - r_1^2\right)\left(\Delta z - z_f\right)} \tag{4. 18}$$

At the large-distance limit, we can derive the macrodispersion coefficient in a closed form for the limiting cases of a) no molecular diffusion and b) only molecular diffusion. For a derivation of the closed form of the macrodispersion coefficient please refer to *Cirpka and Kitanidis* [2001b].

By neglecting the transverse dispersivity, $\alpha_t = 0$ ($\Rightarrow D_t = D$), we obtain:

$$\lim_{\varphi \to \infty} \frac{\partial M_{2c}}{\partial \varphi} = \frac{\left(\Delta z - z_f\right)\theta}{Q_{tot}} \frac{r_2^4\left(4\left(\ln\frac{r_2}{r_1}\right)^2 - 9\ln\frac{r_2}{r_1} + 6\right) + r_2^2 r_1^2\left(4\left(\ln\frac{r_2}{r_1}\right)^2 - 12\right) + r_1^4\left(4\left(\ln\frac{r_2}{r_1}\right)^2 + 9\ln\frac{r_2}{r_1} + 6\right)}{24\ln\left(\frac{r_2}{r_1}\right) D} \tag{4.19}$$

By neglecting the molecular diffusion, $D = 0$ ($\Rightarrow D_t = \alpha_t q_{\varphi}$), we obtain:

$$\lim_{\varphi\to\infty}\frac{\partial M_{2c}}{\partial\varphi}=\frac{\theta^2\left(\Delta z-z_f\right)^2}{Q_{tot}^2}\frac{\left(\frac{4}{15}\left(r_2^5-r_1^5\right)\ln\left(\frac{r_2}{r_1}\right)^2+\frac{8}{9}\left(r_1^2r_2^3-r_2^5+r_1^3r_2^2-r_1^5\right)\ln\left(\frac{r_2}{r_1}\right)+r_2^5-r_1r_2^4-2r_1^2r_2^3+2r_1^3r_2^2+r_1^4r_2-r_1^5\right)}{\alpha_t\ln\left(\frac{r_2}{r_1}\right)} \tag{4. 20}$$

Neglecting the effect of the early-time behavior on the value of M_{2c}, we get the following general relationship between M_{2c} at a given φ and Q_{tot}:

$$M_{2c}\left(D,0,Q_{tot}\right)=\frac{B}{Q_{tot}} \tag{4. 21}$$

$$M_{2c}\left(0,\alpha_t,Q_{tot}\right)=\frac{A(r_1,r_2,\alpha_t)}{Q_{tot}^2} \tag{4. 22}$$

in which coefficients A and B are given from equations (4.19 and 4.20).

We can approximate the combined effects of D and α_t by considering that the local dispersion contributions are additive and that macrodispersion is inversely proportional to transverse dispersion. Therefore we use the approximation:

$$\frac{1}{Q_{tot}M_{2c}\left(D,\alpha_t,Q_{tot}\right)}\approx\frac{1}{B}+\frac{Q_{tot}}{A} \tag{4. 23}$$

Equation (4.23) is the basis for the determination of α_t and D from a series of tracer experiments at different discharge. A linear regression of $Q_{tot}M_{2c}$ as a function of Q_{tot} yields the coefficient A and B that we used to determine α_t and D.

4.4. Impact of Pitch

4.4.1. Velocity Field

In the previous derivation, I have considered the limit $\Delta z \to 0$. Here, the flow was always into the angular direction, and no variation in the vertical direction occurred. I now evaluate the impact of the pitch $\Delta z > 0$. The pitch causes a vertical shift when following the angular direction along the flight. The vertical shift per rotation is identical for all radii. The corresponding path length, however, is smaller at the inside of the helix than at the outside. That is, the slope of the flight is higher at the inside than at the outside.

In a transfer from the ring ($\Delta z = 0$) to the helix, we would expect the flow to be parallel to the flight over the entire height of the cross-section. As a consequence, the vertical hydraulic gradient within the flight would be larger at the in- than at the outside. Figure 4. **2** shows the expected head-distribution. Obviously, because of the radial variation in the verti-

cal hydraulic gradient, a radial gradient occurs that, for the case of flow spiraling upwards enforces flow into the center of the helix at the upper part of section and outwards in the lower part. Continuity requires a downward motion at the inside and an upward motion at the outside.

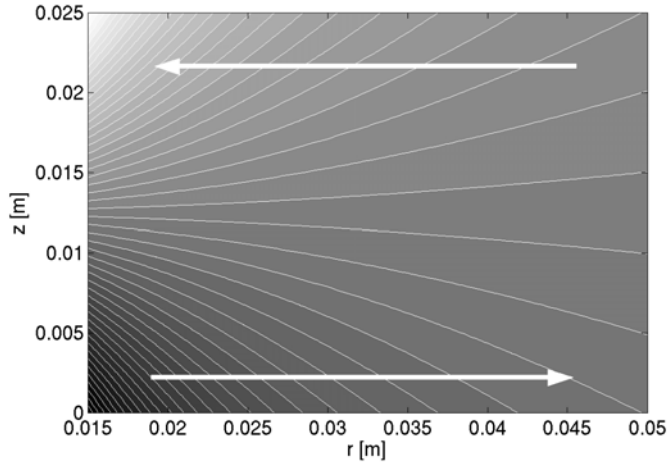

Figure 4. 2 Expected head distribution inside the helical column

Considering the system of helical coordinates, the steady-state continuity equation becomes:

$$\frac{2\pi}{\sqrt{4\pi^2 r^2 + \Delta z^2}} \frac{\partial(rq_\varphi)}{\partial\varphi} + \frac{\partial(rq_r)}{\partial r} + \frac{\partial(rq_z)}{\partial z} = 0 \tag{4. 24}$$

in which the specific-discharge vector in helical coordinates has the same length as in Cartesian coordinates. The helical components of the specific-discharge vector are:

$$\begin{aligned} q_\varphi &= -K\left(\frac{\sqrt{4\pi^2 r^2 + \Delta z^2}}{2\pi r^2}\frac{\partial h}{\partial\varphi} - \frac{\Delta z\sqrt{4\pi^2 r^2 + \Delta z^2}}{4\pi^2 r^2}\frac{\partial h}{\partial z}\right) \\ q_r &= -K\frac{\partial h}{\partial r} \\ q_z &= -K\left(\frac{4\pi^2 r^2 + \Delta z^2}{4\pi^2 r^2}\frac{\partial h}{\partial z} - \frac{\Delta z}{2\pi r^2}\frac{\partial h}{\partial\varphi}\right) \end{aligned} \tag{4. 25}$$

leading to the groundwater-flow equation in helical coordinates:

$$\frac{1}{r^2}\frac{\partial^2 h}{\partial\varphi^2} - \frac{\Delta z}{\pi r^2}\frac{\partial^2 h}{\partial z\partial\varphi} + \frac{1}{r}\frac{\partial h}{\partial r} + \frac{\partial^2 h}{\partial r^2} + \frac{4\pi^2 r^2 + \Delta z^2}{4\pi^2 r^2}\frac{\partial^2 h}{\partial z^2} = 0 \tag{4. 26}$$

subject to the boundary conditions:

$$q_z = 0 \text{ at } z = 0 \text{ and } z = \Delta z \tag{4. 27}$$

$$q_r = 0 \text{ at } r = r_1 \text{ and } r = r_2 \tag{4. 28}$$

At a sufficient distance from the in- and outlets, the angular hydraulic gradient becomes uniform:

$$\frac{\partial h}{\partial \varphi} = -J \;\forall \varphi, r, z \tag{4. 29}$$

which simplifies the *pde* for the hydraulic heads to:

$$\frac{\partial}{\partial \mathrm{r}}\left(\mathrm{r}\frac{\partial \mathrm{h}}{\partial \mathrm{r}}\right) + \frac{\partial}{\partial \mathrm{r}}\left(\frac{4\pi^2 \mathrm{r}^2 + \Delta \mathrm{z}^2}{4\pi^2 \mathrm{r}}\frac{\partial \mathrm{h}}{\partial \mathrm{z}}\right) = 0 \tag{4. 30}$$

subject to:

$$\frac{\partial h}{\partial z} = -\frac{2\pi\Delta z}{4\pi^2 r^2 + \Delta z^2} J \text{ at } z = 0 \text{ and } z = \Delta z \tag{4. 31}$$

$$\frac{\partial h}{\partial r} = 0 \text{ at } r = r_1 \text{ and } r = r_2 \tag{4. 32}$$

The components of the specific discharge in helical coordinates are now:

$$\begin{aligned} q_\varphi &= K\left(\frac{\sqrt{4\pi^2 r^2 + \Delta z^2}}{2\pi r^2} J + \frac{\Delta z\sqrt{4\pi^2 r^2 + \Delta z^2}}{4\pi^2 r^2}\frac{\partial h}{\partial z}\right) \\ q_r &= -K\frac{\partial h}{\partial r} \\ q_z &= -K\left(\frac{4\pi^2 r^2 + \Delta z^2}{4\pi^2 r^2}\frac{\partial h}{\partial z} + \frac{\Delta z}{2\pi r^2} J\right) \end{aligned} \tag{4. 33}$$

Back-transformation into Cartesian coordinates yields:

$$\mathbf{q_x} = -K\begin{bmatrix} \left(\frac{J}{r} + \frac{\Delta z}{2\pi r}\frac{\partial h}{\partial z}\right)\sin\varphi + \frac{\partial h}{\partial r}\cos\varphi \\ -\left(\frac{J}{r} + \frac{\Delta z}{2\pi r}\frac{\partial h}{\partial z}\right)\cos\varphi + \frac{\partial h}{\partial r}\sin\varphi \\ \frac{\partial h}{\partial z} \end{bmatrix} \tag{4. 34}$$

Thus, the specific discharge in Cartesian coordinates normal to the vertical reference frame is:

$$q_{nor}(r, z) = K\left(\frac{J}{r} + \frac{\Delta z}{2\pi r}\frac{\partial h}{\partial z}\right) \tag{4. 35}$$

Note that the secondary flow-field [q_r, q_z] is not conservative when interpreted as two-dimensional flow. This can be shown from the continuity equation in helical coordinates, taking into account $\partial h/\partial\varphi = 0$:

$$\frac{q_r}{r} + \frac{\partial q_r}{\partial r} + \frac{\partial q_z}{\partial z} = 0 \tag{4. 36}$$

which does not describe a conservative behavior in 2-D. However, the secondary motion times the radial coordinate r is conservative:

$$\frac{\partial(rq_r)}{\partial r} + \frac{\partial(rq_z)}{\partial z} = 0 \tag{4. 37}$$

which means that the secondary motion must be source-sink free in a slice of the helix which, obviously, is thicker at the outside than at the inside.

Figure 4.3 shows the head fluctuations within the vertical reference frame and streamlines calculated for the secondary motion [rq_r, rq_z].

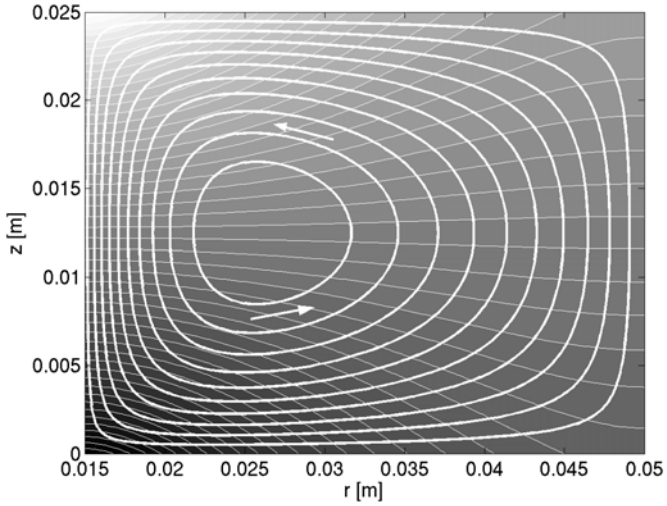

Figure 4.3 Head fluctuation within the vertical frame and streamlines calculated for the secondary motion

4.4.2. Forward Simulation by Particle-Tracking Random-Walk

The forward model is developed *Benekos* [2004] at the department of Civil and Environmental Engineering at Stanford University, USA.

If we consider the secondary-flow field, for which we don't have a closed-form solution, we can evaluate the concentration distribution within the helix and the breakthrough curve at its outlet only by numerical simulation. In order to prevent numerical dispersion, we apply the particle-tracking random walk method [*Prickett et al., 19*81]. Here, the advection-

dispersion equation, Eq. (2.16.), is rewritten in the form of the Fokker-Plank equation [*Tompson et al., 1990*]:

$$\frac{\partial c}{\partial t} + (v - \nabla \mathbf{D}) \cdot \nabla c - \mathbf{D} \nabla^2 c = 0 \qquad (4.38)$$

The particle tracking consist of three motions: the advective motion $(v \cdot c)$, the Brownian motion $(-\mathbf{D}\nabla^2 \cdot c)$, and the drift motion $(-\nabla \mathbf{D} \cdot \nabla c)$, [*Prickett et al., 1981*, *Kinzelbach, 1986*, *Pollock, 1988*, *Anderson, 1992* and *Zheng and Bennet, 1995*]. In the Lagrangian framework, we express the concentration c by the spatial density of the solute particles. Then, the advective and the drift motions result in a spatial displacement of $\int_t^{t+\Delta t} (v - \nabla \mathbf{D})\, d\tau$, whereas the parabolic term $(-\mathbf{D}\nabla^2 \cdot c)$ is simulated as Brownian motion with spatial covariance matrix $2\Delta t\, \mathbf{D}$. As demonstrated by [*Kitanidis 1994b*], applying explicit Euler integration in time results in the first-order scheme:

$$x_{t+\Delta t} = x_t + (v - \nabla \cdot \boldsymbol{D})_{xt} \Delta t + \sqrt{2\Delta t} L(x_t) \xi \qquad (4.39)$$

in which x_t is the Cartesian coordinates of a single particle at time t, ξ is a vector containing random numbers taken from a standard normal distribution, and L is the lower Cholesky decomposition of the dispersion tensor meeting:

$$L(x_t)\, L^T(x_t) = D(x_t) \qquad (4.40)$$

Here, the drift motion appeared to be non-significant and is therefore ignored.

At time zero, the domain is concentration-free:

$$C(t) = 0, \varphi > 0) = 0 \qquad (4.41)$$

which implies that all particles start at the inlet screen. *Benekos* applies a Dirac-pulse injection into the flux by distributing the particles in the inlet of the helix inversely proportional to the radius and uniformly over the height of the inlet screen.

Figure 4.4 comparing the simulated advective travel-time distributions in the outflow of helix with and without pitch. The geometric parameters are identical to those of the helix used in the experiment described below. Obviously, the secondary motion decreases the spread of the breakthrough curve. Interpreting the second central moment with the regression technique described in section 4.3 would yield transverse dispersion coefficient that, in the simulated reality, should be zero. In the particle tracking model, *Benekos* uses a model based

on the Finite Element Method (FEM) for solving Eqn. 4.30 and obtain the hydraulic gradients needed in the computational of the velocities.

In my experiments, I inject the tracer solution continuously, which relates to a Heaviside rather than Dirac-pulse boundary condition with respect to time. This breakthrough curve is given by the cumulative distribution function (CDF) of the particle arrival times in the outlet of the helix for particles starting at identical time.

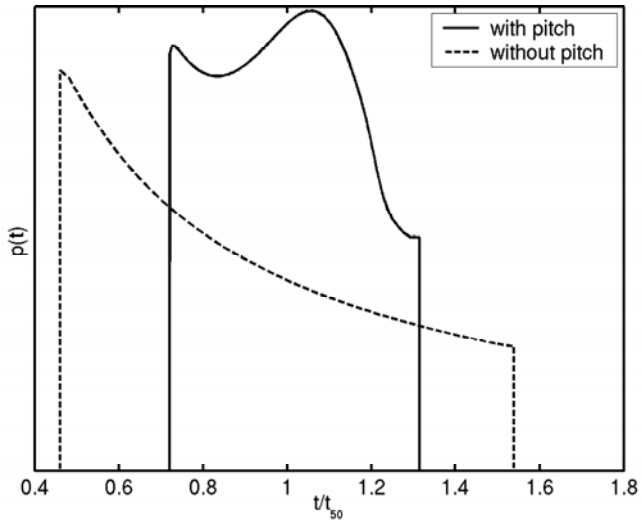

Figure 4.4 A comparison of the advective travel-time distribution considering with pitch and without pitch

4.4.3. Levenberg-Marquardt Optimization

Benekos [2004] used the Levenberg-Marquardt method in order to estimate the transverse dispersion parameters. As objective function W, he used the sum of squared residuals ε:

$$W = \varepsilon \cdot \varepsilon \tag{4. 42}$$

$$\varepsilon = \mathbf{c}_{meas} - \mathbf{c}_{sim}(\mathbf{p}) \tag{4. 43}$$

in which $\mathbf{c}_{\text{meas}}$ is the vector of measured normalized concentrations in the out flow at times $t_i = 0, \Delta t, \Delta 2t, ...m\Delta t,$ and $\mathbf{c}_{sim}(\mathbf{p})$ is the corresponding vector of simulated values using the set of dispersion parameters $\mathbf{p}$. The Levenberg-Marquardt method is a stabilized version of the Gauss-Newton method, in which he has updated the parameter vector in the $(k+1)$-th step by:

$$\mathbf{p}_{k+1} = \mathbf{p}_k - \left(\mathbf{J}_k^T \mathbf{J}_k + \mu_k \mathbf{I}\right)^{-1} \mathbf{J}_k^T \boldsymbol{\varepsilon}_k \tag{4. 44}$$

with the Jacobian $$\mathbf{J}_k = \left.\frac{\partial \mathbf{c}_{sim(\mathbf{p})}}{\partial \mathbf{p}^T}\right|_{\mathbf{p}=\mathbf{p}_k} \tag{4. 45}$$

and the Levenberg-Marquardt parameter μ_k which is adapted according to the convergence of the solution. In particular, when $\left\|\left(\mathbf{J}_k^T \mathbf{J}_k\right)^{-1} \mathbf{J}_k^T \boldsymbol{\varepsilon}_k\right\|_2$ becomes smaller than a predefined level δ, we set μ_k to zero thus retaining the standard Gauss-Newton method. Several criteria and tests for convergence are proposed in Dennis et al., 1981a. He has used two criteria to test the convergence of the procedure. The first one is that the objective function W has to be below a tolerance level. The second one is the orthogonality criterion proposed by *Bates and Watts*, 1981:

$$\cos\phi = \frac{\varepsilon^T \mathbf{J}\left(\mathbf{J}^T \mathbf{J}\right)^{-1} \mathbf{J}^T \varepsilon}{\left\|\mathbf{J}\left(\mathbf{J}^T \mathbf{J}\right)^{-1} \mathbf{J}^T \varepsilon\right\|_2 \cdot \|\varepsilon\|_2} < tolerence \tag{4. 46}$$

Orthogonality means that the residual vector has zero projection on to the tangent plane. And so we may use the length of this projection as an indicator for obtaining a local minimum. Contrary to the absolute function criterion, which is a termination criterion, the orthogonality criterion assures convergence.

4.5. Experimental Description

Fluorescence intensity of fluorescein was measured by optic fiber probes at the in- and outlet of the helix. The optic fiber probes are connected to a fluorometer. A personal computer is used for continuous data acquisition. Details of the measurement techniques are given in chapter 3. To prevent reduction of the hydraulic conductivity by entrapped gas, the unsaturated column was first flushed with gaseous carbon dioxide and subsequently with degassed water dissolving all gas. At first, 3 pore volumes of carbon dioxide gas were passed through the column from top to bottom displacing air from the pores. After passing the carbon dioxide, the column was saturated by slowly injecting degassed-deionized water to the column from top to bottom. Three pore volumes of water were passed through the column to reach fully saturated conditions. A constant linear relationship between head difference and discharge was used as criterion whether the column had reached fully saturated conditions. The degassed-deionized water was passed for 48 hours to be sure that all the carbon dioxide gas dissolved into the water.

Prior to injection of the tracer into the helical column, water was passed through the column at a constant discharge by applying a head difference between inlet and outlet of the helix. Starting at some time $t_{0,}$ a tracer was injected continuously into the porous medium. I measured the breakthrough curve at the outflow of the helix. Due to the velocity profile, the concentrations at the inner radius of the cross section contribute more to the mean mass flux than those at the outer radius. Therefore, the measured concentration is flux-averaged. The experimental setup is shown in Figure 4. 5.

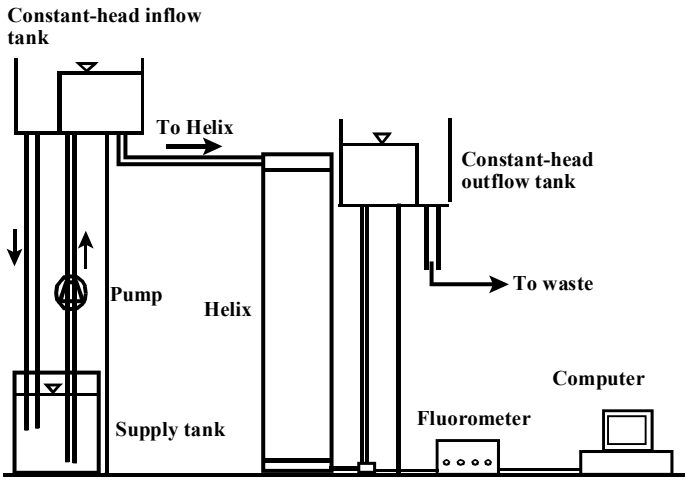

Figure 4. 5 Experimental setup of the helical column experiments

4.6. Results

4.6.1. Experimental Results

I present five experiments each with different discharge rate to distinguish between the contributions of molecular diffusion and hydrodynamic dispersion to transverse dispersion. The measured concentrations are normalized by the inflow concentration, so that the concentration values in the breakthrough curves, shown in Figure 4. 6, range from zero to one.

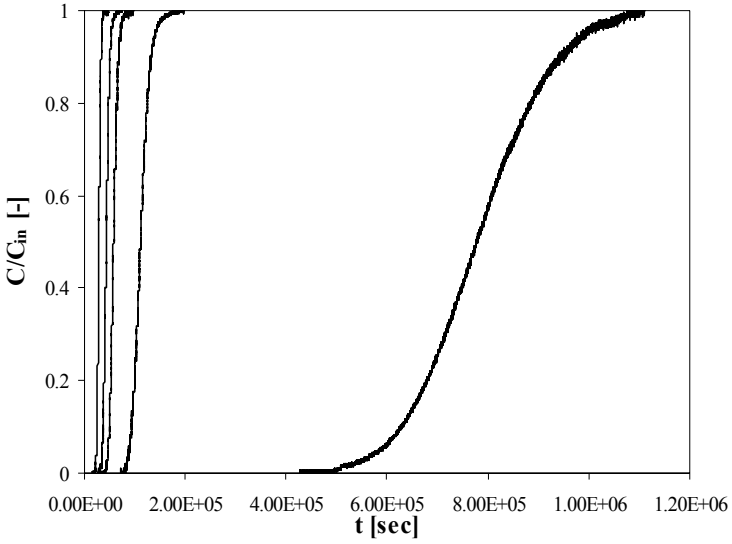

Figure 4. 6 Normalized breakthrough curves as a function of real time for the different experiments.

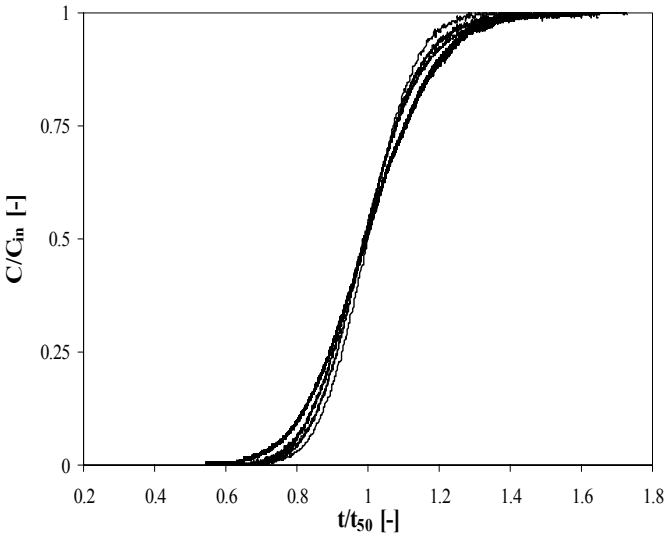

Figure 4. 7 Normalized concentration breakthrough curves plotted in a normalized time axis. The time axis is normalized by the mean arrival time t_{50} of the tracer front

The duration of the experiments ranged from a few hours to several days. Figure 4. 7 shows the concentration breakthrough curves in dimensionless axes. Here, the time is divided by the mean arrival time of the concentration front denoted by t_{50}. The curve in Figure 4. 7 with the most spreading refers to the experiment with the lowest discharge rate (experiment 5 in Table 4. 1), and the curve with the least spreading to that with the highest discharge rate (experiment 1 in Table 4. 1). That is, the macroscopic Peclet number $Pe_{mac} = \omega_{mac}\varphi/D^{\varphi}_{mac}$ increases with discharge rate.

I determine the apparent macroscopic parameters D^{φ}_{mac} and ω_{mac} by fitting the analytical solution of [*Ogata and Banks, 1961*] for the Heaviside problem to the measured data. From the fitted macroscopic parameters, I derive the temporal moments M_{2c} and M_1 by using eqn. (4.16) and (4.17) and compare them to the moments calculated directly from the breakthrough curves. The comparison gives us a measure for the error in M_{2c} and M_1. The effective porosity θ_e is calculated by $\theta_e = \Omega / \omega_{mac}$ in which Ω is the angular rotational specific discharge:

$$\Omega = \frac{2\mathrm{KJ}\ln\left(\frac{r_2}{r_1}\right)}{r_2^2 - r_1^2} \tag{4. 47}$$

As listed in Table 4. 1, the estimated first moment M_1 has an error < 1% for all experiments except experiment 5 where it has a value of 2.67%. As a consequence, we get consistent estimates of the porosity. Similarly, the estimated second central moment M_{2c} has relative error < 10% except in experiment 5 where more time should have been allowed in order to capture the full tail of the breakthrough curve.

Figure 4. 8 shows a linear regression of $(Q_{tot}M_{2c})^{-1}$ as a function of Q_{tot} for the measured data. Obviously, coefficients A and B of Eq. (4.23) are the inverse of the slope and the intercept of the regression line. Considering eq. (4.19) and (4.20), we can approximate D and α_t from A and B by:

$$D = \frac{\Delta\varphi}{B}\theta_e \frac{r_2^4\left(4\left(\ln\frac{r_2}{r_1}\right)^2 - 9\ln\frac{r_2}{r_1} + 6\right) + r_2^2 r_1^2\left(4\left(\ln\frac{r_2}{r_1}\right)^2 - 12\right) + r_1^4\left(4\left(\ln\frac{r_2}{r_1}\right)^2 + 9\ln\frac{r_2}{r_1} + 6\right)}{24\ln\left(\frac{r_2}{r_1}\right)} \tag{4. 48}$$

$$\alpha_t = \frac{\Delta\varphi}{A}\theta_e^2 \frac{\left(\frac{4}{15}\left(r_2^5 - r_1^5\right)ln\left(\frac{r_2}{r_1}\right)^2 + \frac{8}{9}\left(r_1^2 r_2^3 - r_2^5 + r_1^3 r_2^2 - r_1^5\right)ln\left(\frac{r_2}{r_1}\right) + r_2^5 - r_1 r_2^4 - 2r_1^2 r_2^3 + 2r_1^3 r_2^2 + r_1^4 r_2 - r_1^5\right)}{ln\frac{r_2}{r_1}}$$

Table 4. 1 Parameters calculated from different experiments

Parameter	Experiment				
	1	2	3	4	5
Total Discharge, Q_{tot} [m^3/s]	1.5×10^{-7}	1.0×10^{-7}	7.5×10^{-8}	3.8×10^{-8}	5.55×10^{-9}
First Moment, M_1 [s]	2.88×10^{4}	4.38×10^{4}	5.82×10^{4}	1.12×10^{5}	7.89×10^{5}
	±0.25%	±0.20%	±0.57%	±2.67%	±0.12%
Second Central Moment, M_{2c} [s^2]	9.78×10^{6}	2.96×10^{7}	5.18×10^{7}	2.31×10^{8}	1.64×10^{10}
	±9.6%	±6.4%	±4.8%	±9.0%	±25.0%
Angular Rotational Specific Discharge, Ω [1/s]	0.0053	0.0035	0.0026	0.0013	0.00019
Macroscopic Rotational Velocity, ω_{mac} [1/s]	0.0131	0.0086	0.0065	0.0034	0.00048
Macroscopic Angular Dispersion Coefficient, D^{φ}_{mac} [1/s]	0.0290	0.0251	0.0181	0.0116	0.0024
Macroscopic Peclet Number [-]	170	129	131	109	76
Effective Porosity, θ_e [-]	0.403	0.408	0.407	0.401	0.405

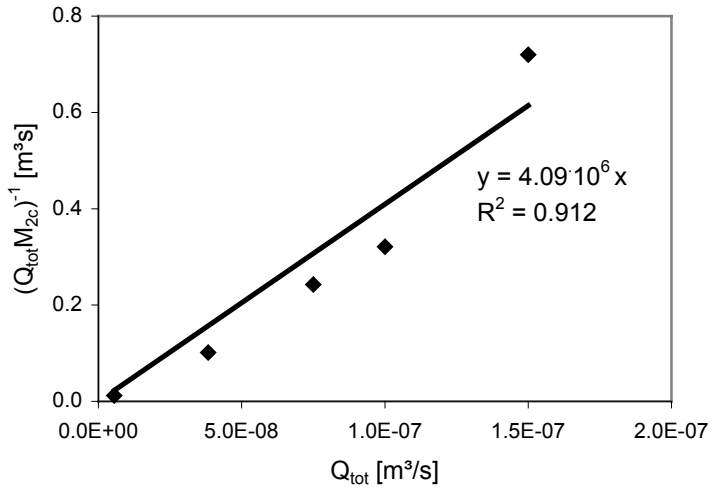

Figure 4. 8: Linear regression of $(Q_{tot}M_{2c})^{-1}$ as a function of Q_{tot} for the given data

The discharge rates are fairly high in all experiments. At these rates, molecular diffusion contributed marginally to local transverse dispersion. As a consequence, I am not able to estimate D from the data. In fact, the intercept of the regression was negative.

As noted above, eqn. (4.19) and eqn. (4.20) refer to the large-distance limit. Therefore, early-time effects on M_{2c} are neglected in the regression-based analysis. I use the result-

ing values α_t and D as initial guess in a Gauss-Newton scheme that uses a numerical solution of the moment-generating equations accounting for the entire time range. Table 4. 2 shows the initial guess for parameters α_t, D, and θ_e as well as their final estimates computed by the Gauss-Newton method. As in the regression-based analysis, I am not able to determine the diffusion coefficient from the data.

Table 4. 2 Initial guess and final estimate for parameters *D*, α_t, and θ_e

Parameter	Initial guess	Final estimate
D [m^2/s]	Set to 0	Set to 0
α_t [m]	7.27×10^{-4}	6.57×10^{-4}
θ_e	0.404	0.405

4.6.2. Simulations Results

The basic assumption in the analytical approach was that transverse dispersion is the only process leading to radial exchange of the solute [*Cirpka and Kitanidis, 2001b*]. With the secondary flow, however, we have a second mechanism leading to mass transfer in the z –r plane. *Benekos* [2004] simulated conservative transport in the helix by particle-tracking random walk of 5000 particles. The flow-field is simulated by solving Eqn. 4.25. to Eqn 4.31 using the Galerkin Finite Element Method (FEM) with bilinear elements. A few tests were performed for validating the particle tracking model. The velocities in the particle tracking model obtained using the two-dimensional FEM compared with the ones obtained from a three-dimensional FEM with tri-linear elements where Darcy's equation is solved for the entire helical column. The velocities obtained from these two models agreed.

In our model, we use the two-dimensional FEM which is computationally less intensive. In addition, the second central moment M_{2c} as a function of φ obtained with the particle tracking model when the secondary flow are neglected matched the M_{2c} obtained at the same locations by FEM simulations using the Streamline-Upwind-Petrove-Galerkin (SUPG) methods of *Brooks and Hughes,* [1982] neglecting the secondary flow.

The particle-tracking simulations show that the secondary flow may have a significant impact on transverse mixing. We perform particle tracking with and without the secon-

dary flow component in order to assess its compact on the spread of the breakthrough curve. Figure 4. 9 shows plots of M_{2c} normalized by the zeroth moment M_0 as a function of the angel φ in the helix (M_{2c}^{sec} in the case that secondary flow was considered). The solid lines show results when secondary flow is neglected, and the circles when the secondary flow is considered. In this example-simulations the parameters are: hydraulic head difference $\Delta H = 2.33$ m, hydraulic conductivity $K = 8.19 \times 10^{-3}$ m/sec, effective porosity $\theta_e = 0.4$, transverse dispersivity $\alpha_t = 5.52 \times 10^{-4}$ m and the effective diffusion coefficient $D_m = 10^{-9}$ m²/sec. The relative difference $\left(\partial M_{2c}/\partial\varphi - \partial M_{2c}^{sec}/\partial\varphi\right)/(\partial M_{2c}/\partial\varphi) \times 100\%$ is 30% in this example. Because everything scales with the average velocity in the transport equation (as long as the hydrodynamic part of the transverse dispersion is orders of magnitude larger than the effective molecular diffusion), the relative difference $\left(\partial M_{2c}/\partial\varphi - \partial M_{2c}^{sec}/\partial\varphi\right)/(\partial M_{2c}/\partial\varphi) \times 100\%$ remains the same for the same α_t irrespectively of the value of the hydraulic gradient. Simulations were performed where α_t and D_m were kept constant with the same values as the one used in the aforementioned example and the hydraulic head varied from simulation to simulation. The relative difference $\left(\partial M_{2c}/\partial\varphi - \partial M_{2c}^{sec}/\partial\varphi\right)/(\partial M_{2c}/\partial\varphi) \times 100\%$ remained equal to 30% for all simulations. However, when the hydrodynamic part of the transverse dispersion became of the same order of magnitudes as the effective molecular diffusion, the relative difference $\left(\partial M_{2c}/\partial\varphi - \partial M_{2c}^{sec}/\partial\varphi\right)/(\partial M_{2c}/\partial\varphi) \times 100\%$ decreased. This is expected when the hydrodynamic dispersive mixing is not the controlling mechanism of transverse dispersion. The impact of the secondary flow becomes insignificant if the molecular diffusion becomes the dominant mixing mechanism. We conclude that the secondary flow due to the presence of the pitch may have a significant effect on longitudinal macrodispersion in the case where hydrodynamic portion of the transverse dispersion is large compared to the effective molecular diffusion. Therefore, neglecting the pitch and the resulting flow anomaly in the analysis of the tracer test is prohibited. In this case, the analytical expressions presented by [Cirpka and Kitanidis, 2001b] are not applicable.

Here, the estimate the transverse dispersivity by applying the Levenberg-Marquardt method to the particle-tracking method. In a domain with helical geometry, the contribution of α_l to the second central moment is orders of magnitude smaller than the contribution of α_t. Thus we set α_l to a fixed value of 0.001m. D_m was fixed to 1×10^{-9} m²/s which is rather typical value for small molecules and ions in water at room temperature (International Critical

Tables). For assessing the sensitivity of the optimization procedure a base case simulation of the particle-tracking model is performed. Subsequently, the parameters α_t and θ_e are repeatedly updated by the Levenberg-Marquardt method. The iterative procedure is terminated when both the absolute function criterion and the orthogonality criterion, Eqn. 4.46 are met. Table 4. **3** shows the results for one of these simulations.

Table 4. **4** includes the estimated parameters for the fluorescein experiments. **Figure 4.10** shows the comparison between the measured and fitted breakthrough curves for one of these experiments.

Table 4. 3 Parameters values for the base case and estimated values after the optimization procedures and convergence criteria values

	Parameters	
	α_t [m]	θ_e [-]
Base case	10^{-4}	0.35
Initial case	3×10^{-5}	0.40
Estimated values	1.2×10^{-4}	0.3493
Convergence criteria		
Absolute	0.0043	
Orthogonality	0.032	

Table 4. 4 Estimated parameters with the Levenberg-Marquardt optimization scheme for the fluorescein experiments

Tracer	**Fluorescein**				
Experiment	**1**	**2**	**3**	**4**	**Average**
α_t	5.52×10^{-4}	3×10^{-4}	3.5×10^{-4}	3.15×10^{-4}	3.82×10^{-4}
θ_e	0.400	0.421	0.403	0.398	0.406

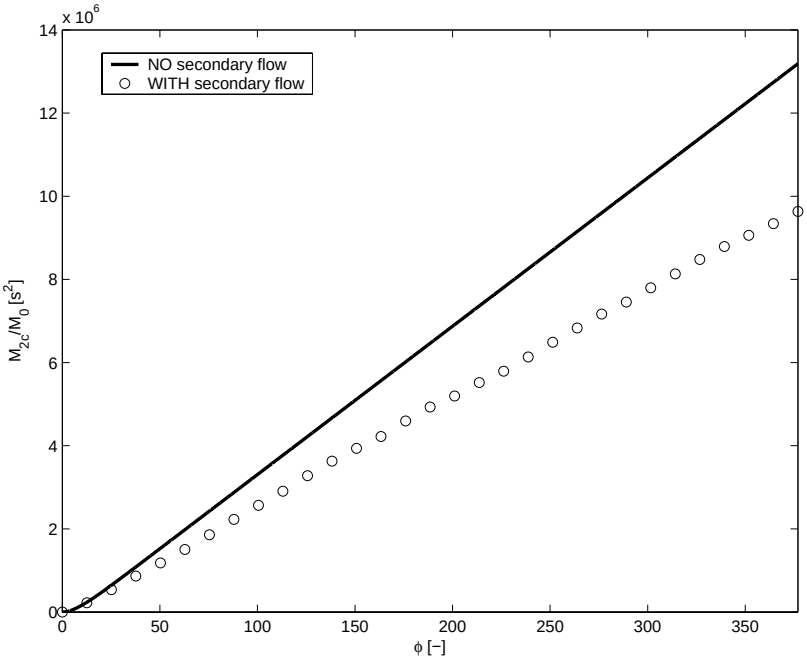

Figure 4. 9 Plot of the normalized second central moment ($\partial M_{2c}^{sec}/M_0$ and $\partial M_{2c}/M_0$ for the case with and without the secondary flow respectively) as a function of the angle location φ .

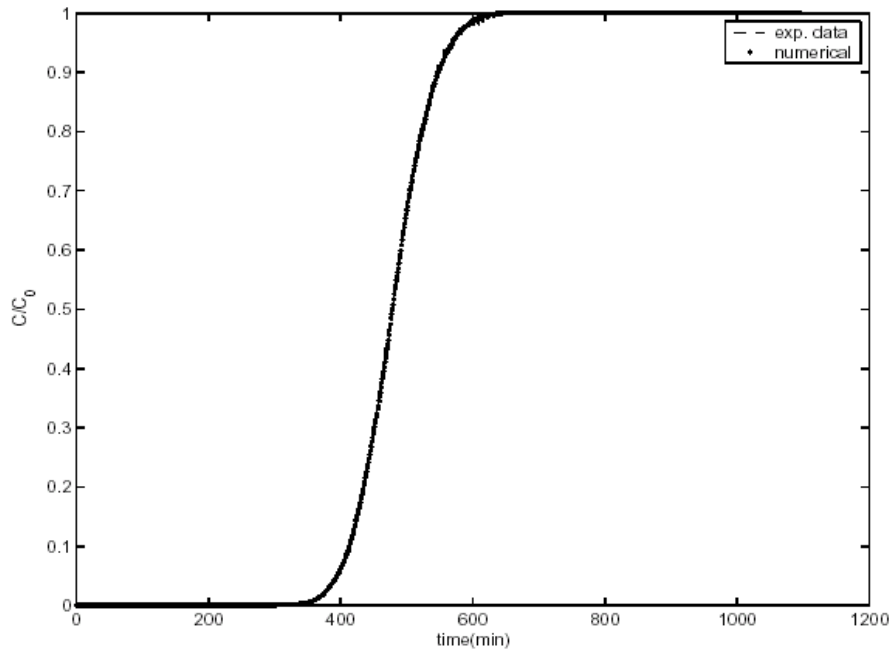

Figure 4.10 Experimental and simulated breakthrough curves for experiment 1.

4.7. Discussion and Conclusions

I present an experimental method for the determination of pore-scale transverse dispersion coefficients that is based on Taylor-Aris dispersion in a helical domain. I measure the

spread of the breakthrough curve, which is inversely proportional to the local transverse dispersion coefficient. This is advantageous, because transverse-dispersion parameters are generally small.

I perform five tracer experiments with different discharge rates (1.5×10^{-7} m³/s to 5.55×10^{-9}m³/s). I estimate the local transverse dispersivity using analytical expressions for the angular macrodispersion coefficient in the large-time limit, resulting in a value of $\alpha_t = 7.27\times10^{-4}$m**.** I use this value as initial guess in a Gauss-Newton scheme based on a numerical solution of the moment generating equations accounting for the entire time range. The final estimate computed by the Gauss-Newton method is 6.57×10^{-4}m. In neither case, I am able to determine the diffusion coefficient from the data. A possible explanation for this behavior might be that the discharge rates were fairly high in all experiments. The mean rotational seepage velocity varied from 0.27 rotations per hour to 7.5 rotations per hour. At these rates, molecular diffusion contributed marginally to local transverse dispersion.

The optimization approach for determining the transverse dispersivity coupled with the numerical simulation of the transport in the helix reveals that the secondary flow can have implications that need to be considered. The secondary flow depends entirely on the hydraulic gradient and the helix characteristics whether the transverse dispersivity is a property of the porous medium and its geometry. Particle-tracking simulations show that neglecting the secondary flow may result in significant differences in the determination of $\partial M_{2c}/\partial\varphi$. The relative impact of the secondary flow in the second central moment of the concentration breakthrough curve remains independent of the discharge as long as the hydrodynamic dispersion is the controlling transverse dispersion mixing mechanism. A comparison between the Levenberg-Marquardt optimization based on particle tracking considering the secondary motion and the regression technique neglecting secondary motion presented shows smaller values of α_t when accounting for the secondary motion. As the first moment hardly affected by the secondary motion, the estimates of the porosity by the two methods agreed well.

5. Determination of Transverse Dispersion coefficient in Homogeneous Porous Media

5.1. Introduction

A non-invasive imaging technique is developed for the determination of transverse dispersion coefficient in a quasi two dimensional model aquifer system by performing conservative and reactive tracer test. A more detailed description of the imaging techniques is given in the master's thesis of Qingsong Ju (2003).

5.2. Conservative Tracer Test

A conservative tracer Cochineal Red 80 E 124 with a concentration of 0.3 gm/l is used as a tracer for the experiment. Color intensity of the media are recorded by a digital camera, and stored on a computer. Details of the measurement techniques are already mentioned in chapter 3.6. The model aquifer was filled homogeneously with sand sizes of 1.0 mm – 2.5mm. The detailed descriptions of the mode aquifer and the filling procedures are described in section 3.3 and 3.4, respectively. To prevent reduction of the hydraulic conductivity by entrapped gas, the unsaturated aquifer was first flushed with gaseous carbon dioxide and subsequently with degassed water dissolving all gas. At first, 6 pore volumes of carbon dioxide gas were passed through the aquifer for displacing air from the pores. After passing the carbon dioxide, the model aquifer was saturated by slowly injecting degassed-deionized water. Three pore volumes of water were passed through the aquifer to reach fully saturated conditions.

While the tracer solution was pumped to the horizontal well, degassed-deionized water was simultaneously pumped into the inlet chamber to pass through the entire domain. After injecting four pore volumes of tracer solution to the aquifer, the plume reached steady state, Ju took digital photos and stored on a computer. The schematic diagram of the experimental setup is shown in

Figure 5. 1.

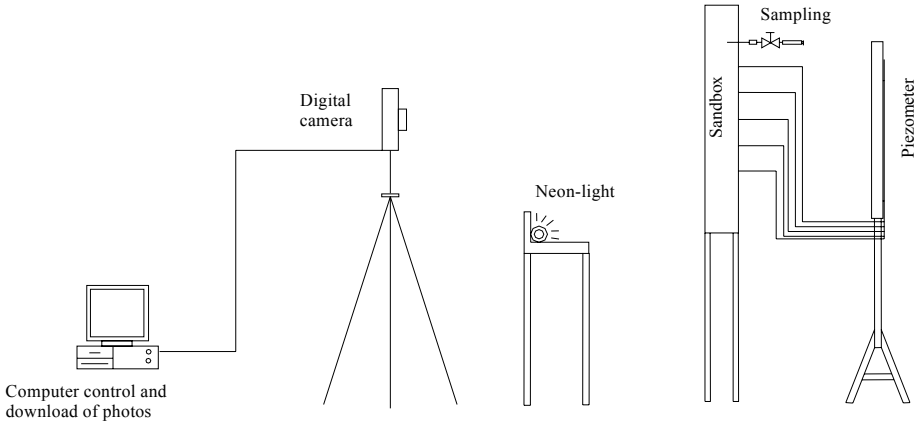

Figure 5. 1 Schematic of experimental setup (side view)

5.3. Determination of transverse dispersion coefficient

In a uniform flow field, the solute transport equation (2.16) of conservative solutes can be rewritten for three-dimensional transport in a porous medium as follows:

$$\frac{\partial c}{\partial t} + +v\frac{\partial c}{\partial x} - D_x\frac{\partial^2 c}{\partial x^2} - D_y\frac{\partial^2 c}{\partial y^2} - D_z\frac{\partial^2 c}{\partial z^2} = 0 \qquad (5.1)$$

where c[M/L³] is the volumetric concentration of the solutes, v [L/T] is the seepage velocity orientated in the x-direction, D_x, D_y and D_z [L/T²] are the longitudinal and two transverse dispersion coefficients, lumping effective molecular diffusion and pore-scale mechanical dispersion, x, y and z [L] are the longitudinal and the two transverse spatial coordinates, and t [T] is the time.

Furthermore, for large Peclet numbers, *Pe* =xv/Dx >30, we may neglect longitudinal dispersion [*Domenico and Robbins, 1985*]. Then, the three dimensional steady-state transport equation simplifies to:

$$\frac{\partial c}{\partial t} - \frac{D_y}{v}\frac{\partial^2 c}{\partial y^2} - \frac{D_z}{v}\frac{\partial^2 c}{\partial z^2} = 0 \qquad (5.2)$$

Domenico and Robbins [1985] developed analytical solutions to equations (5.2) for conservative transport neglecting longitudinal dispersion coefficient, in a 2-dimensional aquifer under a uniform flow velocity, where solute is continuously injected at a constant line source. The following equation gives the solution for the steady state of the plume.

$$c(x,y) = \frac{C_0}{2}\left(erf\left(\frac{y + b/2}{2}\sqrt{\frac{v}{D_T x}} \right) - erf\left(\frac{y - b/2}{2}\sqrt{\frac{v}{D_T x}} \right) \right) \quad (5.3)$$

where b is the size of the source in the y direction, D_T is the transverse dispersion Coefficient.

Here, I rewrite the equation (2.1), which commonly used for the parameterization for transverse dispersion [Fetter, 1993]

$$D_T = \alpha_T v + D_e^* \quad (5.4)$$

5.4. Preprocessing of Color Images

Although the images are taken under reproducible conditions, the spatial representation of identical objects on two images, taken at different times, may not match on a pixel-by-pixel basis. This may be the result of removing and re-installing the camera, as the same camera is used for all windows. In order to correct for geometric miss-representation, each window contains markers in the bottom left and top right corners. The digital images belonging to the same window are rotated and shifted so that the markers have identical pixel coordinates.

In addition to the geometric correction, the images need to be color-calibrated. To do so, I attached color cards to each window. For calibration, I analyze the representation of a grey color bar on each image. Ideally, the values of the red (R), green (G), and blue (B) color channels should linearly range from 0 to 255. In order to correct the color representation of the images taken, I use the γ-calibration model, applied individually to each color channel. For the red channel, I get:

$$R_{corr}(i,j) = a_R + b_R \times \left(R_{meas}(i,j)\right)^{\gamma_R} \quad (5.5)$$

in which $R_{meas}(i,j)$ and $R_{corr}(i,j)$ are the measured and corrected values of the red channel at the pixel with indices *i* and *j*. The coefficients a_R, b_R, γ_R are the correction parameters, assumed spatially uniform. I use the same function to calibrate the green and blue channels, here with coefficients a_G, b_G, γ_G and a_B, b_B, γ_B, respectively. The values of the correction parameters are determined by fitting the measured color intensities of all points belonging to the color bar to the ideal linear model. I use the squared deviation between the corrected color values and the linear model as objective function and apply the Nelder-Mead simplex algorithm for optimization [*Nelder & Mead*, 1965].

After geometric correction and color calibration, all images of the same window can be quantitatively compared to each other in a quantitative way. In the following analysis, I assume that the color intensity depends linearly on the concentration of the tracer. Since the

colors of the individual sand grains vary, however, the parameters mapping the color intensities to the tracer concentration differ from pixel to pixel

For the quantification of concentrations during the conservative-tracer experiment, I need two reference experiments. In the first, I pass tracer-free degassed-deionized water through the domain. Here, the normalized tracer concentration X [-] is zero. I denote the color intensities of this experiment R_0, G_0 and B_0. In the other reference experiment, the entire domain is filled with a tracer solution at maximum concentration. Here, the normalized tracer concentration is unity, and I denote the color intensities R_{max}, G_{max}, and B_{max}. In the image analysis, I use only the blue and green components, since the red component hardly differs with the concentration of the red dye. For monochromatic light, the attenuation should follow Lambert's exponential law. Because the light is not monochromatic, the concentration-intensity relationship differs from the ideal behavior. In a series of test experiments with various concentrations, I determined the following dependence of the normalized concentration $X(i,j)$ at pixel (i,j) from the color intensities of the blue and green picture components:

$$X(i,j) = \frac{1}{2}\left(\frac{\ln(G_0) - \ln(G_{corr})}{\ln(G_0) - \ln(G_{\max})}\right)^{1.4} + \frac{1}{2}\left(\frac{\ln(B_0) - \ln(B_{corr})}{\ln(B_0) - \ln(B_{\max})}\right)^{1.4} \tag{5. 6}$$

Finally, I transform the pixel-coordinates into spatial coordinates. All routines for image processing are written as Matlab scripts.

.

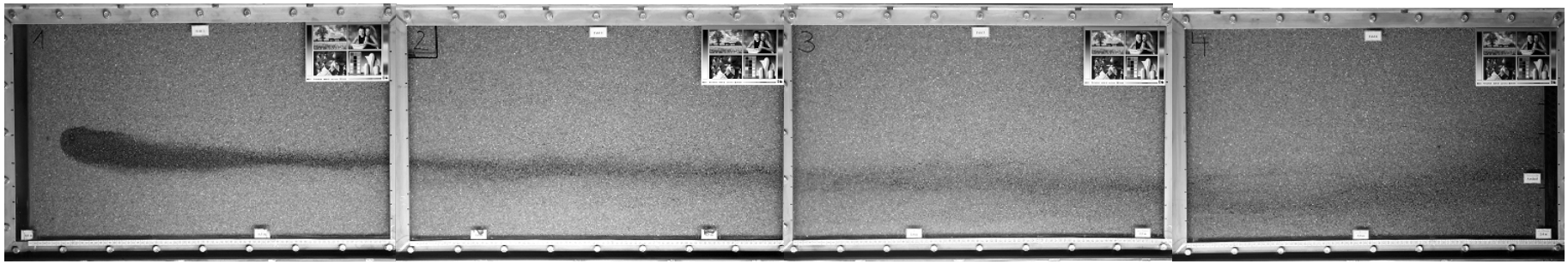

Figure 5. 2 Conservative tracer concentration profile (experimental data)

5.5. Results

Figure 5. **2** shows the conservative plume with a injection width of 7 cm. Figure 5. **3** to Figure 5. **8** show the steady-state concentration profiles at the positions down gradient 0.05m, 1.019m, 1.74m, 2.00m, 2.62m and 3.00m. I use the analytical solution (see section 5.3) to fit the experimental data. Two parameters, the transverse dispersivity α_T and the effective injection source width *h* determine the shape of the concentration profile. The effective source width *h* needed to be fitted because of the heterogeneity in the porous medium.

Using the MATLAB optimization function "fminsearch", the best-fit-curves of the experimental data are shown as bold line. The fminsearch function uses the Nelder-Mead simplex (direct search) method to minimize the error between the best-fit-curve and the experimental data.

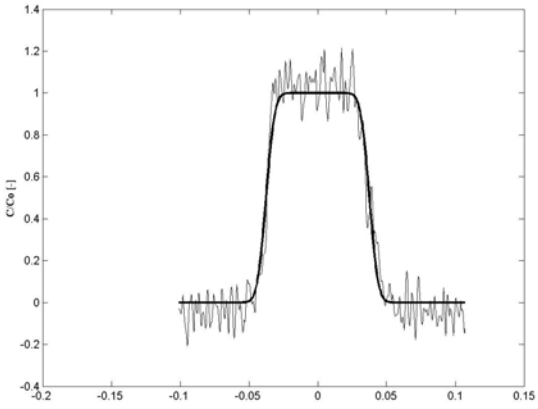

Figure 5. 3 Concentration profile 0.05m down gradient from the injection source

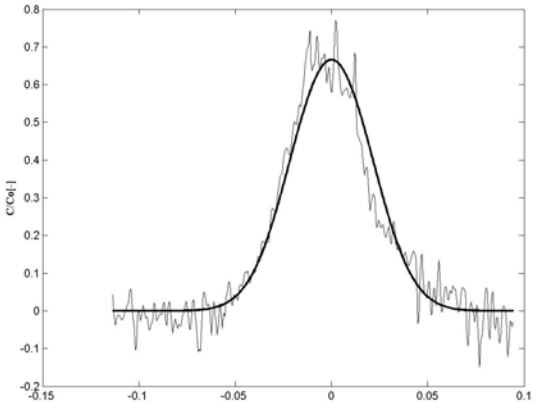

Figure 5. 4 Concentration profile 1.019m down gradient from the injection source

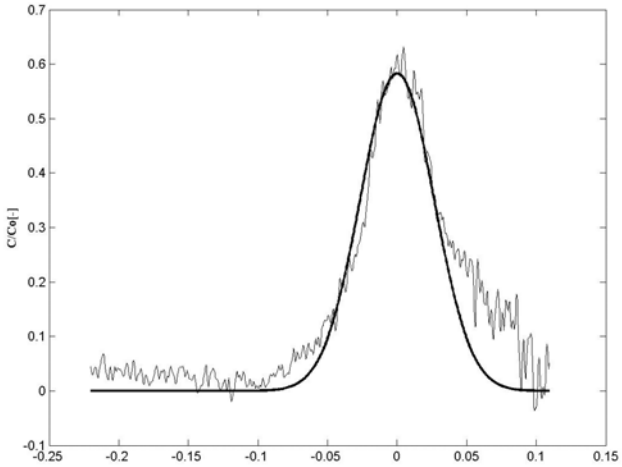

Figure 5. 5 Concentration profile 1.74m down gradient from the injection source

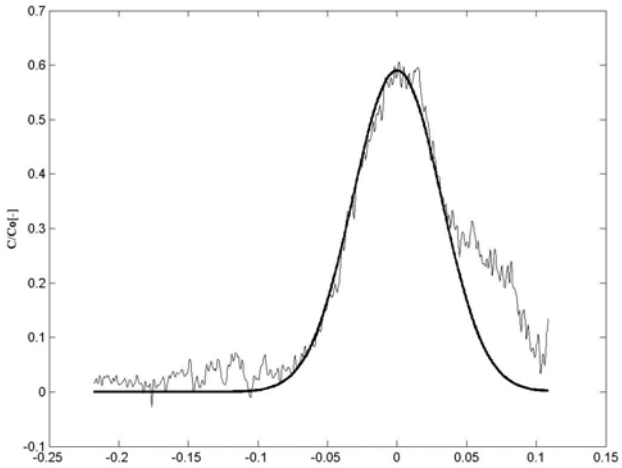

Figure 5. 6 Concentration profile 2.00m down gradient from the injection source

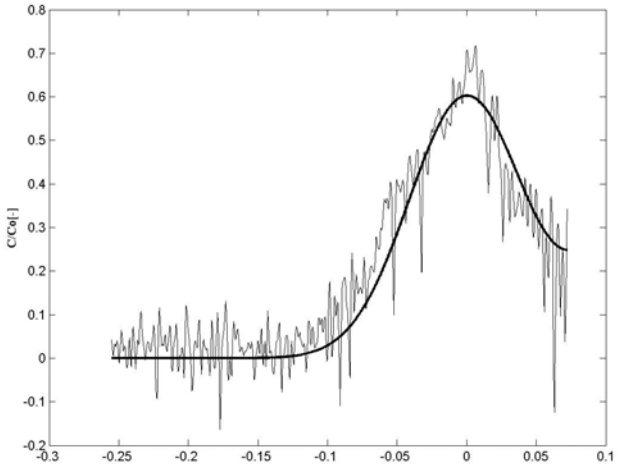

Figure 5. 7 Concentration profile 2.62m down gradient from the injection source

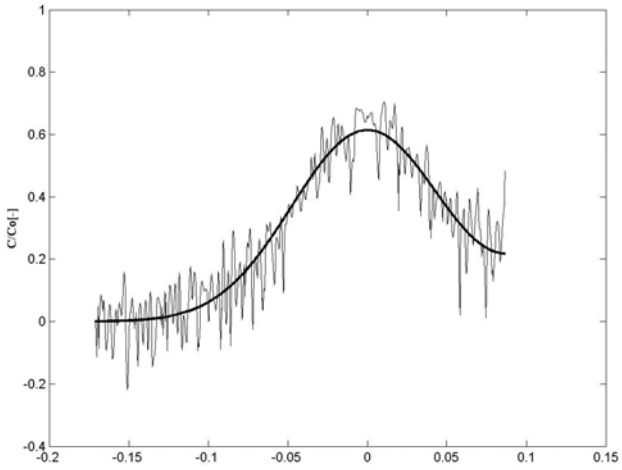

Figure 5. 8 Concentration profile 3.00m down gradient from the injection source

Table 5. **1** summarizes the parameters used to fit the experimental data. By analyzing six profiles (Figure 5. **3** to Figure 5. **8**), I determine the transverse dispersivity in the range of 1.6×10^{-4} to 2.89×10^{-4} m/s with the effective width ranging from 3.5 to 7.5 cm. The results agree with literature values (about 10% the mean diameter of sand), as I use coarse sand with 1.0-2.5 mm diameter.

The estimated transverse dispersivity α_T has an error < 5% for all vertical profiles, except the profile 0.05m down gradient, where it has a value of 8.9%. The high error of this profile is partly from the applied *Domenico's* model, which differs form the exact solution near the injection source. The effective injection source width can be determined very accu-

rately as it has an error smaller than 2%. The correlation coefficient of parameters are smaller than 0.65. This means the model parameters could be estimated jointly.

The uncertainty of measurement data ($\mathbf{C_{yy}}$ matrix) in each profile is rather small and the error can be thought as random error. This verifies the advantages of the non-invasive imaging method providing a large quantity of data with small errors.

By comparing the estimated parameters from different profiles, I obtain a small effective width corresponding to small transverse dispersivity in the profiles 1.09m and 1.74m. The underestimation of the parameters of these two profiles is obviously not due to the measurement errors. If the mean transverse dispersivity around 2.5×10^{-4} is correct, the error bar only gives a deviation around 10% (2.25×10^{-4} to 2.75×10^{-4} were the acceptable range). This indicates some systematic errors. Local heterogeneity is a possible explanation. For an illustration see Figure 5. **9**. In the middle part of the domain, there is a high hydraulic conductivity zone. The streamlines converge in the high conductivity zone, so that the concentration profile of a plume passing through that zone has a sharp fringe and is less widespread. As my model does not consider the change of hydraulic conductivity, it represents the converging plume as smaller values of h and α_T.

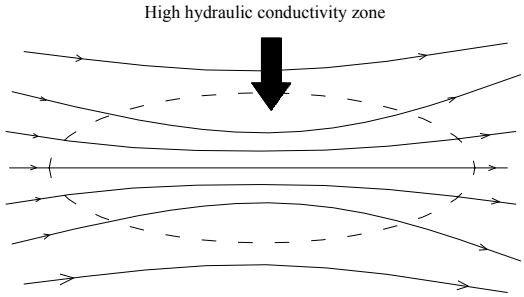

Figure 5. 9 Streamlines in a high hydraulic conductivity zone

Table 5. 1 Parameters estimating transverse dispersion

x	**0.05m**	**1.019m**	**1.74m**	**2.00m**	**2.62m**	**3.00m**
First moment (m)	0.1441	0.1964	0.22	0.218	0.255	0.2373
α ($\times 10^{-4}$ m) (fminsearch)	2.49	1.63	1.62	2.00	2.56	2.89
σ_a ($\times 10^{-4}$m) standard deviation	0.204	0.040	0.033	0.03	0.11	0.07
variance C_{yy} of color intensity (measurement error)	0.0077	0.0027	0.012	0.00077829	0.0061	0.0056
Coefficient of variation σ_a/α	8.19%	2.45%	2.04%	1.5%	4.30%	2.42%
Effective width *h* (m) (fminsearch)	0.074984	0.035179	0.038534	0.046561	0.0618	0.072148
σ_b standard deviation (m)	3.0×10^{-4}	3.134×10^{-4}	2.865×10^{-4}	2.593×10^{-4}	9.434×10^{-4}	6.359×10^{-4}
Coefficient of variance σ_b /*h*	0.40%	0.89%	0.74%	0.56%	1.53%	0.88%
Correlation coefficient of parameters	-0.0169	0.3914	0.6308	0.6416	0.344	0.339

*First moment indicate the shifting of the central line of the profile.

5.6. Reactive Tracer Test

I perform two sets of reactive-mixing experiments. I add thymolblue and methylred as pH indicators to both solutions. Details of the tracer solutions are described in chapter 3. Sufficient amount of NaOH and HNO3 was added to adjust the pH value. I inject the alkaline tracer solution by an injection well in the interior of the domain whereas the acidic solution is pumped to the inlet by a constant head tank. By adjusting the flow rate of two pumps, I achieved an injection-source width of 2.10cm and 4.50 cm for the two experiments. After injecting three pore volumes of tracer solutions to the aquifer, the plume reached steady state, I took digital photos and measured the length and the effective source width of the plume.

5.7. Conceptual and Mathematical Representation of Reactive Mixing

5.7.1. Steady-state Transport of Reactive Solutes

The closed-form solution to the steady-state transport equation of conservative solutes in a two-dimensional domain, neglecting dispersion, as already mentioned in equation (5.3) [Domenico and Robbins, 1985]:

$$c(x,y) = \frac{C_0}{2}\left(erf\left(\frac{y + b/2}{2}\sqrt{\frac{v}{D_T x}} \right) - erf\left(\frac{y - b/2}{2}\sqrt{\frac{v}{D_T x}} \right) \right) \tag{5. 7}$$

in which erf() is the error function. In the vertical profile, the concentration reaches the maximum along the centerline, y=0. Here, equation (5.7) simplifies to:

$$X(x,y_0) = \frac{c(x,y_0)}{c_0} = erf\left(\frac{b}{4\sqrt{x\,D_T/v}} \right) \tag{5. 8}$$

in which $X(x,y_0)$ is the normalized concentration. Thus, for a given injection height *b*, relative concentration c/c_0 at the centerline, and measured longitudinal distance x, or length *L*, we can determine the vertical, transverse dispersion coefficient D_T by:

$$D_T = \frac{v b^2}{16 L (inverf(X(L,y_0)))^2} \tag{5. 9}$$

in which inverf() is the inverse error function. Equation (5.9) makes clear that we can determine the transverse dispersion coefficient in a homogeneous porous medium from the length *L* of a plume with injection height *b* provided that we are able to detect a distinct relative concentration.

For a single solute, the relative concentration X is identical to the volumetric fraction of the solution, originating from the line source, in the mixture with the water from ambient flow.

Now we consider reactive systems in local equilibrium. The local equilibrium assumption is valid whenever the time scale of reaction is considerably smaller than the time scale of advective-dispersion transport. This is the case of most aqueous-phase acid/base reactions, but even field-scale microbial reactions are sometimes considered as equilibrium reactions because transport may be slow in comparison to the biological activity. The interaction with the solid phase cancels out in a steady-state transport. This implies that complex heterogeneous reactions, although present, do not influence the aqueous-phase concentration once the steady state has been approached.

For any aqueous-phase speciation, we can define quantities that do not change with the speciation, they are conservative. In geochemical codes, these quantities are commonly referred to a master species [*Appelo and Postma*, *1993*] . Typical conservative quantities are the total concentrations of the elements in a certain oxidation state, the alkalinity of a solution, or the charge of all ions corresponding to strong acids and bases. Given the master-species concentrations, the speciation of all compounds can be calculated. Since the master-species concentration are invariant with the aqueous-phase reaction, their transport can be calculated with the expressions for conservative compounds.

This brings us to applicability of Equations 5.8 and 5.9 to reactive system. I introduce a solution of reacting compounds by a line source into two-dimensional domain with parallel flow. The ambient solution has a different chemical composition. The two solutions mix due to transverse dispersion. Provided that all compounds under go essentially the same transverse dispersion, Equation 5.8 holds to estimate the volumetric fraction of the injected solution in the mixture along the centerline. All master species mix according to the volumetric fraction, resulting in a distribution of species according to distribution of master species concentration.

A particular application of this principle is to visualize the volume fraction of the injected solution by introducing a solution with a pH value different from that of the ambient water. Where the two solution mix by transverse dispersion, an intermediate pH will be established according to the buffer reactions of the solutes. Now, a particular color change marks a specific pH value which relates to a defined volumetric fraction X of the injected solution within the mixture. The latter information may be given by an independent titration experi-

ment. Measuring the length L of the pH indicator color plume, the seepage velocity v, and the injection width h, we can determine the transverse dispersion coefficient D_z by equation 5.9.

5.7.2. pH of a Mixture of Buffering Solutions

Consider a solution with low ionic strength containing a set of buffering compounds undergoing the buffer reaction $HBuf_i \leftrightarrow H^{\oplus} + Buf_i^{\theta}$ for each buffering compound i. All other ions, such as $Na^{\oplus}$ or Cl^{θ}, belong to strong acids and bases and do not change their charge in the pH range considered. Thus, at known pH and total buffer concentrations $[Buf_{tot,i}] = [HBuf_i] + [Buf_i^{\theta}]$. We can calculate the total charge of the remaining ions by:

$$\text{charge} = \frac{10^{-14}}{[H^{\oplus}]} + \sum_{i}^{n_{buf}} \frac{K_i [Buf_{tot,i}]}{K_i + [H^{\oplus}]} - [H^{\oplus}] \qquad \textbf{(5. 10)}$$

in which K_i is the equilibrium constant of the buffer reaction i. Equation (5.10) can easily be extended to account for multiple charged compounds.

We know consider an alkaline solution with total buffer concentrations $[Buf_{tot,i}]_{alk}$ and charge $_{alk}$, and an acidic solution with total buffer concentrations $[Buf_{tot,i}]_{ac}$ and $charge_{ac}$. When these two solutions mix, the charge and the total buffer concentrations mix linearly:

$$charge_{mix} = (1\text{-}X_{alk}) \times charge_{ac} + charge_{alk} \qquad \textbf{(5. 11)}$$

$$[Buf_{tot,i}]_{mix} = (1\text{-}X_{alk}) \times [Buf_{tot,i}]_{ac} + X_{alk} \times [Buf_{tot,i}]_{alk} \qquad \textbf{(5. 12)}$$

in which X_{alk} is the volumetric fraction of the alkaline solution in the mixture. Then, the pH of the mixture can be calculated by iterative solutions of:

$$[H^{\oplus}] = \frac{1}{2}\left(\sqrt{charge^2 + 4 \times \left(10^{-14} + \sum_{i}^{nbuf} \frac{K_i [H^{\oplus}][Buf_{tot,i}]}{[H^{\oplus}] + K_i}\right)} - charge\right) \qquad \textbf{(5. 13)}$$

using the charge and the total buffer concentrations of the mixture.

Equation (5.11) and (5.12) exemplify that the charge of the non-buffering ions as well as the total concentrations $[Buf_{tot,i}]$ of the buffering compounds are conservative quantities, even though we consider a reactive system.

It is well known, that the titration curve of a rather alkaline solution in a rather acidic one shows a rapid change of pH in a small range of the volumetric fraction X_{alk}. Adding small amount of a pH indicator, which must be a buffering compound, introduces a small step in the titration curve. Nonetheless, the color change of the indicator will mark a very distinct volumetric fraction X_{alk}.

5.8. Results

5.8.1. Titration Test

From the titration test , the pH as a function of the volumetric fraction of the alkaline solution X_{alk} is obtained. This curve is the basic quantification method, as described in section 5.7.2, in the mixing-controlled reactive transport experiment to determine how much alkaline solution is mixed with the acidic solution due to transverse dispersion at the mixing interface.

Figure 5. **10** shows the titration curve where experimental data are fitted with model data. Here, the measured data are fitted by the buffer model given in equation 5.13 with two buffering compounds, the first of which having a total concentration of $1.39\times10^{-4}\left(\pm1.43\times10^{-6}\right)$ mol/L and a pKa-value of $6.197\left(\pm0.022\right)$ and the second with total concentration $4.88\times10^{-4}\left(\pm4.54\times10^{-6}\right)$ mol/L and pKa $9.522\left(\pm0.021\right)$. The values in the brackets are the standard deviations of estimation, determined by the Levenberg-Marquardt optimization scheme. The estimated total concentration and pKa-value of the second buffer showed strong correlation, whereas all other parameters are mutually independent of each other. In Figure 5. **10**, the pH-values of 8.8, 5.2 and 4.5 and the corresponding volumetric fraction of the alkaline solution, 0.703, 0.562, 0.538, are highlighted by dashed lines. At these pH-values, the mixture of indicators changes color, and the corresponding X_{alk}-values are to be substituted into equation 5.9 in order to determine the transverse dispersion coefficient from the length and height of the reactive plume.

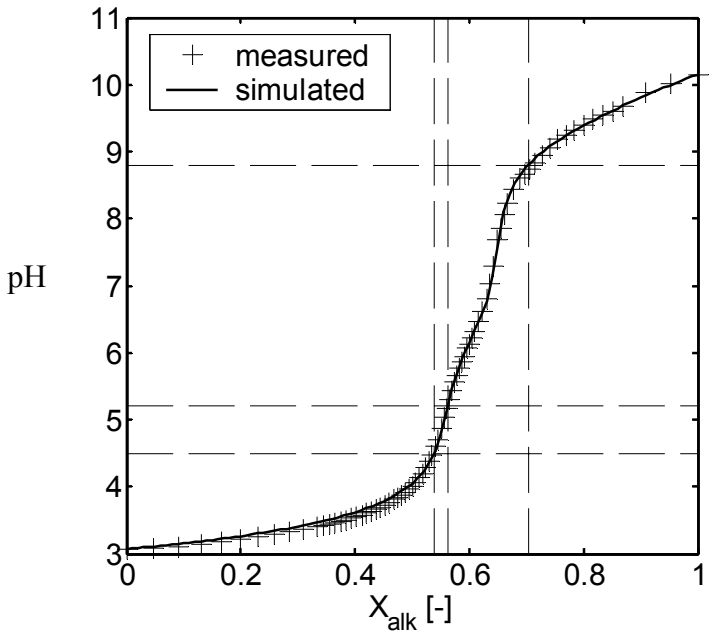

Figure 5. 10 Titration curve as a function of $X_{alkaline}$

5.8.2. Estimation of transverse dispersion coefficient from the plume length

Figure 5. **11** and Figure 5. **12** show the images of the alkaline plumes. The end of the alkaline plume, where the pH indicator in plume changes color from blue to yellow, indicates the pH value 8.8. The volumetric fraction of alkaline solution is determined in the independent titration experiment. The other two obvious color changes occur at pH 4.5 (dark red to light red) and at pH 5.2 (red to yellow). Hence, the length of the plume for these two pH-values are also measured. Table 5. **2** summarize the measured length of the plumes at three above mentioned pH valves of each experiment performed and the estimated transverse dispersion coefficient from the length and height of the plume by using eq. (5.9).

Figure 5. 11 Reactive-mixing plume with a 2.10 cm injection source width (experimental data)

Figure 5. 12 Reactive-mixing plume with a 4.50 cm injection source width (experimental data)

Table 5. 2 Estimated transverse dispersivity from the plume length

		Low injection rate	**High injection rate**
Injection rate		3.65 ml/min	6.2ml/min
Seepage velocity		2.08×10^{-5} m/s	2.32×10^{-5}m/s
Injection width		0.021m	0.045m
pH = 8.8 (X_{alk} = 0.703)	Alkaline plume length	0.202m	0.933m
	Calculated transverse dispersion coefficient	5.20×10^{-9} m²/s	5.79×10^{-9} m²/s
pH = 5.2 (X_{alk} = 0.562)	Neutral plume length	0.360 m	1.566 m
	Calculated transverse dispersion coefficient	5.30×10^{-9} m²/s	5.25×10^{-9} m²/s
H = 4.5 (X_{alk} = 0.539)	pH 4.5 acidic plume length	0.430m	1.846m
	Calculated transverse dispersion coefficient	4.91×10^{-9} m²/s	5.88×10^{-9} m²/s

The estimated transverse dispersion coefficient are in the range of 4.91×10^{-9} m²/s to 5.88×10^{-9} m²/s. The errors from two sets of experiment are within 8%, which indicates that the parameter can be accurately determined.

Comparing the estimated transverse dispersivities determined by the plume length corresponding to different color and X_{alk} in each experiment, I found consistent results with small uncertainty. This indicates that the titration curve determined in laboratory is valid under the conditions of the sandbox.

The results from the two experiments using different injection rate are quite similar. The difference in the results is mainly from data uncertainty. However, the D_T-value estimated by the high injection rate is slightly larger. As we can see in eq. (5.9), the contribution to the larger value of D_T is a smaller L_x or/and a larger b. While the length measurement is fairly accurate, the error in measurement of b will squarely influence D_T. Since the plume meandered, I first plot the centerline of the plume on the screen of sandbox and then measured the curve's length. The measurement errors might also come from measurement of the long curve in the high injection rate experiment.

The estimated transverse dispersivities as well as the measured injection width are applied in the analytical solution (equation 5.9). The resulting pH 8.8, 5.2 and 4.5 contour lines are plotted on the raw data. The contour lines fit quite well to the range of color changes. Since the plume meanders, the positions of contour lines are biased. But the length of the con-

tour line agrees with the one of the plume. Comparing the cross-section, the width of the contour line and the plume matches. The Figure 5. **13** and Figure 5. **14** illustrate the contour lines on the raw image.

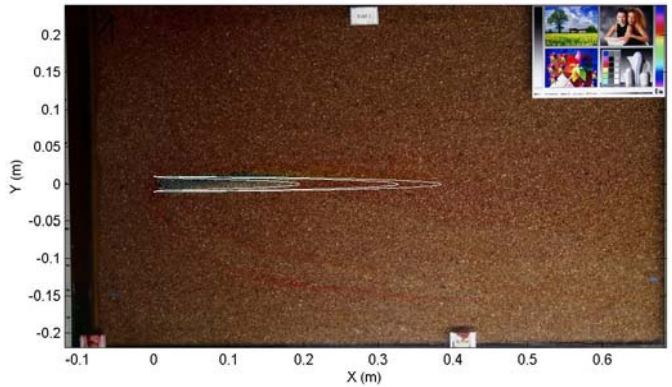

Figure 5. 13 Model contour lines of pH 8.8, 5.2, 4.5 on raw data (injection source width 0.21cm)

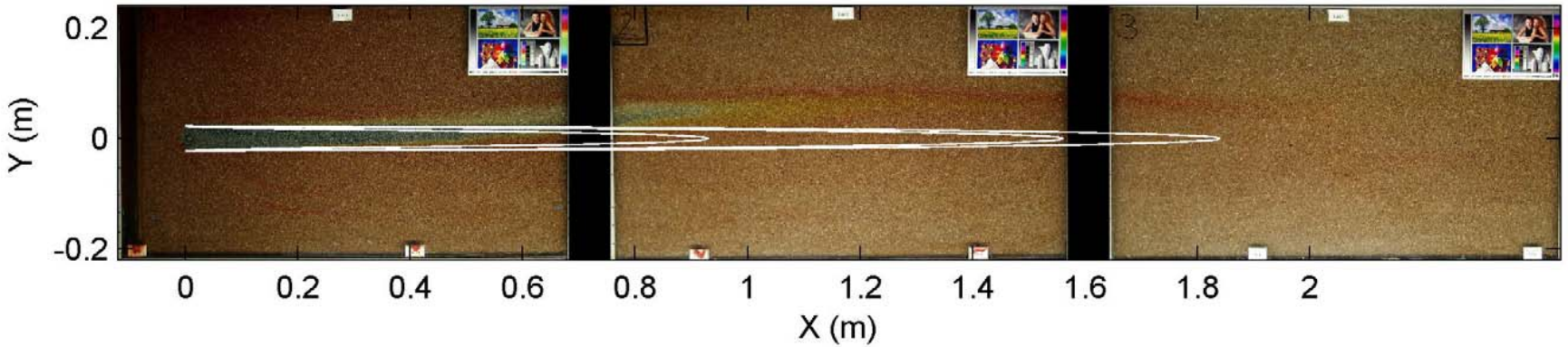

Figure 5. 14 Model contour lines of pH 8.8, 5.2, 4.5 on raw data (injection source width 0.450cm)

5.9. Discussions and Conclusion

Transverse mixing is visualized by a conservative-tracer and a mixing-controlled acid-base reaction. A non-invasive image method (digital images taken by digital camera) is used to capture the color intensity in the mixing domain.

By analyzing 6 vertical conservative concentration profiles and applying *Domenico's* approximate analytical solution to fit experimental data, I estimate transverse-dispersivity values in the range of 1.6×10^{-4} to 2.89×10^{-4} m/s with an effective width ranging from 3.5 to 7.5 cm. A simple equation (eqn.5.9) derived from Domenico's solution is used to estimate the transverse dispersivity from the reactive plume length and effective source width. The estimated transverse dispersivity from the two experiments are 2.31×10^{-4} m and 2.41×10^{-4} m, respectively. The result agrees with the literature value of about 10% of the mean grain diameter.

I use MATLAB to process the image data and perform model simulation. Image pixel values are transformed as $n_y \times n_x \times 3$ array. By matrix calculation, the image preprocessing, (shifting, rotation, color calibration and smoothing), color normalization can be realized.

Equation 5.9 is derived to determine the transverse dispersion coefficient. The only required measurement data are the injection source width h and the end length of the plume L_x The transverse dispersivity α_t is proportional to the square of effective injection source width h and inversely proportional to the plume end length Lx. Other parameters in this equation depended on the acid-base mixing ration, pH indicator properties and other factors.

The reaction between an acid and a base is simple, quick and reversible. Adding a small amount of pH indictor hardly has buffering effects. The pH value and the mixing ratio of the acid and base can be easily determined by titration experiment. If the concentrations of the acidic and the alkaline solutions and of the pH indicator do not change, the titration results are reproducible. This is a reliable experimental method.

A new non-invasive image technology tested is an innovative and accurate method. First, compared with other experimental methods, it does not need probes or sensors located in the domain. The setup is simple and the operation and control of the camera is easy. Second, this method does not disturb the flow or dispersion because the domain is not touched. Burying probes in the domain could not avoid slight changes of dispersion process. Third, the image technology can provide millions of pixel values as experimental data. Such a large quantity of data is not achieved in other methods. Take the conservative tracer profile as an

example. The average numbers of data points in one vertical profile is around 500-900. Incident errors are dramatically reduced. The error caused by the experiment in this case is within 8%. Image processing is an accurate method. Fourth, this method is not influenced by meandering of the tracer plume as it is not based on local point probes.

6. Transverse Mixing in Microscopically Heterogeneous Porous Media

6.1. Introduction

In this chapter, I study the role of micro-heterogeneity on transverse mixing. I discuss multiple reactive experiments, performed in a microscopically heterogeneous model aquifer with dimensions of 3.4m x 0.15m x 0.5m. The same sandbox has been used previously to develop a method for the determination of transverse dispersion for a reactive plume length for homogeneous steady-state flow condition [see chapter 5]. The sandbox was uniformly filled with two sand mixtures. However, the filling exhibited heterogeneities on the cm-scale. The microstructure resembles natural sedimentary structures such as laminations. This is in contrast to previous laboratory-scale studies on solute dispersion, where heterogeneities were created with definite sand lenses that themselves were as homogeneous as possible [*Ursino et al., 2001*, *Sillman & Zheng, 2001*, *Grathwohl et al., 2000*].

The main goal of the study is to deepen our understanding of vertical transverse dispersion and mixing in natural porous media. Especially, I want to test whether microscopic sedimentary structures enhance transverse vertical mixing. I applied the same reactive system as used in chapter 5, that is, I pump an alkaline tracer solution by a horizontal well into the domain while injecting an acidic tracer solution as ambient water, using constant head tanks. The two solutions are advected through the domain and mix due to transverse dispersion, leading to a distinct pH pattern. After the plume has reached steady state, I measure its length and the width at the source and take digital images.

6.2. Governing Equation

I use the same expression to estimate the transverse dispersion coefficient from the plume geometry as used in the homogeneous domain. This way, I determine apparent transverse dispersion coefficients, since Eq. (5.9) was derived for homogeneous conditions.

6.3. Experimental Section

6.3.1. Solutions Injected

In the experiments on the impact of micro-heterogeneities, I used thymol blue solely as pH indicator because methyl red, used in the homogeneous domain, sorbed onto the Quartz grains. The concentration of thymol blue was 0.04µg/L in both the acidic and alkaline solu-

tions. A sufficient amount of NaOH was added to adjust the pH in the alkaline solution to a value of 10, while HNO_3 (65%) was added to the acidic solution, leading to a pH of 3.

6.3.2. Reactive Tracer Tests

Two series of reactive experiments were carried out in the quasi two-dimensional, micro-heterogeneous model aquifer, using two different sand mixtures (grain size 0-3mm and 0.1-0.8mm, respectively) as filling materials. Each series contain two experiments with different seepage velocities. Details of the physical description of the model aquifers are described in chapter 3. The alkaline tracer solution was injected continuously into the model aquifer via a horizontal injection well, while the water of ambient flow was acidic. Table 6. 1 summarizes the sand types, injection rates of the tracer solution and seepage velocities used in the experiments. After injecting three pore volumes of tracer solutions to the aquifer, the plume reached steady state; I took digital photos and measured the length and the effective source width of the plume. The discharge rates and the pH in the inflow, within the domain and in the outflow were measured twice daily.

Table 6. 1 Injection rates and Seepage velocities used in the experiments

Experiment No.	Sand grain size (mm)	Tracer injection rate (ml/min)	Seepage velocity (m/s)
1	0-3mm	7.2	2.76×10^{-5}
2	0-3mm	2.9	1.65×10^{-5}
3	0.1-0.8mm	4.3	1.65×10^{-5}
4	0.1-0.8mm	2.4	1.10×10^{-5}

The end of the alkaline plume, where the pH indicator in plume changes color from blue to yellow, indicates the pKa value of 8.8, which corresponds to the volumetric fraction of alkaline solution in the mixture of 0.618. While the first two experiments were performed in the sand filling with grain sizes of 0-3mm, the other two were conducted in a rather fine sand mixture with grain sizes of 0.1-0.8mm. Figure 6. **1** and Figure 6. **2** show the photographs of the alkaline plumes developed in different reactive experiments. The center of the plume is blue, the fringes are yellow.

The transverse dispersion coefficient for each experiment was estimated by equation 5.9. The value of X_{alk} was 0.618 for the current system. Table 6. 2 shows the measured plume heights and lengths for the color changes, and the estimated transverse dispersion coefficients for different seepage velocities. The estimated transverse dispersion coefficient values ranged between 4.64×10^{-9}m2/s and 8.9×10^{-9}m²/s. The transverse dispersion coefficients were

higher for higher seepage velocities. The estimated dispersion coefficients are less than an order of magnitude higher than the effective diffusion coefficient.

In the experiments using the homogenously packed filling, the grain size was 1-2.5mm. Using a similar setup, the transverse dispersion coefficients obtained were 4.9×10^{-9}m²/s to 5.9×10^{-9}m²/s (See section 5.8).

Table 6. 2 Plume sizes and the estimated transverse dispersion coefficients.

Experiment No.	Seepage velocity (m/s)	Plume size (m)		Transverse Dispersion Coefficient (m²/s)
		Height	Length	
1.	2.76×10^{-5}	0.060	1.82	8.90×10^{-9}
2.	1.65×10^{-5}	0.040	0.50	8.60×10^{-9}
3.	1.65×10^{-5}	0.060	1.84	5.26×10^{-9}
4.	1.10×10^{-5}	0.050	0.97	4.64×10^{-9}

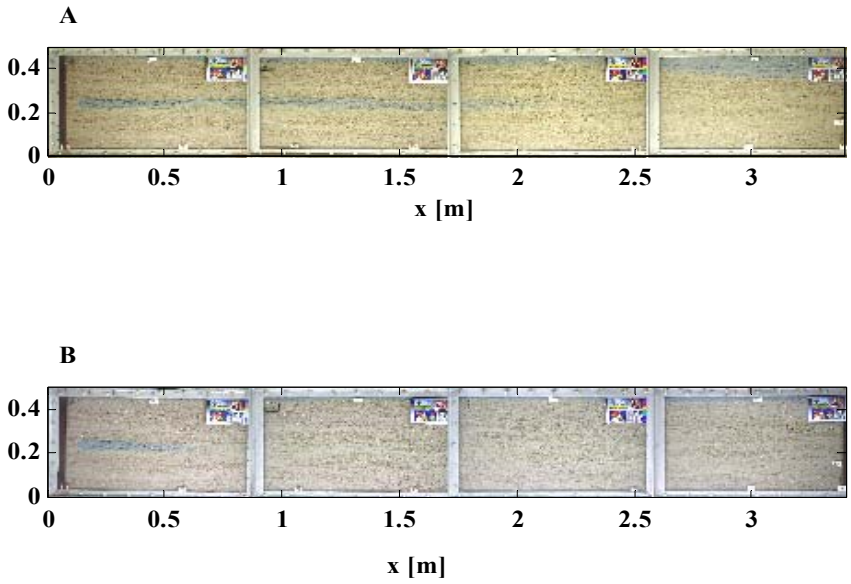

Figure 6. 1 Alkaline plume developed in the micro-heterogeneous model aquifer filled with the sand of size 0-3mm. A: seepage velocity of 2.76×10^{-5} m/s; B: seepage velocity of 1.65×10^{-5}m/s.

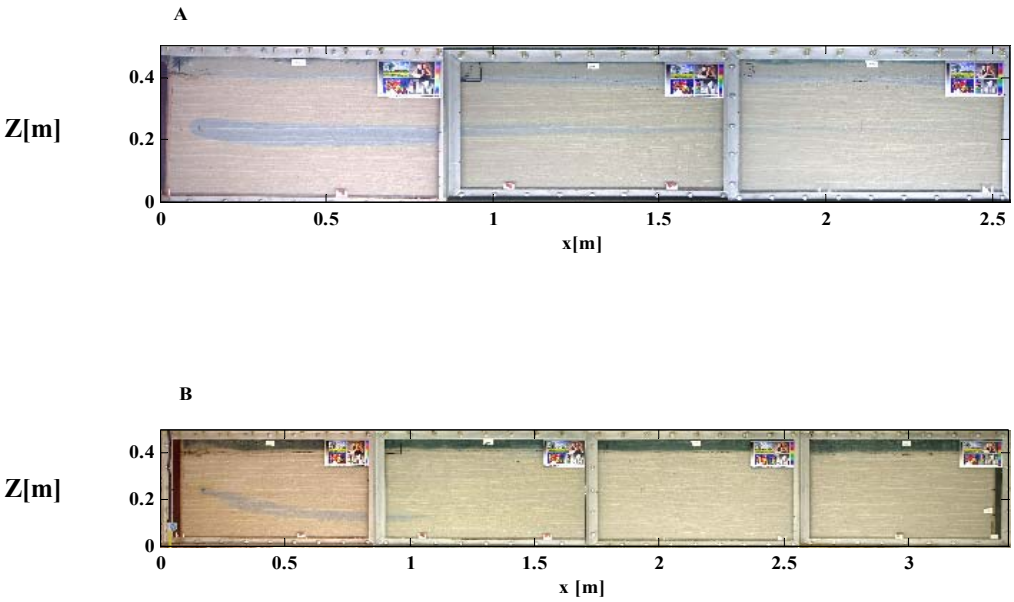

Figure 6. 2 Alkaline plume developed in the micro-heterogeneous model aquifer filled with the sand of size 0.1-0.8mm. A: seepage velocity of 1.65×10^{-5}m/s; B: seepage velocity of 1.1×10^{-5}m/s.

6.4. Conclusions

My experiments confirm that transverse dispersion coefficients are rather small. Using a filling exhibiting micro-heterogeneities, I obtained coefficients that are not larger than those found in homogeneous media. Therefore, I conclude that micro-heterogeneity has no major impact on transverse mixing. The estimated transverse coefficients are in the same order as the effective molecular diffusion coefficient. For typical groundwater flow velocities, therefore, the velocity-independent contribution to transverse dispersion cannot be ignored.

7. Transverse Mixing in Macroscopically Heterogeneous Porous Media

7.1. Introduction

Here, I describe tracer experiments on vertical transverse dispersion conducted in a quasi two-dimensional artificial model aquifer with dimensions 14m × 0.13m × 0.5m. The same sandbox has been used previously to analyze longitudinal mixing [*Jose, 2004*]. The sandbox is filled heterogeneously with four types of sand mixtures [chapter 3]. In contrast to previous large-scale laboratory studies on solute dispersion in heterogeneous media [*Silliman & Zheng*, *2001*; *Barth et al*., *2001*; *Ursino et al*., *2001*], I deliberately choose a filling that resembles natural sedimentary structures [*Pettijohn et al.*, *1987*]. In particular, the blocks of different sand types have the shapes of lenses rather than rectangles, and the blocks exhibit sedimentary micro-structures, such as laminations, created by filling the box in a settling procedure under water. Opting for closer-to-nature conditions, I sacrifice the exact knowledge about the hydraulic structure of the domain. While the authors of above cited studies tried to meet second-order statistics in order to test stochastic theory, I try to mimic natural sediments.

The main goal of the study is to deepen the understanding of vertical transverse dispersion and mixing in natural heterogeneous porous media. In particular, I want to test whether there is any significant enhancement of vertical transverse mixing due to the heterogeneity of the formation. For this purpose, I inject a dye tracer in the bottom half of the inflow boundary of the domain and measure the steady-state tracer distribution. A similar setup was used in homogeneous media for the determination of the transverse dispersion coefficient by *Grane & Gardner* [1961]. In contrast to homogeneous media, I must correct for plume meandering, not only because the boundary of the plume varies with distance but also because the transverse concentration profile is squeezed in high-velocity regions and stretched in low-velocity regions. Like *Ursino et al*. [2001], I use digital imaging to quantify the concentration distribution. For the correction related to plume meandering, I use simulated stream-function values applying the hydraulic-conductivity distribution determined from inverse modeling [*Nowak, 2004*].

7.2. Governing Equation

The solute transport equation (2.16) can be rewritten as follows:

$$\frac{\partial c}{\partial t} + \mathbf{v} \cdot \nabla c - \nabla \cdot \left(\mathbf{D} \nabla c \right) = 0 \tag{7. 1}$$

In two-dimensional, steady state flow with uniform flow-effective porosity θ_e [-], streamlines are oriented into the longitudinal direction, and potential lines in the transverse:

$$-\frac{q}{K} = \frac{\partial \Phi}{\partial x_\ell} \tag{7. 2}$$

$$q = \frac{\partial \Psi}{\partial x_t} \tag{7. 3}$$

in which x_t [L] is the remaining transverse coordinate. Φ [L] is the hydraulic head or pseudo-potential, and Ψ [L^2/T] is the value of the stream function.

Here, I consider a domain of a limited horizontal thickness W [L]. I neglect variability in the corresponding direction. The domain has a length L [L] and a height Δz [L]. The total discharge is denoted Q [L^3/T] and the total head-loss $\Delta\Phi$ [L]. Then, we may choose the following system of distorted spatial coordinates:

$$\xi(\mathbf{x}) = -\frac{L}{\Delta\Phi}\Phi(\mathbf{x}) \tag{7. 4}$$

$$\eta(\mathrm{x}) = \frac{\mathrm{W}\Delta\mathrm{z}}{\mathrm{Q}}\Psi(\mathrm{x}) \tag{7. 5}$$

In the system of transformed coordinates, the transport equation reads as:

$$\frac{\partial \mathrm{c}}{\partial \mathrm{t}} + \frac{\mathrm{L}}{\theta_\mathrm{e}\Delta\Phi}\frac{\mathrm{q}^2}{\mathrm{K}}\frac{\partial \mathrm{c}}{\partial \xi} - \frac{\mathrm{L}^2}{(\Delta\Phi)^2}\frac{\mathrm{q}}{\mathrm{K}}\frac{\partial}{\partial \xi}\left(\frac{\mathrm{D}_\ell \mathrm{q}}{\mathrm{K}}\frac{\partial \mathrm{c}}{\partial \xi}\right) - \frac{\mathrm{W}^2\Delta\mathrm{z}^2}{\mathrm{Q}^2}\mathrm{q}\frac{\partial}{\partial \eta}\left(\mathrm{D}_\mathrm{t}\mathrm{q}\frac{\partial \mathrm{c}}{\partial \eta}\right) = 0 \tag{7. 6}$$

The important difference between the original transport equation, Eq. (7.1), and the transformed one, Eq. (7.6), is that advection has become one-dimensional upon the transformation of coordinates. That is, effects of plume meandering have disappeared.

I now consider steady-state transport, so that the time-derivative in Eq. (7.6) vanishes. In the steady state, the longitudinal concentration gradients are typically very small, at least at a sufficient distance from injection points. Then, I can neglect longitudinal dispersion, and arrive at the following steady-state transport equation:

$$\frac{\partial \mathrm{c}}{\partial \xi} = \frac{\theta_\mathrm{e}\Delta\Phi\mathrm{W}^2\Delta\mathrm{z}^2}{\mathrm{LQ}^2}\frac{\mathrm{K}}{\mathrm{q}}\frac{\partial}{\partial \eta}\left(\mathrm{D}_\mathrm{t}\mathrm{q}\frac{\partial \mathrm{c}}{\partial \eta}\right) \tag{7. 7}$$

As boundary conditions, I assume no mass flux across the bounding streamlines, η = 0 and $\eta = W$, and a fixed concentration distribution at the inflow boundary, $\xi = 0$. In my experiments, I apply a step-like distribution:

$$\frac{\partial c}{\partial \eta} = 0 \text{ at } \eta = 0, \Delta z \tag{7. 8}$$

$$c(\xi = 0, \eta) = c_0 H(-\eta_b) \tag{7. 9}$$

in which c_0 is the inflow concentration, $H(\eta)$ is the Heaviside function and η_b [L] marks the lateral position of the plume boundary.

With varying coefficients of K, q, and D_t, no simple analytical solution of Eq. (7.9) exists. In my analysis, I thus determine an apparent transverse dispersion coefficient D_t^a [L^2/T], interpreting the concentration profile as if the coefficients were uniform:

$$\frac{\partial c}{\partial \xi} = \frac{\theta_e W \Delta z}{Q} D_t^a \frac{\partial^2 c}{\partial \eta^2} \tag{7. 10}$$

Accounting for the boundary conditions, Eqs. (7.8 & 7.9), and introducing the apparent transverse dispersivity $\alpha_t^a = \theta_e W \Delta z D_t^a / Q$ [L], the solution of Eqn. (7.10) is:

$$c(\xi, \eta) = \frac{c_0}{2}\left(1 - \sum_{i=-\infty}^{+\infty}\left(\mathbf{erf}\left(\frac{\eta - (2iW + \eta_b)}{2}\sqrt{\frac{1}{\alpha_t^a \xi}}\right) - \mathbf{erf}\left(\frac{\eta - (2(i+1)W - \eta_b)}{2}\sqrt{\frac{1}{\alpha_t^a \xi}}\right)\right)\right) \tag{7. 11}$$

in which the infinite series arises from the no-mass-flux boundary conditions, Eqn, (7.8). Since the transverse dispersivities are typically rather small, the series can be truncated to i ranging from -1 to +1.

In Section 6.3.2, I fit Eq. (7.11) to measured concentration profiles. I do this, using both the original Cartesian coordinates, x and z, and the transformed spatial coordinates, ξ and η, according to Eqs. (7.4 & 7.5). For the latter, I need the distribution of stream-function values, which I approximate from a calibrated numerical model. The main difference between the systems of coordinates is that ξ and η follow the iso-potential and streamlines whereas x_1 and z don't. In a low-velocity region, the streamlines diverge and the concentration profile is stretched laterally. Interpreting the concentration profile without knowing the velocity anomaly leads to high apparent transverse dispersion coefficients although transverse mixing, that is, the exchange between streamlines, may not be enhanced whatsoever. Conversely, the concentration profile is squeezed in high-velocity regions, which would be explained by small apparent transverse dispersion coefficients when using the original coordinates.

7.3. Experimental Description

7.3.1. Conservative Tracer Test

I use the food dye Cochineal Red A (E 124) as conservative tracer because it is toxicologically harmless and does neither degrade nor significantly adsorb to Quartz. 0.3 g/l of the tracer is dissolved into deionized-degassed water. I injected the tracer solution into the bottom inlet chamber, and a tracer-free solution into the separated top chamber. Cross-flow between the chambers was prevented by adjusting identical constant heads in both the chambers, thus guaranteeing the desired step-like concentration profile of the inflow concentration. I measured the discharge at the outflow twice daily.

Figure 7.1 shows a schematic diagram of the tracer test. In the course of the experiment, about five pore volumes of tracer solution were passed through the aquifer. The seepage velocity was approximately 7.6×10^{-5} m/s ≈ 6.6 m/d.

After the injection of about four pore volumes, the plume reached steady state. I took photos using the digital camera, stored the images on a computer, and later converted them to concentration data according to the procedure described in section 5.4. The red color of the tracer dye implies that the green and blue color channels have smaller values within the plume than outside. The red channel, by contrast, is hardly affected by the presence of the tracer. Thus, I use only the green and blue channels for the quantification of concentrations.

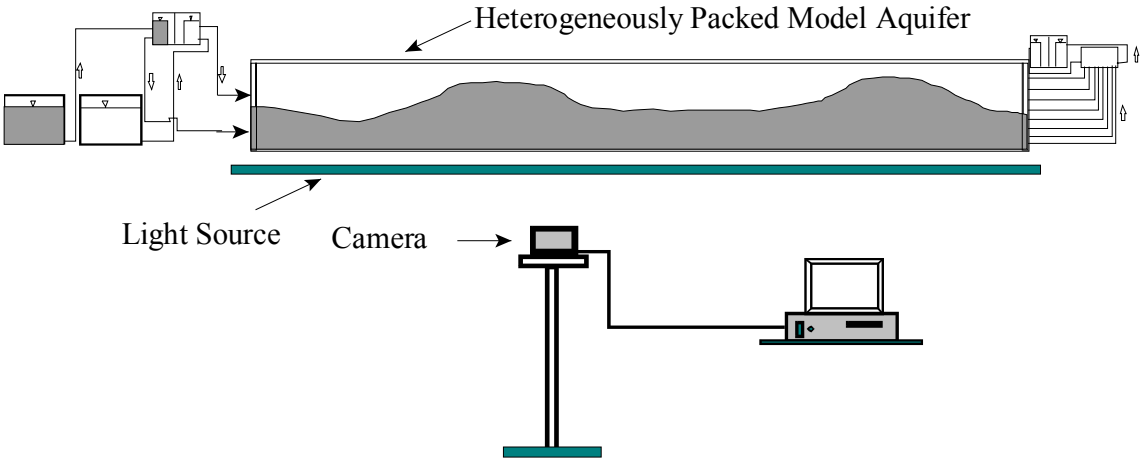

Figure 7. 1 Schematic setup of the tracer test

7.3.2. Correction for plume meandering

I analyze the transverse concentration profiles, obtained after image processing, in two ways. First, I use the original spatial coordinates, that is, the distance to the inlet x [L] and the vertical coordinate z [L], and interpret the transverse concentration profiles as if caused by steady-state advective-dispersive transport with uniform coefficients. For this purpose, I fit

the measured concentration at a certain distance x to the analytical expression of Eq. (7.11), replacing ξ by x and η by z. The fitting parameters are the vertical position z_b of the boundary line and the apparent transverse dispersivity α_t^a. The parameters obtained by the fitting procedure may be biased because advective transport is not oriented strictly in the x-direction, so that the transverse concentration profile is squeezed in high-velocity regions and stretched in low-velocity zones. At distances where the transverse fringe of the plume happens to be in a high-velocity region, the fit will determine a small value of α_t^a, whereas the fitted value will be large at distances where the fringe is in a low-velocity zone.

In order to correct for plume meandering, I need to transform the spatial coordinates according to Eqs. (7.4 & 7.5). This requires detailed knowledge about the flow field. Since there are no direct measurements of the velocity, we can only rely on results of inverse modeling. For this purpose, Nowak (2004) analyzed the temporal moments of 126 point-related breakthrough curves obtained in the experiment described by *Jose* [2004]. I use the inverse model by Nowak (2004) where he used 121 measurements of hydraulic head within the domain. He applied the quasi-linear approach of geostatistical inversing by *Kitanidis* [1995] with a modified Levenberg-Marquardt method for stabilization developed for his dissertation.

The primary result of the inverse model is a smooth distribution of the log-hydraulic conductivity. Simulations of flow and transport, using the estimated field, meet the data used for inversing within the prescribed measurement error. In the context of the present study, I use the field to approximate the distribution of the stream function $\Psi(\mathbf{x})$ within the domain. Particularly, I transform the vertical coordinate z to η according to Eqn. (7.5), while I keep the distance x to the inlet as longitudinal coordinate. Thus I fit η_b and α_t^a, so that Eqn. (7.11), using x rather than ξ, meets the measured vertical concentration profile for various values of the distance x to the inlet. If my estimate of the stream-line pattern was exact, the fitted value for the vertical position of the boundary line in transformed coordinates η_b would be identical in each profile.

7.3.3. Reactive Tracer Test

In addition to the conservative tracer test, I performed a test involving a reaction that was controlled by transverse mixing. I applied the same type of reactive system used as described in section 5.6. Reversing the flow field, I injected a solution with pH 10 in the middle of the inflow boundary over the height of 5cm. On top and underneath of that region, I in-

jected a solution with pH3. The two solutions were advected through the domain and mixed due to transverse dispersion, leading to a distinct pH pattern.

I added thymol blue as pH indicator to both solutions. Having a pKa-value of 8.5, thymol blue is yellowish under acidic to neutral conditions, and dark blue under alkaline conditions. Thus, the boundary of the blue color marks the contour line of pH 8.5. The concentration of thymol blue in the solutions is 0.04gm/l. I dissolved the tracer in deionized-degassed water and added sodium hydroxide or nitric acid to adjust the pH value.

From independent titration experiments, as described in section 5.8.1, I know that the point of color change refers to a relative concentration X_{alk} [-] of the alkaline solution in the mixture of 0.618% (Figure 7. **2**). I measure the length L [L] of the plume and estimate the apparent transverse α_t^a according to Eqn. 5.9.

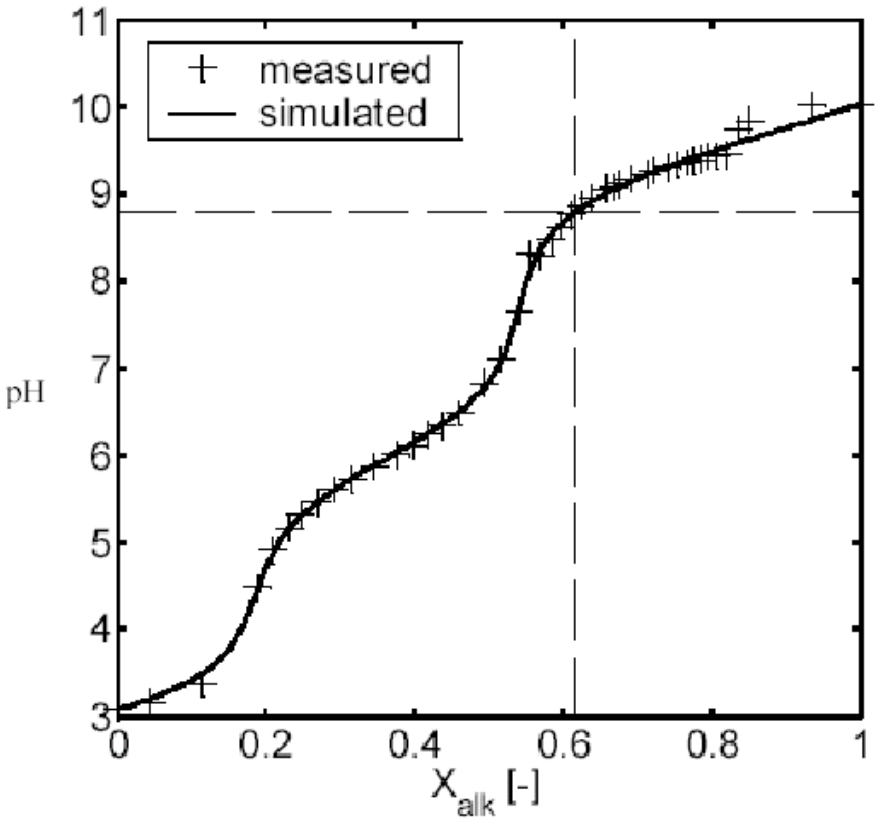

Figure 7. 2 Titration curve fitted with simulated curve

7.4. Results

7.4.1. Conservative Tracer Experiment

Figure 7. **3** shows the estimated log-conductivity field, the simulated flow net and the digital image of the conservative tracer in the model aquifer. The ratio of the largest to the smallest conductivity value is about 200. In the photo, the meandering of the plume boundary

is quite obvious. In the first two meters, the boundary remains in the middle of the box. Between distances of 2m and 3m, the boundary rises to a rather high position where it stays until about x=5m. Then it drops down and reaches its minimum at about x=7m. Around x=9m, the boundary meanders shortly upwards, comes down and rises to a high vertical position at $x \approx$ 10m. It stays there until $x \approx$ 12m and leaves the domain in a middle position.

The simulated flow field, shown also in Figure 7. **3**, follows essentially the same pattern, although not all features match exactly. In the first meter, the estimated conductivity field includes a high-conductivity zone in the upper half of the domain, focusing the flow. As a result, the simulation shows a significant dip of the boundary line between x=1m and x=2m. The real boundary, however, does not meander that strongly in this region. Also, the estimated high-conductivity lenses in the bottom half between $x \approx$ 7m and $x \approx$ 8m and at the very top at about x=12m appear slightly exaggerated, since the simulated meandering of the plume boundary is stronger than indicated by the photo. In this context, it may be worth noting that the inverse model relies mainly on the travel-time measurements presented by *Jose,* [2004]. The errors of the hydraulic-head measurements, which are also used in the inversing procedure, are rather large in comparison to the total head difference in the domain. Accurate measurements of the heads, however, are essential to accurately estimate the field of stream-function values, since streamlines and iso-potential lines are orthogonal to each other.

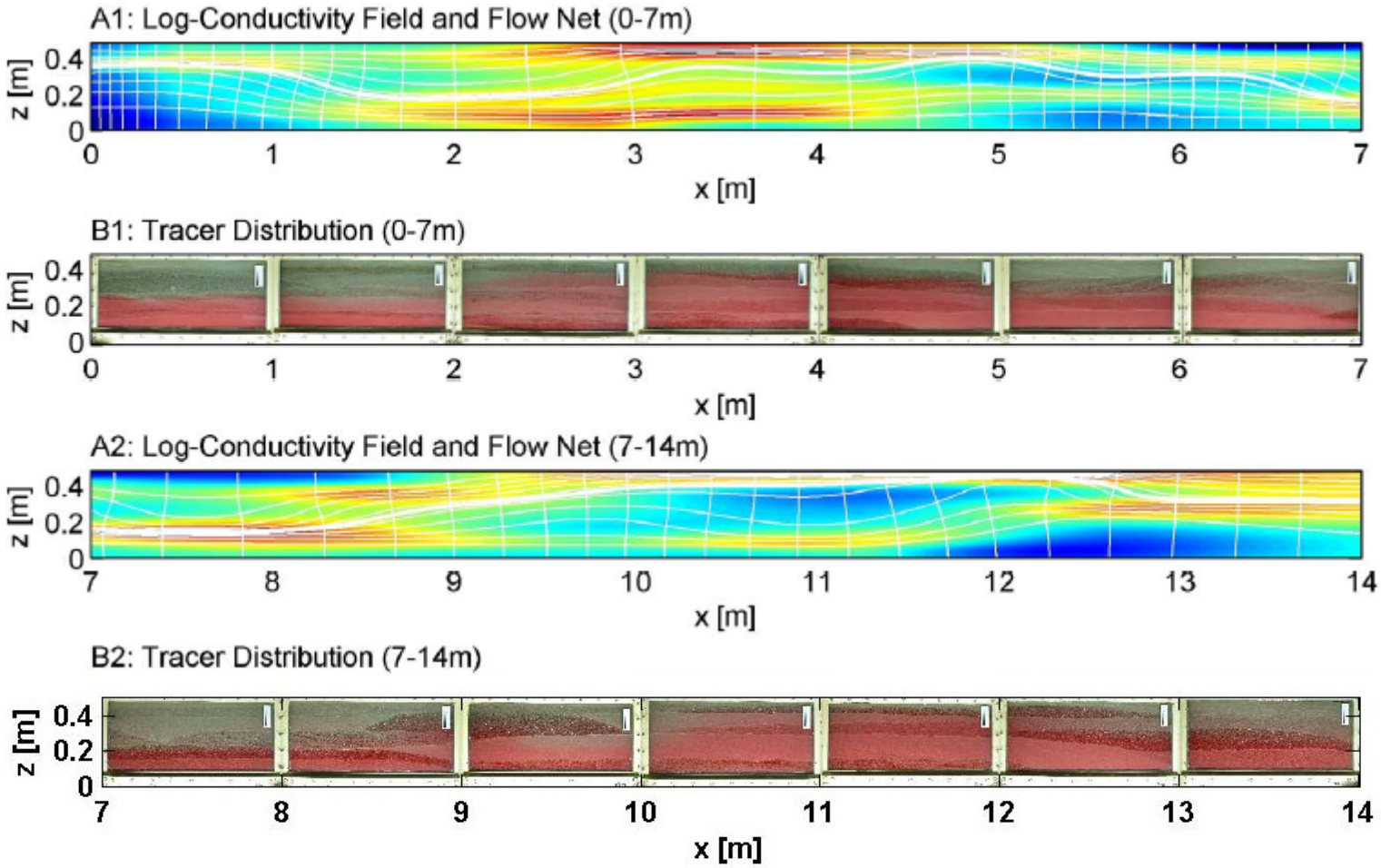

Figure 7. 3 Log-conductivity field, simulated flow net and measured distribution of the conservative tracer in the model aquifer. Bold streamline: centerline in transformed coordinates.

Figure 7. **4** shows the measured vertical concentration profile at x=5.20m and the corresponding model fit using Eqn. (7.11). The measured concentration profile is rather scattered which I attribute to the remaining spatial misalignment between the different images used in the analysis. Nonetheless, the high spatial resolution makes it possible to fit the analytical expression.

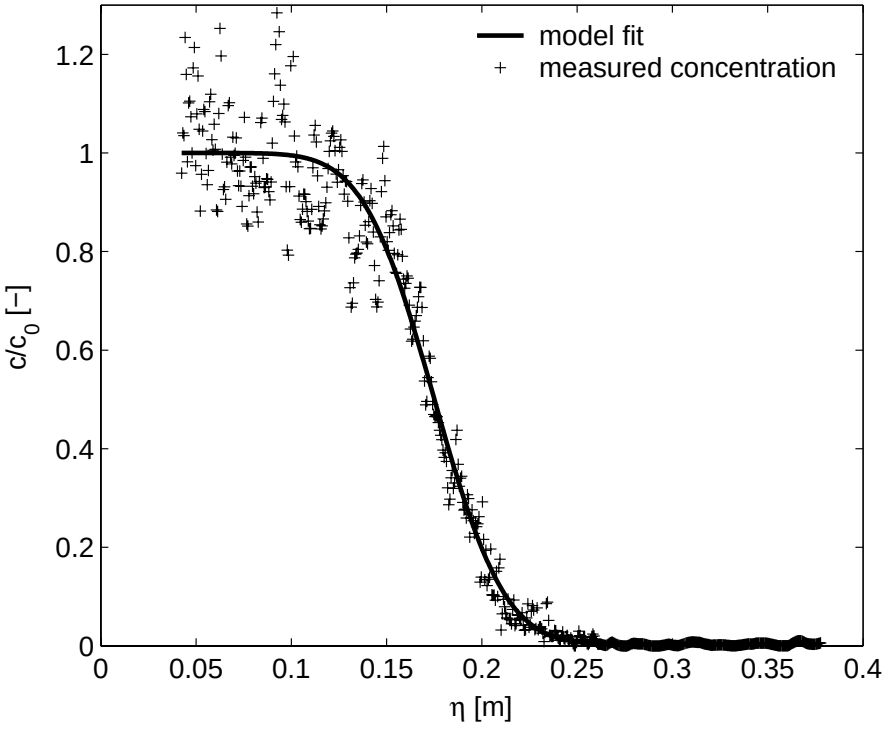

Figure 7. 4 Fit between Eqn. (7.11) and the measured vertical concentration profile at x =5.20 m

Figure 7. **5** shows the fitted apparent transverse dispersivity α_t^a and vertical position of the boundary line z_b, applying Eqn. (7.11) to the data with original spatial coordinates. The fitted values of z_b agree with the visual observation of the plume boundary discussed above, whereas the fitted values of α_t^a show a physically unreasonable distribution. At distances where the vertical position of the plume boundary has high values, the fitted apparent transverse dispersivities are very small. Between $x \approx$ 3.5m and $x \approx$ 5m, as well as between $x \approx$ 10m and $x \approx$ 11m, the fitted values of α_t^a are smaller than 1×10^{-4}m, and between $x \approx$ 11m and $x \approx$ 12m, they are even in the range of only 5×10^{-6}m. At $x \approx$ 2m, by contrast, the fitted transverse dispersivity is approximately 3×10^{-3}m. Intermediate values of about 3×10^{-4}m can be found, e.g., in the last two meters of the domain. The strong variations in the fitted dispersivities reflect the stretching and squeezing of the streamlines rather than enhanced and diminished transverse mixing. This becomes particularly clear in the region with the smallest fitted values

of α_t^a at $x \approx 11$m to $x \approx 12$m. Here, the boundary of the plume is far at the top of the domain ($z_b \approx 0.465$m). Obviously, this is a high-velocity region with very small distances between streamlines. Further downstream, the streamlines diverge and the transverse concentration profile is more spread out, resulting in higher values of the apparent transverse dispersivity α_t^a.

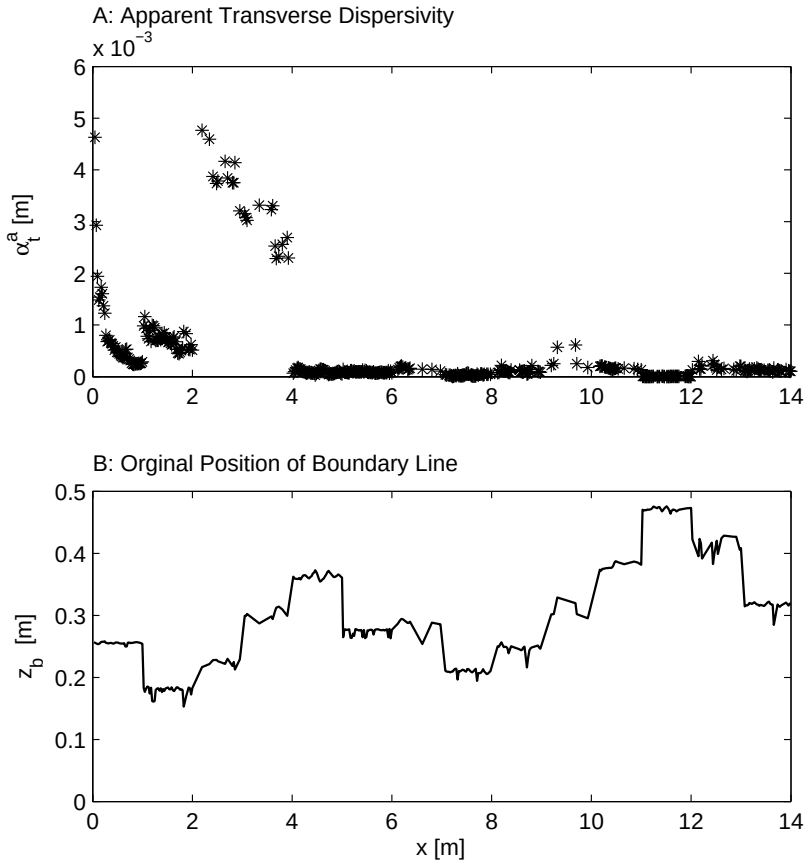

Figure 7. 5 Apparent transverse dispersivity α_t^a and vertical position z_b of the boundary line using the original spatial coordinates.

Figure 7. **6** shows the fitted apparent transverse dispersivity α_t^a and vertical position of the boundary line η_b, applying Eqn. (7.11) to the data after transforming the vertical coordinate according to Eqn. (7.5). If the estimated velocity field, used for the transformation, were exact, the fitted value of η_b would be constant. Obviously, this is not the case. As mentioned earlier, the estimated conductivity field shows a high-permeability lens in the first meter focusing the streamlines in the top half. Consequently, the initial η_b–values are rather small, whereas later on the values typically fluctuate about $\eta_b \approx 0.2$m. Wherever the plume meanders are the strongest, the fitted values of η_b vary, indicating that the proper length of high- or low-conductivity lenses is not estimated correctly by the inversing procedure. To-

wards the end of the domain, the fitted η_b–values tend again towards small numbers, which may be attributed to an overestimation of the high conductivity values in the top half at the end of the domain. Overall, however, the plume meandering is predicted rather well. While Figure 7. **5** shows very high values of the original vertical coordinate z_b of the boundary line, the fitted vertical coordinate η_b in transformed coordinates, shown in Figure 7. 6, never exceeds values of 0.3m.

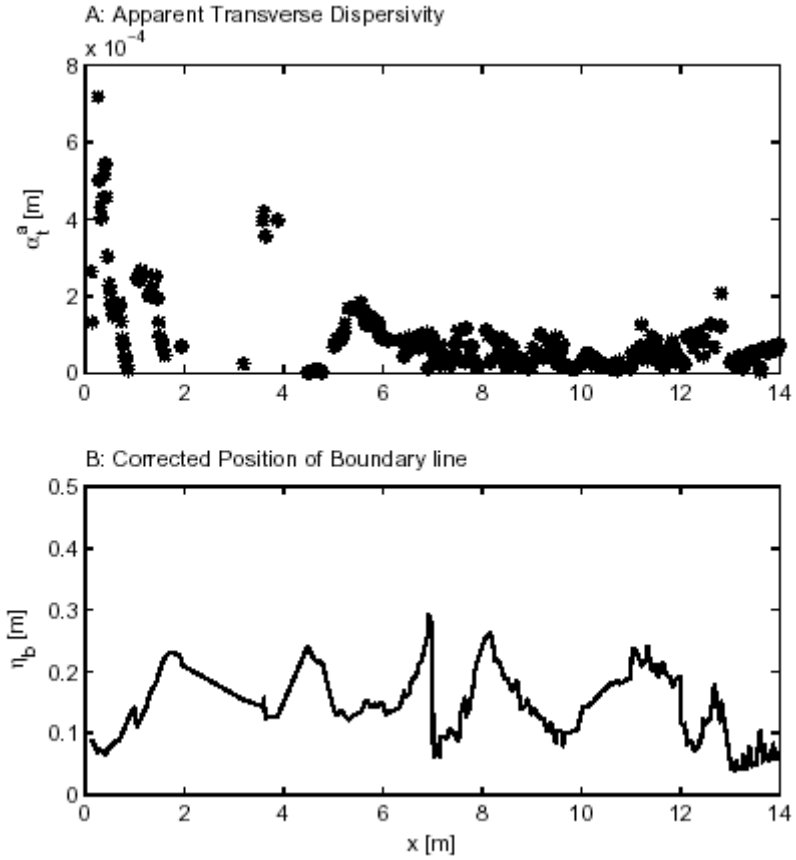

Figure 7. 6 Apparent transverse dispersivity α_t^a and vertical position η_b of the boundary line using the transformed spatial coordinates.

Figure 7. **6** also includes the fitted values of the apparent transverse dispersivity α_t^a, after transforming the coordinates. In general, these values fluctuate much less than those shown in Figure 7. **5**. In the first two meters, the estimated values of the apparent transverse dispersivity α_t^a are rather large due to the misrepresentation of stream lines in this region. For x>2m, the mean value of the fitted apparent transverse dispersivity α_t^a is 6.9×10^{-5} m, with a coefficient of variation of 75%. No definite trend with travel distance can be observed. Considering the mean seepage velocity of 7.6×10^{-5} m/s, the apparent transverse dispersion coeffi-

cient $D_t^a = v \times \alpha_t^a$ is 5.2×10^{-9} m^2/s, which is at most by a single order of magnitude larger than typical effective molecular diffusion coefficients.

7.4.2. Reactive tracer experiment

Figure 7. **7** shows the visualization of the reactive plume at the steady-state condition. Keep in mind that the flow field is reversed, the alkaline plume and the acidic ambient water are transported from right to left. Obviously, the plume meanders, expands and contracts according to the flow field. At x= 2.4m the plume spread out and remain thick until 4m. Compare to the conservative plume, it has followed the same pattern of meandering. Due to the meandering pattern of the plume, I consider the center path line of the plume for the measurement of the plume length and the measured plume length is about 7.65m and the measured height of the plume is 0.05m. The calculated apparent vertical transverse dispersivity α_t^a using Eq. (5.9) is 5.32×10^{-5}m where the mixing ratio of the alkaline solution was 0.618. Considering the mean seepage velocity of 6.41×10^{-5} m/s, and ignoring the effective diffusion coefficient the apparent transverse dispersion coefficient $D_t^a = v \times \alpha_t^a$ is 3.41×10^{-9} m^2/s which is less than an order of magnitude larger than typical effective molecular diffusion coefficients.

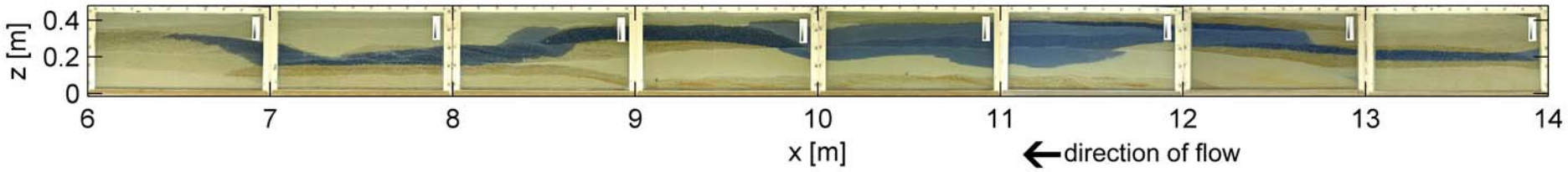

Figure 7. 7 Reactive tracer plume in the model aquifer, source width 0.05m and the measured length of the plume is 7.65m (Color of plume enhanced to obtain clearer optical impression).

7.5. Discussions and Conclusions

My experiments confirm that transverse vertical dispersion coefficients are fairly small. I have determined coefficients of approximately 5×10^{-9} m^2/s in a heterogeneously packed model aquifer of 14m length. These coefficients are not larger than those found in homogenous systems. Therefore, I conclude that heterogeneity has only a minor impact on vertical mixing. It does, however, cause significant vertical plume meandering. These findings are in agreement with stochastic theory predicting only a small increase in transverse vertical macrodispersion coefficients in the large-time limit [*Gelhar & Axness*, *1983*]. In stochastic theory, the plume meandering is expressed in enhanced transverse macrodispersion coefficients at intermediate times [*Dagan*, *1988*]. However, the corresponding time-dependent effective dispersion coefficient, which is more relevant to describe mixing, does typically not exceed the asymptotic macrodispersion coefficient [e.g., *Cirpka & Attinger*, *2003*]. Hence, small coefficients, as found in the experiment, were to be expected.

The limitation of vertical dispersive mixing can be of great practical relevance. The degradation of a wide and thin plume, originating from a continuously emitting source and reacting with compounds in the ambient water above and underneath the plume, may be controlled by vertical mixing [e.g., *Thornton et al.*, 2001]. I may estimate a characteristic vertical mixing width w [L] by $w=\sqrt{x\alpha_t^a}$. My domain is 14m long, resulting in a vertical mixing width w of 3.3cm. In order to reach a mixing width w of 10cm, a travel distance of ≈ 130m must be traversed. Thus, a plume, the degradation of which depends on vertical dispersive mixing, will become rather long.

In my experiments, I have used digital imaging techniques to quantify conservative-tracer concentrations. Like others [*Ursino et al.*, *2001*; *Huang et al.*, *2003*], I highly recommend this approach as a technique for the laboratory, because it allows for a spatial resolution that cannot be reached by sampling techniques. In field experiments, of course, glass panes are not available for optical observation. Here, optical sensors in direct-push rods may be suitable to obtain highly resolved vertical concentration profiles. However, my experiments also clearly show that concentration profiles alone are insufficient to quantify transverse mixing. Spatial variability of the velocity field yields a geometric distortion of the stream-line pattern. In order to express the probability that a solute particle changes streamlines, the distribution of stream lines and thus the velocity distribution needs to be known. Without such knowledge, interpreting vertical concentration profiles at an arbitrary point may lead to highly biased results. In my experimental domain, I could estimate the velocity field from previous

tracer studies and head measurements. Even there, the boundary line of the plume could not be predicted accurately throughout the domain. Under field conditions, such estimates are even more complicated, because the distribution of the streamlines needs to be approximated on a scale smaller than the vertical mixing width. It may thus be more feasible to estimate vertical mixing coefficients by analyzing reactive systems controlled by mixing rather than by analyzing concentration profiles of conservative tracers. My reactive-tracer experiment, where I estimate the transverse dispersion coefficient from the length and height of a reacting plume yields an estimate of the transverse dispersivity, which is consistent to the conservative-tracer data.

8. Summary and Conclusions

This thesis offers a promising approach to the characterization and quantification of transverse dispersion in heterogeneous porous media. The aim of the study is to deepen the understanding of transverse dispersion and mixing in natural heterogeneous porous media. Particularly, I verify experimentally if there is any enhancement of transverse mixing in natural heterogeneous porous media.

I perform experiments in three different dimensions to achieve the goal of the study. First, I develop method for the determination of pore-scale transverse dispersivity by Taylor-Aris-dispersion theory as suggested by *Cirpka and Kitanidis* [2001b] by performing experiments in helical column. Second, I develop a non-invasive imaging method for the determination of transverse dispersion coefficient in porous media at the laboratory scale. I design a laboratory scale quasi two-dimensional model aquifer and pack it homogeneously by silica sand. I conduct the conservative and reactive tracer tests. Third, I quantify the impact of microheterogeneity on transverse mixing in porous media by different silica sand type mixtures in such a way that homogeneous and heterogeneous porous media are formed. Here, I apply an imaging technique to perform several reactive tracer tests to quantify the effect of microheterogeneity. Fourth, I quantify vertical mixing in heterogeneous porous media by performing the conservative and the reactive tracer tests in the technical scale heterogeneous model aquifer. Hence, I design a technical scale quasi two-dimensional model aquifer and fill it with different silica sand types to create both macroscopic and microscopic sedimentary structures resembling natural sedimentary structures.

The result of tracer experiments using the helical soil column shows fairly high values of local transverse dispersivity (6.57×10^{-4} m) as the original analysis by *Cirpka and Kitanidis*,[2001b] did not account for the effects of the pitch, which causes secondary flow exchanging mass in the radial direction. The optimization approach developed by *Benekos* [2004] for determining the transverse dispersivity coupled with the numerical simulation of the transport in the helix reveals that the secondary flow needs to be considered. The secondary flow depends entirely on the hydraulic gradient and the helix characteristics whereas the transverse dispersivity is a property of the porous medium and its geometry. Particle-tracking simulations show that neglecting the secondary flow may result in significant differences in determining the rate of increase of the second central moment, which describes the spread of

the breakthrough curve. A comparison between the Levenberg-Marquardt optimization based on particle tracking considering the secondary motion and the regression technique neglecting secondary motion shows smaller values of α_t when accounting for the secondary motion. However, the differences are not overwhelmingly large for this particular configuration and the considered flow regime.

In chapter 5, a digital imaging techniques is developed to quantify the transverse dispersion coefficient in porous media. The method is shown to be a simple and accurate one to investigate dispersive mixing in porous media. The approach as a technique for the laboratory is advantageous because of its high spatial resolution that cannot be reached by sampling techniques. Optical sensors in direct-push rods may be suitable to obtain highly resolved vertical concentration profiles in the field. The equipment is of lower cost compared with other non-invasive techniques, such as tomography or NMR. To assure accurate measurements by using this techniques, one should try to decrease the geometric misrepresentation by keeping the camera in a fixed position during the course of the experiment to match on a pixel by pixel basis of identical objects of two images, taken at different times. By conducting reactive tracer experiments, I show the applicability of the approach by injecting alkaline plumes into acidic ambient water, in which the length of the plumes is measured by observing the color change of standard pH indicators.

To quantify the impact of microheterogeneity on transverse mixing, I conduct two series of experiments packed by two different sand mixtures, which resemble microscopic sedimentary structures on the cm-scale. Here, I apply the reactive approach developed in chapter 5. The estimated transverse dispersion coefficients are in the range of 4.6×10^{-9} m²/s to 8.9×10^{-9} m²/s that are at less than an order of magnitude higher than an effective diffusion coefficient. No significant increase of the vertical transverse dispersion coefficient is observed compared to those found in the homogenous system, indicating that the microscopic heterogeneity has only a minor impact on vertical transverse dispersion.

For the quantification of the impact of macroheterogeneity, I performed conservative and reactive experiments in the technical-scale model aquifer. The result of conservative tracer experiments shows that interpreting the transverse concentration profiles in heterogeneous porous media as if caused by steady-state advective-dispersion transport with uniform coefficient parameters show higher values at distances where the plume fringes are in low velocity zones whereas lower values at distances where fringes are in high velocity zones. These higher or lower values of transverse dispersivities result from the plume meandering caused by heterogeneity, which in fact, does not reflect increase and decrease of transverse

mixing. But, using the transformed vertical spatial coordinates i.e. applying the knowledge of velocity distribution gives more consistent and accurate results. The latter shows good agreement with results from reactive tracer experiments.

The estimated transverse dispersion coefficients are not larger than those found in homogenous systems. Therefore, I conclude that heterogeneity has only minor impact on vertical mixing. But it does cause significant vertical plume meandering. These results, in fact, are in good agreement with stochastic theory given by *Gelhar and Axness*, 1983, predicting only a small increase in transverse vertical macrodispersion coefficients at large times.

My experiments confirm that concentration profiles alone are insufficient to quantify transverse mixing in heterogeneous media. Without knowledge about the velocity distribution within the domain, it is not possible to determine meaningful vertical dispersion coefficients from the concentration profiles. Under field conditions, the uncertainty of the velocity distribution is much higher and more complex than that in the well controlled laboratory experiments. Indeed, it may be more reasonable to estimate vertical mixing coefficients by analyzing reactive systems controlled by mixing instead of analyzing concentration profiles of conservative tracers.

9. References

Anderson, M. P., (1992): Applied Groundwater Modeling: Simulation of Flow and Advective Transport, Academic Press, New York.

Appelo, C.A.J.; D. Postma, (1993): Geochemistry, groundwater and pollution, Rotterdam.

Aris, R., (1956): On the dispersion of a solute in a fluid flowing through a tube, Proc. R. Soc. London, Ser. A, 235, 67–77.

Attinger, S., M. Dentz, H. Kinzelbach, and W. Kinzelbach (1999): Temporal behavior of a solute cloud in a chemically heterogeneous porous medium. Journal of Fluid Mechanics, 386, 77-104.

Barth, G.R., T.H. Illangasekare, M.C. Hill, and H. Rajaram (2001): Predictive modeling of flow and transport in a two-dimensional intermediate-scale: heterogeneous porous medium, Water Resources. Res., 37(10), 2503-2512.

Bates, D. M., and D. G. Watts (1981): A Relative Offset Orthogonality Convergence Criterion for Nonlinear Least Squares, 23(2), 179-183.

Bear, J, and D. K. Todd (1960): The transition zone between fresh and salt waters in costal aquifers, University of California, Water Resources Centre Contribution. No. 29.

Bear, J.(1972): Dynamics of Fluids in Porous Media, Elsevier Science, New York.

Bello, M. S., R. Rezzonico, and P.G. Righetti (1994): Use of Taylor-Aris dispersion for measurement of a solute diffusion coefficient in thin capillaries, Sciences, 266(5186), 773-776, 1994.

Belongia, B. M., and J. C. Baygents (1997): Measurements on the diffusion coefficient of colloidal particles by Traylor –Aris dispersion, J. Colloid Interface Science, 195(1), 19-31.

Benekos, I., (2004): Experimental determination of transverse dispersion parameters. Tracer experiments and numerical simulations in a helix and a cochlea, Unpublished PhD dissertation, Department of Civil and Environmental Engineering, Stanford University, USA.

Blackwell, R.J.(1962): Laboratory studies of Microscopic dispersion Phenomena, Society of Petroleum Engineers Journal, pp.69-76.

Brenner, H., (1980): A general Theory of Taylor Dispersion Phenomena, Physicochemical Hydrodynamics, 1, 91-123.

Brooks, A. N. and T. J. R. Hughes (1982): Streamline upwind/Petrov-Galerkin formulations for convection dominated flows with particular emphasis on the incompressible Navier-Stokes equations, Computational Methods in Applied Mechanical Engineering, 32(1-3), 199-259.

Bruch, J. C.(1970): Two-Dimensional Dispersion Experiments in a porous medium, Water Resources Research, vol. 6, no. 3, pp.791-800.

Carman, P. (1937): Fluid flow though a granular bed, Trans. Inst. Chem. Eng. London 15: 150– 156.

Chen, J. S., C. S. Chen, H. S. Gau, and C. W. Liu (1999): A two-well method to evaluate transverse dispersivity for tracer tests in a radially convergent flow field, Journal of Hydrology, 223(3-4), 175-197.

Cirpka, O.A., E.O. Frind, R. Helmig (1999), Numerical simulation of biodegradation controlled by transverse mixing, J. Contam. Hydrol., 40(2), 159-182.

Cirpka, O.A., and P. K. Kitanidis (2000a): Characterization of mixing and dilution in heterogeneous aquifers by means of local temporal moments. Water Resources Res., 36(5), 1221-1236.

Cirpka, O. A., & P. K. Kitanidis (2000b): An advective-dispersive stream tube approach for the transfer of conservative-tracer data to reactive transport, Water Resources Res., 36(5), 1209-1220.

Cirpka, O. A. & P. K. Kitanidis (2001a): Travel-time based model of bioremediation using circulation wells, Ground Water 39(3): 422–432.

Cirpka, O.A., and P. K. Kitanidis (2001b): Theoretical Basis for the Measurement of Local Transverse Dispersion in Isotropic Porous Media. Water Resources Research, 37(2), 243-252.

Cirpka, O.A. (2002): Choice of dispersion coefficients in reactive transport calculations on smoothened fields, J. Contam. Hydrol., 58(3-4), 261-282.

Dagan, G. (1984): Solute transport in heterogeneous porous formations. Journal of Fluid Mechanics, 145, 151-177.

Dagan, G. (1988), Time-dependent macrodispersion for solute transport in anisotropic heterogeneous aquifers, Water Resources. Res., 24(9), 1491-1500.

Dagan, G. (1990): Transport in heterogeneous porous formations: Spatial moments, ergodicity, and effective dispersion, Water Resources. Res. 26: 1281–1290.

Dagan, G. and S.P. Neuman (Editors) (1997): Subsurface flow and transport: A stochastic approach. International hydrology Series. Cambridge University Press, Cambridge, 241pp.

Dagan, G., and A. Fiori (1997): The influence of pore-scale dispersion on concentration statistical moments in transport through heterogeneous aquifers. Water Resources Res., 33(7), 1595-1605.

Dagan, G., V.D. Cvetkovic, A. Shapiro (1992): A solute flux approach in transport in heterogeneous formations. Water Resources Res., 28(5), 1369-1376.

Dentz, M., H. Kinzelbach, S. Attinger, and W. Kinzelbach (2000a):Temporal behavior of solute cloud in a heterogeneous porous medium:1. Point like injection. Water Resources Res., 36(12), 3591-3604.

Dentz, M., H. Kinzelbach, S. Attinger, and W. Kinzelbach (2000b):Temporal behavior of solute cloud in a heterogeneous porous medium:2. Spatially extended injection. Water Resources Res., 36(12), 3605-3614.

Dentz, M., H. Kinzelbach, S. Attinger, and W. Kinzelbach (2002):Temporal behavior of solute cloud in a heterogeneous porous medium:3. Numerical simulation. Water Resources Res., 38(7), 23-1-13.

Deutsch, C. V. & A. G. Journel (1992): GSLIB: Geostatistical software library and user's guide, Oxford University Press, New York.

Domenico, P.A. and G.A. Robbins (1985): A new method of contaminant plume Analysis. Groundwater, 23(4): 476-485.

Dybas, M. J., M. Barcelona, S. Bezborodnikov, S. Davies, L. Forney, H. Heuer, O. Kawka, T. Mayotte, T., L. Sep´ulveda-Torres, K. Smalla, M. Sneathen, J. Tiedje, T. Voice, D.C. Wiggert, M.E. Witt & C.S. Criddle (1998). Pilot-scale evaluation of bioaugmentation for in-situ

remediation of a carbon tetrachloride-contaminated aquifer, Environ. Sci. Technol. 32(22): 3598–3611.

Eberhardt, C. and P. Grathwohl (2000): Dissolution Kinetics of BTEX and PAHS from creosote pools and smear zones monitored in well controlled large scale laboratory experiments. In Rosbjerg et al., (eds.), Groundwater Research, Rotterdam: Belkema.

Fetter, C.W. (1993): Contaminant hydrology. Prentice-Hall, Inc., London.

Fetter, C.W. (1994): Applied Hydrogeology.3rd ed. Prentice-Hall, Inc.

Fiori, A. (1996). Finite peclet extensions of dagan's solutions to transport in anisotropic heterogeneous formations, Water Resources. Res. 32: 193–198.

Fiori, A., & G. Dagan (2000): Concentration fluctuations in aquifer transport: a rigorous first order solution and applications, Contaminant Hydro., 45, 139-136,

Fiori, A., and G. Dagan, (1999): Concentration fluctuations in transport by groundwater: Comparison between theory and field experiments, Water Resour. Res., 35(1), 105-112,

Freeze, R. A. & J. A. Cherry (1979): Groundwater, Prentice-Hall.Inc.

Gelhar, L. W. and C. Welty, and K.R. Rehfeldt (1992): A critical review of data on field scale dispersion in aquifers, Water Resources. Res., 28(7), 1955-1974.

Gelhar, L.W. (1993): Stochastic subsurface hydrology. Prentice-Hall, Englewood Cliffs, New Jersey, 390pp.

Gelhar, L.W., A.L. Gutjahr, and R.L. Naff (1979): Stochastic analysis of macrodispersion in a stratified aquifer, Water Resour. Res., 15(6), 1387-1397.

Gelhar, L.W., and C.L. Axness (1983), Three dimensional stochastic analysis of macrodispersion in aquifers, Water Resources. Res., 19(1), 161-180.

Ginn, T. R. (2001). Stochastic-convective transport with nonlinear reactions and mixing: finite streamtube ensemble formulation for multicomponent reaction systems with intrastreamtube dispersion, J. Contam. Hydrol. 47(1-2): 1–28.

Ginn, T. R., C. S. Simmons, and B. D. Wood (1995): Stochastic-convective transport with nonlinear reaction: Biodegradation with microbial growth, Water Resources. Res., 31(11), 2689-2700.

Grane, F. E., and G.H.F. Gardner (1961), Measurements of transverse dispersion in granular media, J. Chem. Eng. Data, 6(2), 283-287.

Grathwohl, P. (1998). Diffusion in Natural Porous Media: Contaminant Transport, Sorption, Desorption and Dissolution Kinetics. Kluwer Academics publishers, Boston.

Grathwohl, P., I.D. Klenk, C. Eberhardt, and U. Maier (2000): Steady state plumes: mechanisms of transverse mixing in aquifers. Contaminated Site Remediation Conference, Australia, Melbourne.

Hantush, M. M., and M.A. Marino, (1998): Interlayer diffusive transfer and transport of contaminants in stratified formation: I. Theory. Journal of Hydrol. Eng. 3 (4), 232-240.

Harleman, D.R.F. and R.R. Rumer (1963): Longitudinal and lateral dispersion in an isotropic porous media. Fluid Mechanics: 385-394.

Hassinger, R. C. and D.U. von Rosenberg (1968): A Mathematical and Experimental Examination of Transverse Dispersion Coefficient, Society of Petroleum Engineers Journal, June 1968, pp. 195-204

Huang, W.E., C.C. Smith, D.N. Lerner, S. F. Thornton, A. Oram (2002): Physical Modelling of solute transport in porous media: evaluation of an imaging technique using UV excited fluorescent dye, Water Research, 36, 1843- 1853.

Huang, W.E., S. E. Oswald, D.N. Lerner, C.C. Smith, and C. Zheng (2003): Dissolved oxygen imaging in a porous medium to investigate biodegradation in a plume with limited electron acceptor supply, Environ. Sci. Technol., 37(9), 1905 - 1911

Indelman, P. & Y. Rubin (1995): Flow in heterogeneous media displaying a linear trend in the log conductivity, Water Resources Res. 31(5): 1257–1265.

Isaaks, E. H. & R.M. Srivastava (1988): Spatial continuity measures for probabilistic and deterministic geostatistics, Math. Geol. 20(4): 313–341.

Jiao, J. J.(1993:)Data-Analyses Methods for Determining Two-Dimensional Dispersive Parameters, Groundwater, 31(1), 57-62.

Jose, S.C. (2004): Experimental Investigation on longitudinal dispersive mixing in heterogeneous aquifers. Doctoral thesis, University of Stuttgart, Germany.

Journal, A. and C. Huijbregts (1978): Mining Geostatistics. Academic Press New York, 590pp.

Kapoor, V., and P. K. Kitanidis (1996): Concentration fluctuations and dilution in two-dimensionally periodic heterogeneous porous media, Transport in Porous Media, 22, 91-119.

Kapoor, V., and P.K. Kitanidis (1998): Concentration fluctuations and dilution in aquifers, Water Resources. Res., 34(5), 1181-1193.

Kapoor, V., L. W. Gelhar, and F. Miralles-Wilhelm (1997): Bimolecular second order reactions in spatially varying flows: Segregation induced scale-dependent transformation rates, Water Resources. Res., 33(4), 527-536.

Kapoor, V., L.W. Gelhar, and F. Miralles-Wilhelm (1997): Bimolecular second order reactions in spatially varying flows: Segregation induced scale-dependent transformation rates, Water Resources Res., 33(4), 527-536.

Kasnavia, T., De Vu, and D. A. Sabatini (1999): Fluorescent Dye and Media Properties Affecting Sorption and Tracer Selection, Ground Water, 37(3), 376-381.

Katwagwa, K., (1934): Sur le Displacement et l'Ecart moyen de l'Ecoulement des Eaux Souterrains, Memoirs of the College of Science, Series A, kyoto university, pp. 431-441.

Kinzelbach, W. (1986): Developments in Water Science", Elsevier, Amsterdam.

Kitanidis, K. P., (1992): Analysis of macrodispersion through volume averaging: Moment equations, Stoc. Hydrol. Hydraul. 6, 5-25.

Kitanidis, P.K.,(1994a): The concept of the dilution index. Water Resources Research, 30(7), 2011-2026.

Kitanidis, K. P., (1994b): .Particle-tracking equations for the solution of the advection-dispersion equation with variable coefficients, Water Resources Research, 30(11), 3225-3227.

Kitanidis, P.K. (1995): Quasi-linear geostatistical theory for inversing, Water Resour. Res., 31(10), 2411-2419.

Klenk, I., and P. Grathwohl (2002): Transverse vertical dispersion in groundwater and the capillary fringe. Journal of Contaminant Hydrology, 58, 111-128.

Kobus, H. E. and K. Spitz (1985): Transverse Mixing of Stratified Flows in Porous Media, Presented at the 21st Congress of International Association for Hydraulic Research, Melbourne, Australia, August 19-23, , pp. 169-174.

Koltermann, C. E. & S. M. Gorelick, (1996): Heterogeneity in sedimentary deposits: A review of structure-imitating, process-imitating, and descriptive approaches, Water Resources. Res.32(9): 2617–2658.

Lawson, D. W. and D. E Elrick, (1972): A New method for Determining and Interpreting Dispersion Coefficients in Porous Media, Fundamentals of Transport Phenomena in Porous Media, Proceedings of the 2nd symposium of International Association of Hydrological Research-International Society of Soil Science, vol. 2, University of Guelph, Ontario, Canada, August 7-11, pp.753-777

Li, S.-G. & D. McLaughlin (1991): A non-stationary spectral method for solving stochastic groundwater problems: Unconditional analysis, Water Resources Res. 27(7): 1589–1605.

Li, S.-G. & D. McLaughlin (1995): Using the non-stationary spectral method to analyze flow through heterogeneous trending media, Water Resources Res. 31(3): 541–551.

Marsily, G. de., (1986): Quantitative Hydrogeology-Groundwater Hydrogeology for Engineers, Academic Press, Inc. 286-329pp.

Matheron, G., (1971): The theory of recognized variables and it s application. Les Cahiers du Centre de Morphologie Mathematique de Fontainebleau.

McCarty, P. L., M. N. Goltz,., G.D. Hopkins, M.E. Dolan, J.P Allan, B.T. Kawakami, & T.J. Carrothers (1998): Full-scale evaluation of in situ cometabolic degradation of trichloroethylene in groundwater through toluene injection, Environ. Sci. Technol. 32(1): 88–100.

Miralles-Wilhelm, F. & L. W. Gelhar (2000): Stochastic analysis of oxygen-limited biodegradation in heterogeneous aquifers with transient microbial dynamics, J. Contam. Hydrol. 42(1): 69–97.

Miralles-Wilhelm, F., L. W. Gelhar, and V. Kapoor (1997): Stochastic analysis of oxygen-limited biodegradation in three-dimensionally heterogeneous aquifers, Water Resources. Res., 33(6), 1251-1263.

Mohanty, K. K. and S. J Salter (1983): Multiphase flow in Porous Media: III. Oil Mobilization, Transverse Dispersion, and Wettability, Paper SPE 12127 presented at the 58th Annual Technical Conference of the Society of Petroleum Engineers of AIME, San Francisco, CA, October 5-8.

Moltyaner, G. L., and R. W. D. Killey (1988): Twin Lake Tracer Tests : Longitudinal Dispersion, Water Resources. Res., 24(10), 1613-1627.

Molz, F. & M. Widdowson (1988): Internal inconsistencies in dispersion-dominated models that incorporate chemical and microbial kinetics, Water Resources. Res. 24(4): 615–619.

Nadim, A., (1988): Measurement of shear-induced diffusion in concentrated suspensions with a Couette device. Phys. Fluids, 31(10), 2781-2785.

Nelder, J.A., and R. Mead (1965): A simplex method for function minimization, Computer J., 7(4), 308-313.

Neuman, S. P., C. L. Winter, & C.M Newman (1987): Stochastic theory of field-scale Fickian dispersion in anisotropic porous media, Water Resources. Res. 23(3): 453–466.

Nishigaki, M., T. Sudinda, Y. Sasaki, M. Inoue, and T. Moriwaki (1996): Laboratory Determination of Transverse and Longitudinal Dispersion Coefficients in Porous Media, Journal of Groundwater Hydrology, 38(1), 13-27.

Nowak, W. (2004): Geostatistical methods for the identification flow and transport Parameters in subsurface flow. Doctoral thesis, University of Stuttgart, Germany.

Ogata, A., and R. B. Banks (1961): A solution of the differential equation of longitudinal dispersion in porous media, U.S. Geological Survey, Professional Paper, 411-A.

Oliviera, B. I., A. H. Demond, and A. Salehzadeh (1996): Packing of Sands for the Production of Homogeneous Porous Media, Soil Science of America Journal, 60, 49-53.

Oya, S., and A. J. Valocchi (1998): Transport and biodegradation of solutes in stratified aquifers under enhanced in situ bioremediation conditions, Water Resour. Res., 34(12), 3323-3334.

Perkins, T.K. and O.C. Johnston (1963): A Review of Diffusion and Dispersion in Porous Media, Society of Petroleum Engineers Journal, March 1963, pp. 70-84

Pettijohn, F.J, P.E. Potter, R. Siever (1987): Sand and Sandstone, Springer-Verlag.

Pollock, D. W.,(1988): Semianalytical Computation of Path Lines for Finite-Difference models, Groundwater, 26(6), 743-750.

Prickett, T. A., T. G. Naymik, and C. G. Lonnquist (1981): A random-walk solute transport model for selected groundwater quality evaluations, Illinois State Water Survey, Bulletin 65.

Rajaram, H., and L. W. Gelhar (1991): 3-Dimensional spatial moments analysis of the Borden tracer test, Water Resources. Research., 27(6),1239-1251.

Ripple, C. D., R. V. James, and J. Rubin (1973): Radial particle-size segregation during packing of particulates into cylindrical containers, Powder Technology, 8, 165-175.

Ripple, C. D., R. V. James, and J. Rubin(1974): Packing-Induced Radial Particle-Size Segregation: Influence on Hydrodynamic Dispersion and Water Transfer Measurements, Soil Science of America Journal, 38, 219-222.

Robbins, G.A., (1989): Methods for determination of Transverse dispersion coefficient of porous media in column experiment. Water Resources Research, 25(6), 1249-1258.

Scheidegger, A. E.(1961): General theory of dispersion in liquid flow through porous media, Journal of Geophysical Resources, 66(10), 3273-3278.

Scheidegger, A. E., (1957): On the theory of flow of miscible phases in porous media, Proce. IUGG General Assembly, Toronto 2, 236-242.

Silliman, S.E., and L. Zheng (2001): Comparison of Observations from a Laboratory Model with Stochastic Theory: Initial Analysis of hydraulic and Tracer Experiments, Transp. Porous Media, 42(1-2), 85-107.

Simmons, C. S., T. R. Ginn, & B. D. Wood (1995): Stochastic-convective transport with nonlinear reaction: Biodegradation with microbial growth, Water Resources. Res., 31(11), 2675-2688, 1995.

Simpson, E. S. (1962): Transverse Dispersion in Liquid Flow Through Porous Media, Fluid Movement in Earth Materials, Geological Society of Professional Paper 411-C, united States Printing Office, Washington, 1962, pp. C1-C30.

Smart, P. L., and I. M. S. Laidlaw (1977): An Evaluation of Some Fluorescent Dyes for Water Tracing, Water Resources Research, 13(1), 15-33.

Sudicky, E. A., J. A. Cherry and E.O. Frind. (1983): Migration of contaminants in groundwater at a landfill: a case study. J. Hydrol. 63. 81-108.

Sudicky, E. A., R. W. Gillham, and E. O. Frind (1985): Experimental Investigation of solute Transport in Stratified Porous Media. I. The Nonreactive case, Water Resources Research, vol. 21, No. 7, July 1985, pp. 1035-1041

Taylor, G. I. (1954): The dispersion of matter in turbulent flow through a pipe, Proc. Roy Soc. A. 223, 446-468.

Taylor, G., (1953): Dispersion of Soluble matter in solvent Flowing through a Tube, Proceedings of Royal Society, vol. 219,186-203.

Thornton, S.F., S. Quigley, M.J. Spence, S. Banwart, S. Bottrell, D.N. Lerner (2001): Processes controlling the distribution and natural attenuation of dissolved phenolic compounds in a deep sandstone aquifer, J. Contam. Hydrol., 53(3-4), 233-267.

Tompson, A. F. B., E. G. Vomvoris, and L. W. Gelhar (1990): Numerical Simulation of Solute Transport in Three-Dimensional, Randomly heterogeneous Porous Media, Water Resources Res., 26(10), 2541-2562.

Ursino, N., T. Gimmi, and H. Flühler (2001): Dilution of non-reactive tracers in variably saturated sandy structures, Adv. Water Resour., 24(8), 877-885.

US EPA,(1999): Use of Monitored Natural Attenuation at Superfund, RCPA Corrective Action, and Underground Storage tank Sited. Report 9200.4-17P, U.S.EPA-Office of solid Waste and Emergency Response, Washington.

Wang, H. Q., N. Crampon, S. Huberson, and J. M. Garnier (1987): A Linear Graphical Method for Determining Hydrodispersive Characteristics in Tracer Experiments with Instantaneous Injection, Journal of Hydrology, 95, 143-154, 1987

Wang, J. & P. K. Kitanidis (1999): Analysis of macrodispersion through volume averaging: comparison with stochastic theory, Stoch. Environ. Res. Risk Ass. 13(1-2): 66–84.

Wang, L. B. (1996): Modelling complex reservoir geometries with multiple-point statistics, Math. Geol. 28(7): 895–907.

Weeks, S. W., and G. Sposito (1998): Mixing and stretching efficiency in steady and unsteady groundwater flows, Water Resources. Res., 34(12), 3315-3322.

Weidemeier, T.H., H.S. Rifai, C.J. Newell, and J.T. Wilson, (1999): Natural Attenuation if Fuels and chlorinated solvents in the subsurface. John Wiley and Sons, New York.

Xin, J. &D. Zhang (1998): Stochastic analysis of biodegradation fronts in one-dimensional heterogeneous porous media, Advances Water Resources. 22(2): 102–116.

Zhang, D., R. Andricevic, A. Y. Sun, X. Hu, & G. He (2000): Solute flux approach to transport through spatially nonstationary flow in porous media, Water Resources. Res. 36(8): 2107– 2120.

Zheng, C. and G. Bennett (1995): Applied Contaminant Transport modeling: Theory and Practice, Van Norstrand Reinhold, New York.

Zou, S., and A. Parr (1993): Estimation of Dispersion Parameters for Two-Dimensional Plumes, Ground Water, 31(3), 389-392.

Zou, S., and A. Parr (1994): Two-Dimensional Dispersivity Estimation Using Tracer Experiment Data, Ground Water, 32(3), 367-373.

10. Appendices

Appendix A

Detailed Drawings of the Sandbox

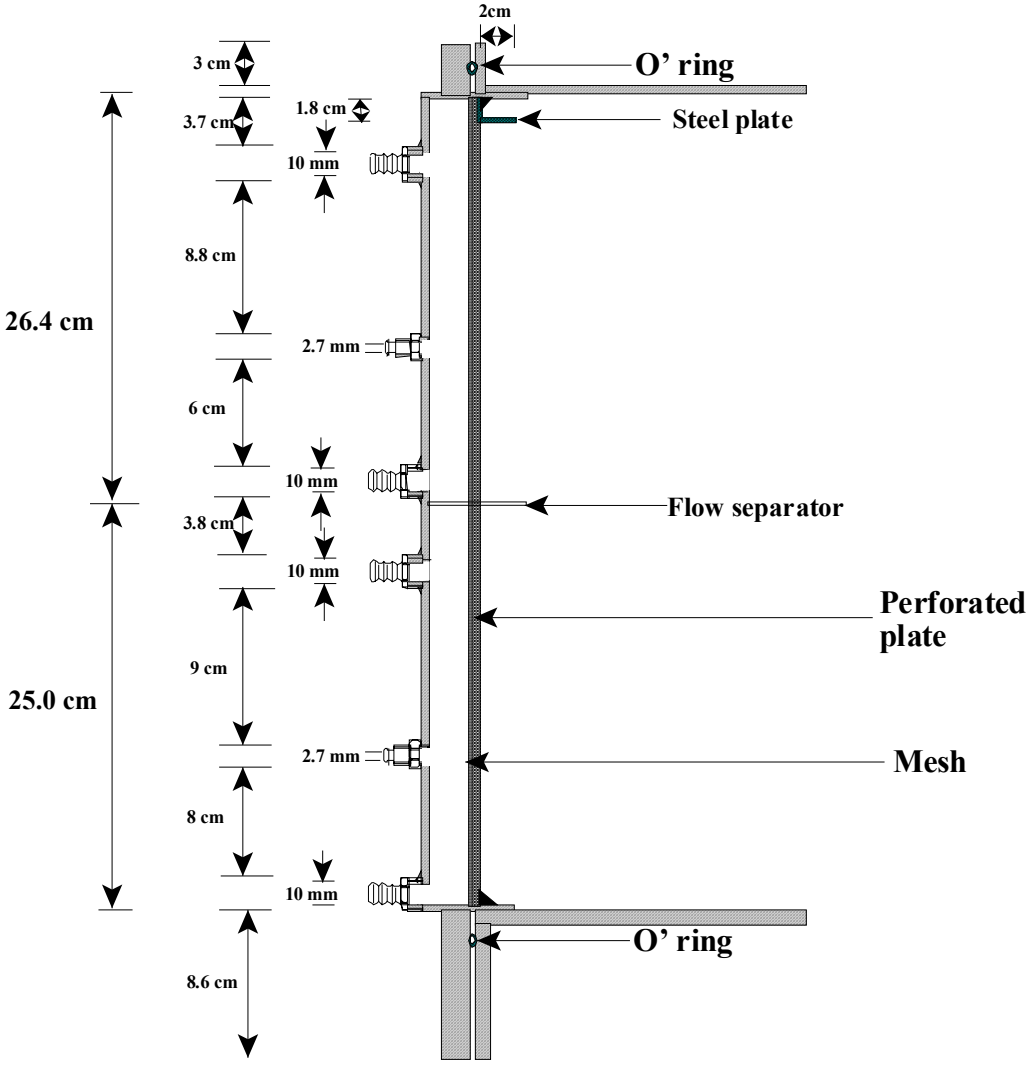

Appendix A.1 Side view of the Inlet

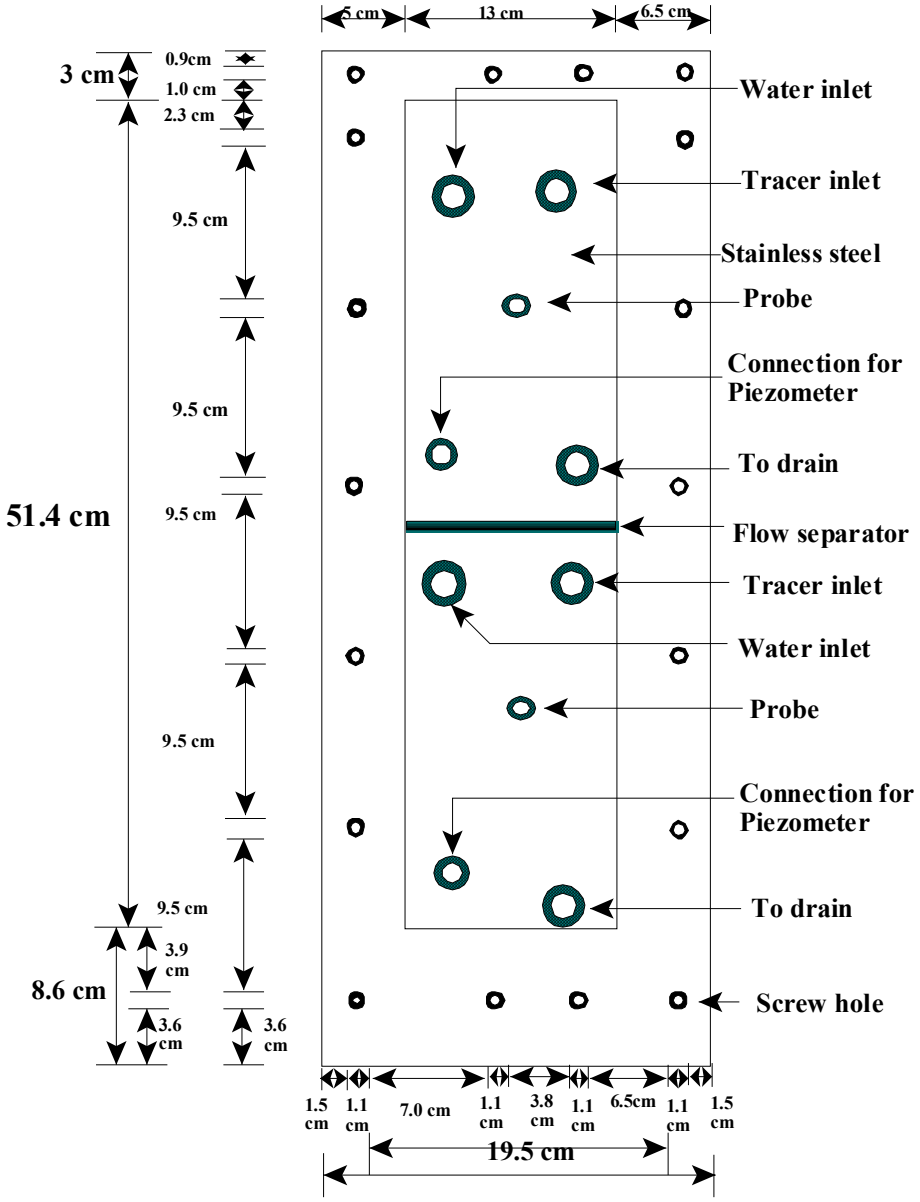

Appendix A.2 Front view of the Inlet

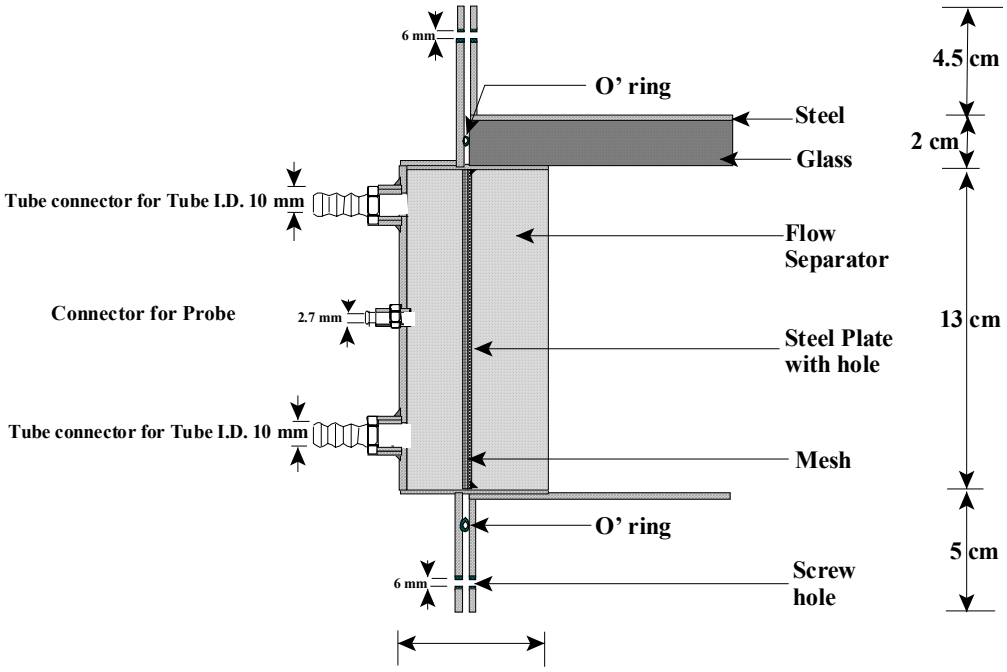

Appendix A.3 Top cross sectional view of the Inlet

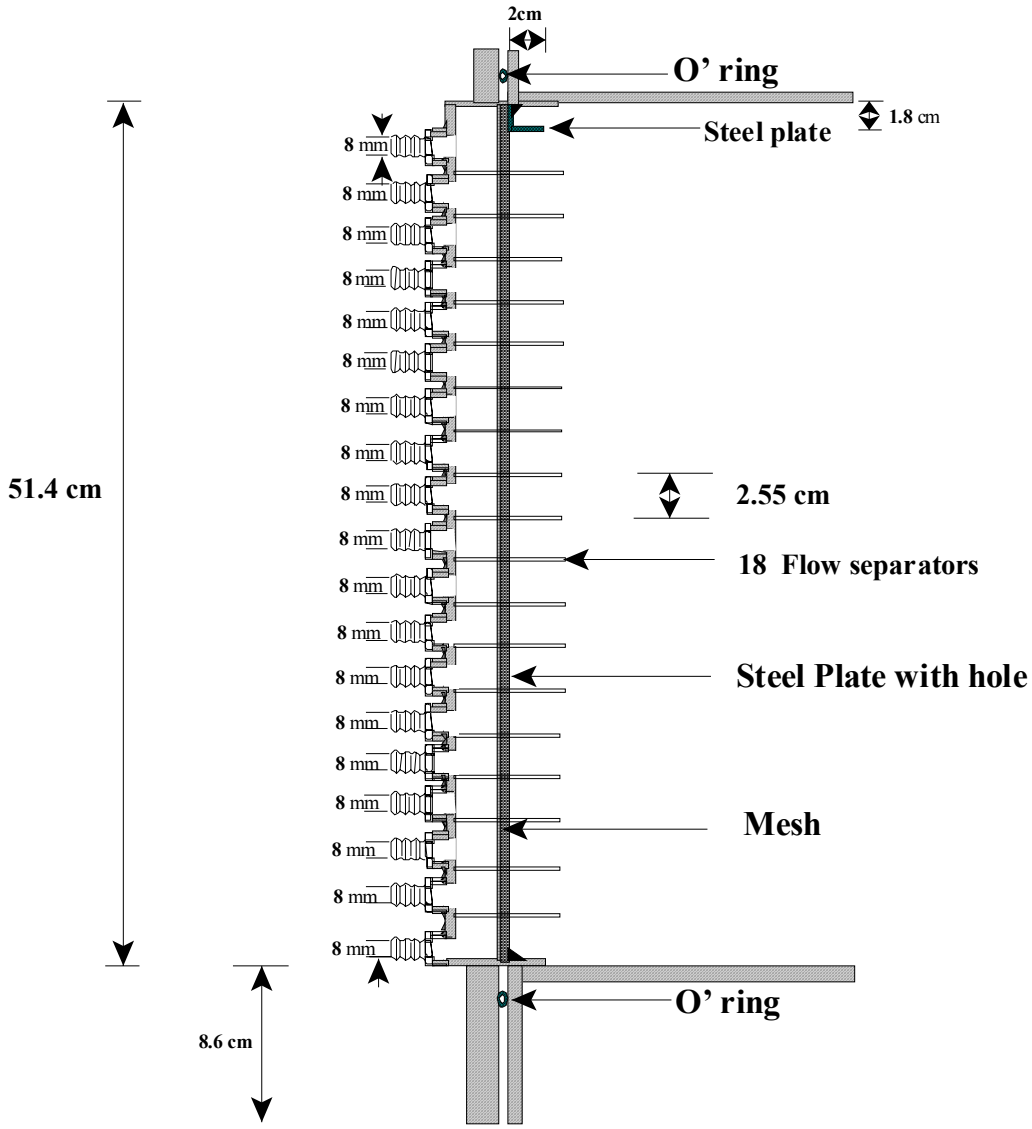

Appendix A.4 Side view of the Outlet

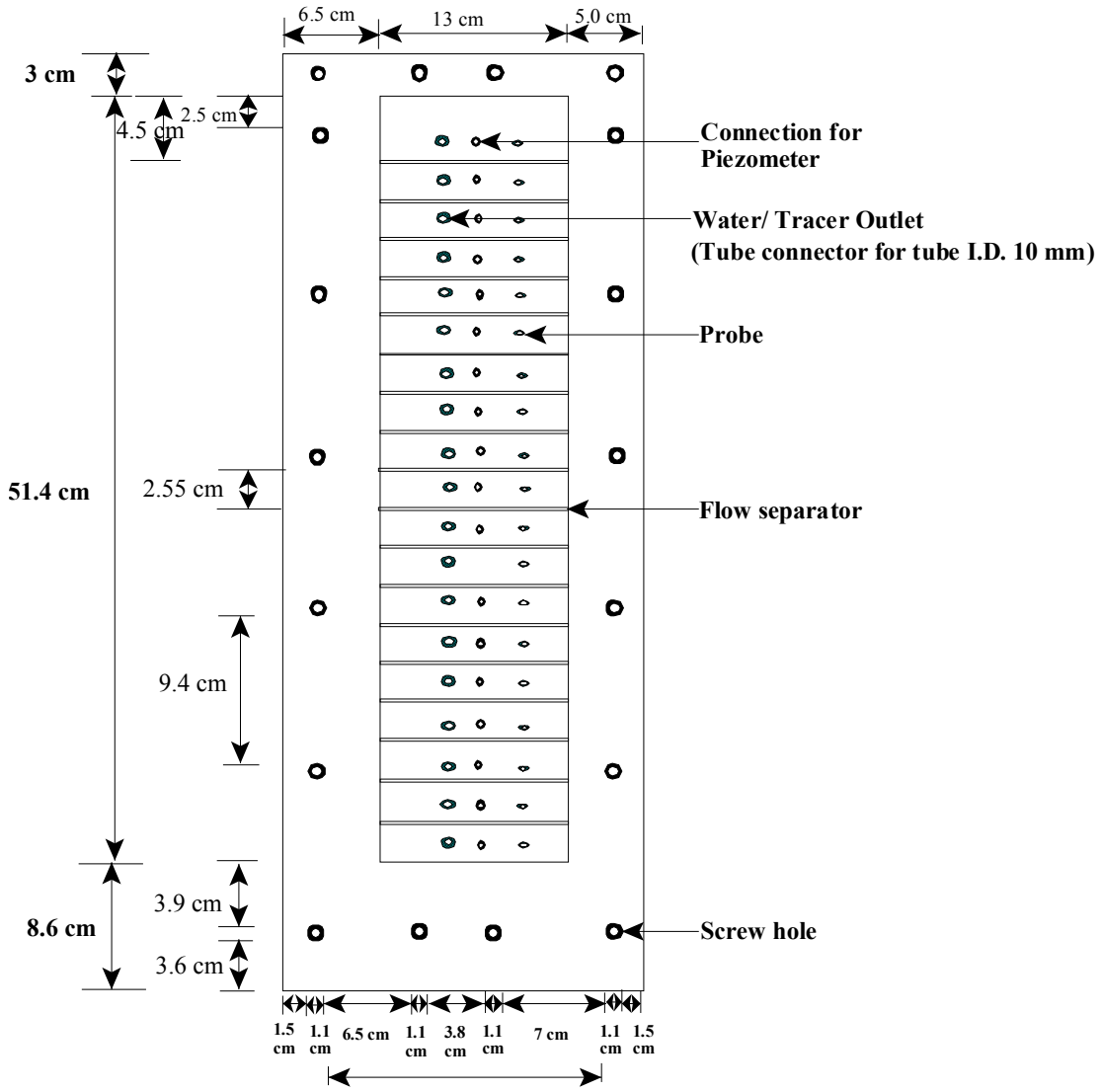

Appendix A.5 Front view of the Outlet

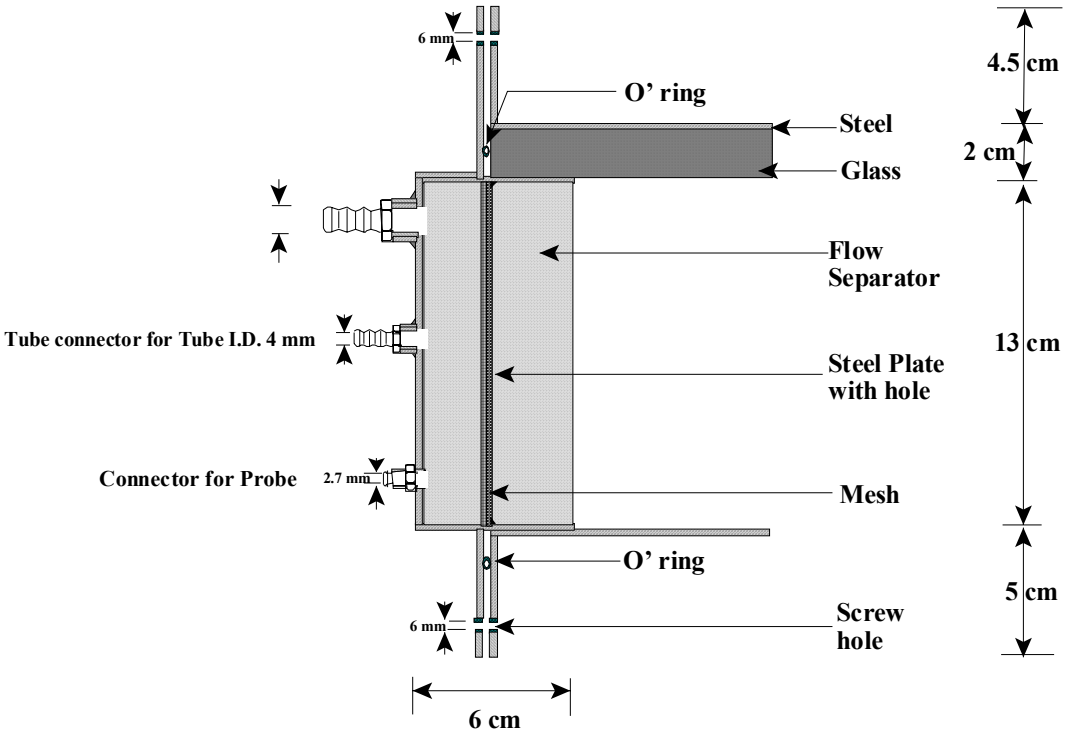

Appendix A.6 Top cross sectional view of the Outlet

Appendix B

Detailed Drawings of the Helical Soil Column

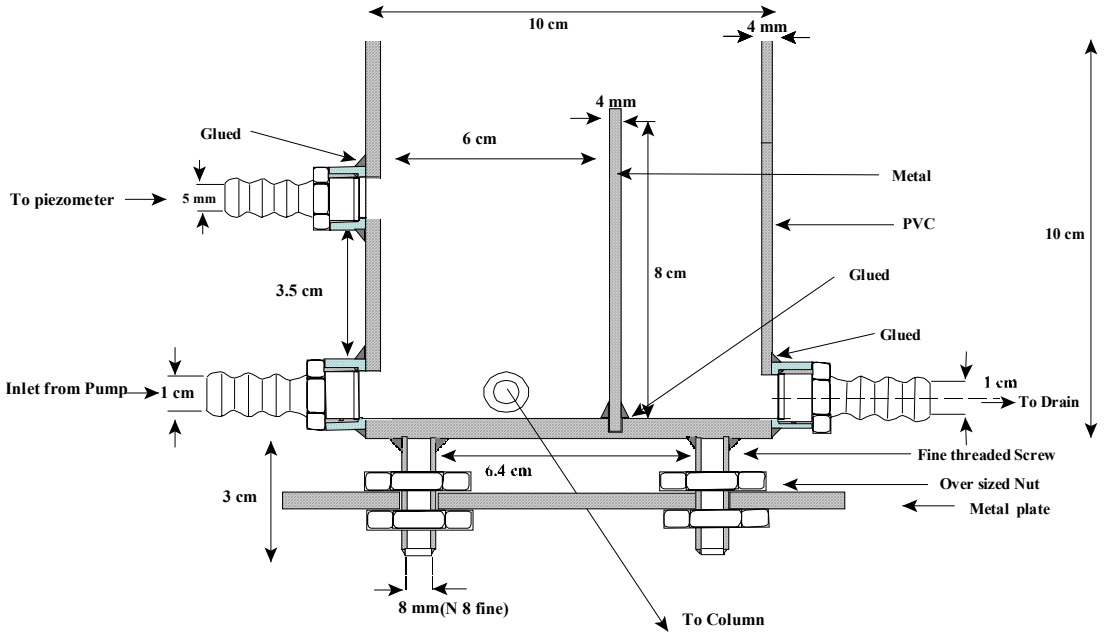

Appendix B. 1 Front cross sectional view of the Constant head Inlet

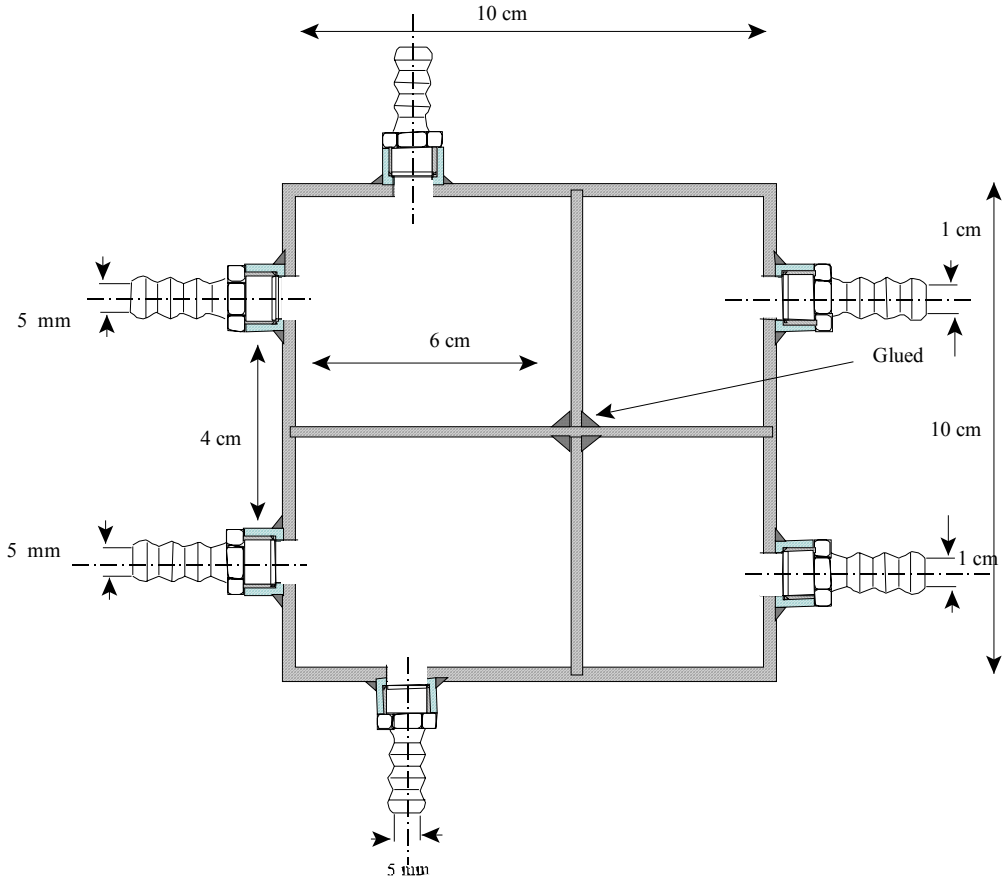

Appendix B. 2 Plan view of the Constant head Inlet

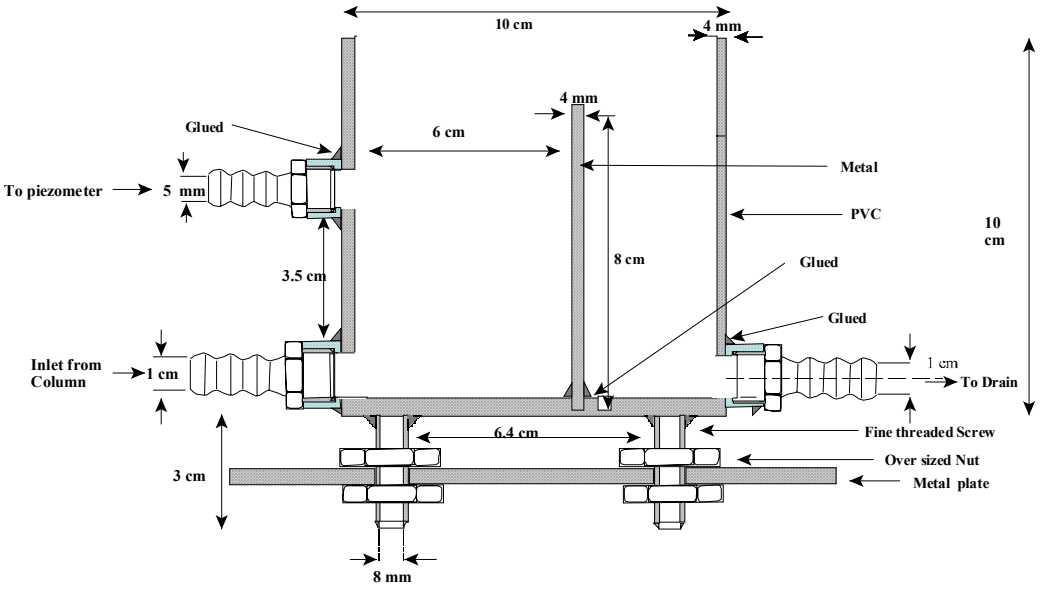

Appendix B. 3 Front cross sectional view of the Constant head Outlet

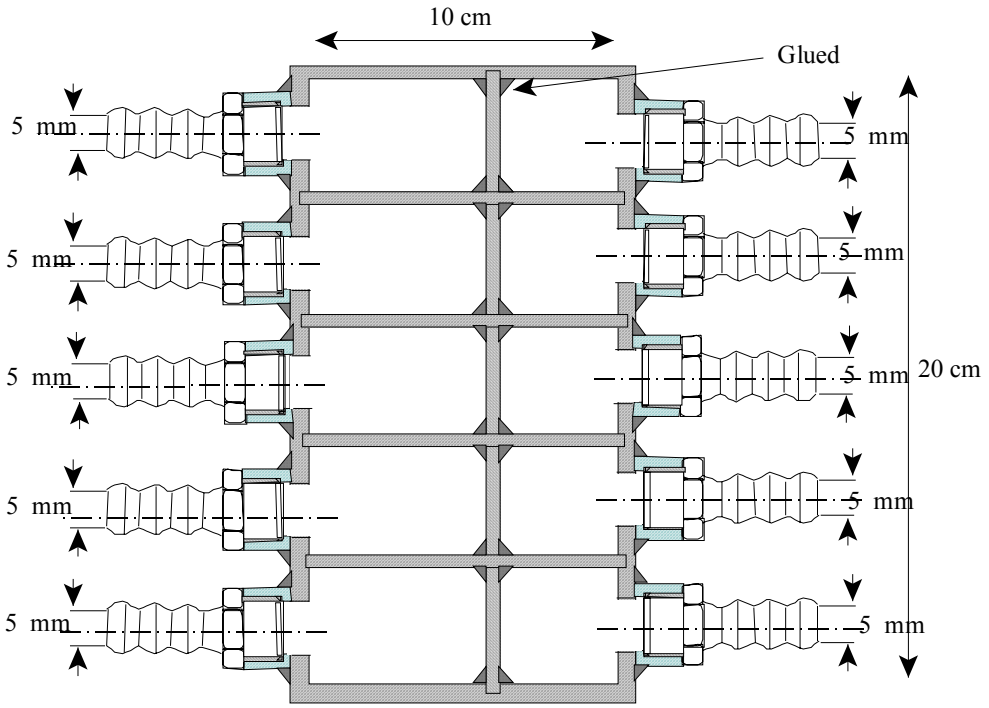

Appendix B. 4 Plan view of the Constant head outlet

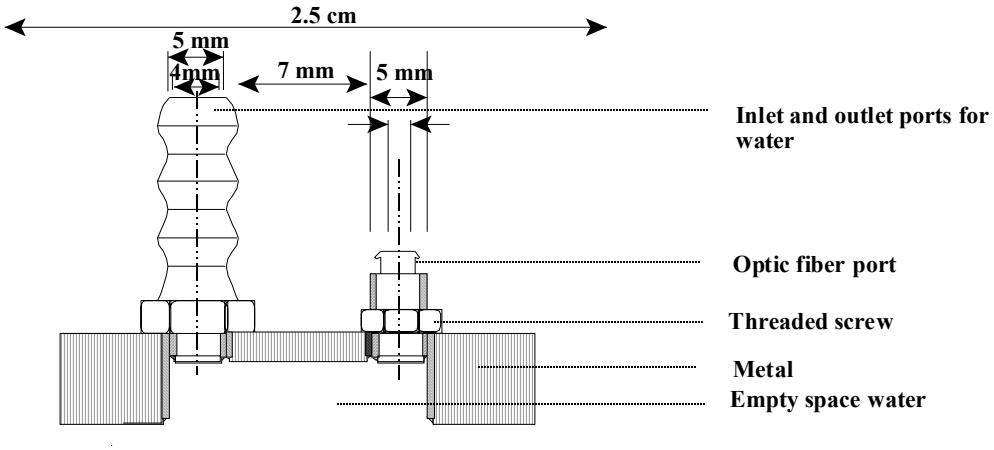

Appendix B. 5 Details of the inlet and outlet (1) of the helical column